FACULTY OF SCIENCE
UNIVERSITY OF COPENHAGEN

Electronic and Magnetic Properties of YbOCl, VS_2 and $CrCl_2(pyz)_2$

Master's Thesis in Physics

Written by *Freja Liebach Guttesen*

December 22, 2020

Supervised by

Per Hedegård

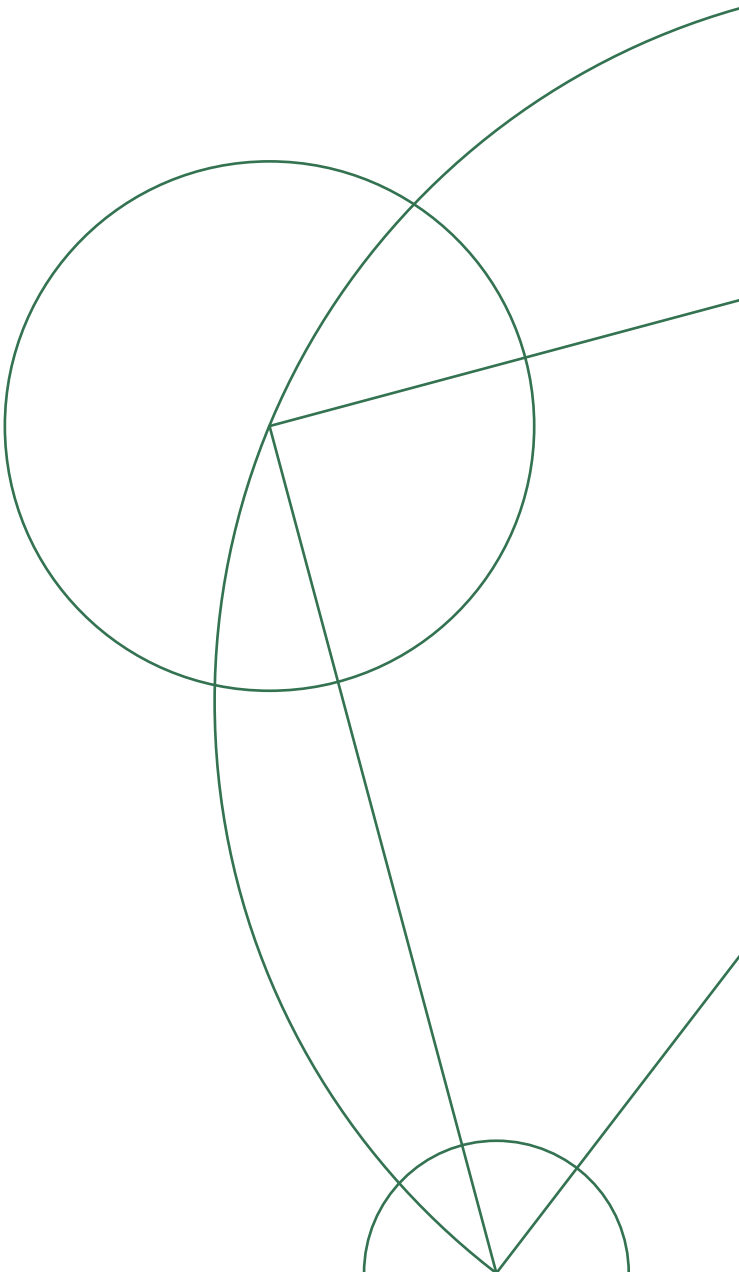

Abstract

Two-dimensional materials are of great interest in the field of solid state physics due to the wide range of applications of these, including the developement of efficent batteries, spintronics, electrocatalytic hydrogen evolution and solar cells. To be able to make use of these exciting new materials, the properties must be well-understood. The electronic and magnetic properties of three distinct two-dimensional materials have been investigated in this thesis. DFT calculations [1] suggests that the oxychloride compound YbOCl exhibit ferromagnetic properties. This is investigated analytically considering the classical Heisenberg model. The transition metal dichalcogenide monolayer VS_2 has been proposed to exhibit metallic behaviour with high conductivity by DFT [2], [3]. VS_2 can be found in two dinstinct geometrical configurations 1T-VS_2 and 2H-VS_2. The band structure of both structures is obtained, using the tight binding model combined with the Hubbard model, from which a metallic groundstate is obtained. Both phases are found to be ferromagnetic though a higher spin polarization is obtained for the 2H structure. From experiments, the organic inorganic hybrid 2D material $CrCl_2(pyz)_2$ has shown to exhibit ferrimagnetic ordering with a Curie temperature of $\simeq 55$ K and an insulating groundstate [4]. In this thesis the band structure of the compound is obtained using the tight binding model. This also suggests an insulating groundstate, though the density of states of the itinerant electrons on the pyrazine ligands is only one quarter filled. A simple model is suggested to describe the behaviour of the relevant spins in the system. This results in a ferrimagnetic ordering in agreement with the experimental data. The exchange interaction between neighbouring sites is investigated and an expression of the indirect exchange coupling between neighbouring chromium spins is obtained using the RKKY model.

Acknowledgements

I owe my greatest thanks to my supervisor Per Hedegård. He has been a great support and has devoted many hours to answer my questions and discuss the physics in the thesis. Thanks to Ivano Castelli for performing DFT calculations to the project, introducing me to this method and answering my numerous questions. Thanks to Yuyu Yao for showing me how she performs her experiments in the lab in Beijing and for elaborating her methods and results. Further, I want to thank both Louise, Cecilie and Poul for proofreading the thesis. I would like to thank my friends and family for the great support throughout this education.

Contents

Chapter 1

Introduction

1.1 Motivation

The first two-dimensional (2D) material ever realized was graphene in 2004 [5]. The importance of the result was emphasized in 2010, when the Nobel Prize in physics was given to Andre Geim and Konstantin Novoselov for this discovery. Graphene has shown to exhibit highly fascinating properties, including a resistance close to that of diamond, high thermal and electrical conductivity and the ability to generate electricity when exposed to sunlight [6]. Graphene has been studied broadly ever since the first realization. Other 2D graphene-like materials have subsequently been synthesized. Transition metal dichalcogenides (TMDs) can also be found in a two-dimensional form and is of great interest due to the wide range of properties, be they electronic [7], optical [8], mechanical [9] and thermal [10]. Another member of the family of 2D materials is MOX (M = Fe, Co, Mn, Cr, lanthanide, or actinide metals; O = oxygen, X = F, Cl, Br, I). These have theoretically been predicted to exhibit interesting electronic and magnetic properties [1]. An example of this is monolayer chromium oxyhalide (CrOX; X = Cl or Br), which is suggested to exhibit ferromagnetic semiconducting properties with Curie temperatures up to 160 and 129 K [11].

The versatile properties of 2D materials makes them usable in a wide range of applications. The present energy crisis demands fabrication of eficient batteries to restore energy. For this purpose 2D materials with large interlayer spacing and weak interlayer interactions together with high surface activity can be used [12]. Spintronics is one of the next-generation nanoelectronic devices in the goal of reducing power consumption and increasing memory and processing capabilities [13]. These devices, together with e.g. magneto-electrics and multi-ferroics, make use of the spin degree of freedom instead of or in addition to the charge degree of freedom of the transported electrons. This require materials with non-zero magnetic moments.

For these applications to be realized using 2D materials, the fundamental properties of these must be well investigated, both theoretically and experimentally. This motivates the study of the electronic and magnetic properties of three distinct 2D materials, namely YbOCl, VS_2 and $CrCl_2(pyz)_2$.

1.2 Thesis Outline

This thesis is structured in the following way. In **chapter 2** an introduction to group theory will be given, since this is exploited in the understanding of the energy sepctra obtained in the thesis. This is followed by a brief introduction to both the properties and fabrication of TMDs in **Chapter 3**. In **chapter 4** the compound YbOCl is studied. The classical Heisenberg model is used to investigate the magnetic properties of this. **Chapter 5** deals with monolayer VS_2. Using the tight binding model together with the Hubbard model, the electronic and magnetic properties are considered. Following a similar approach the compound $CrCl_2(pyz)_2$ is studied in **chapter 6**. Further, a simple model is suggested to understand the behaviour of the relevant spins of the system. The magnetic properties are further investigated using the RKKY model. Lastly, **chapter 7** contains a summary of the study's conclusions and suggestions for further research.

Chapter 2

Group Theory[1]

In quantum mechanics a great effort is spend on solving the Schrödinger equation to obtain eigenenergies and -functions in the study of atoms, molecules and solids. In the Hamiltonian, various effects can be included such as the Coulomb repulsion between the electrons, spin-spin coupling and external-field couplings, for instance the Zeeman effect. The eigenfunctions are functions of both the location and spin of all electrons in the system. Thus, even for a small number of interacting electrons, the dimension of the Hilbert space becomes too great for us to solve the Schrödinger equation. This is where group theory comes into play, since this is a measure to simplify the system. In the sort of problems explained above, symmetries of the Hamiltonian will be searched for, to simplify the calculations. Further, symmetries of a molecule or a Hamiltonian can be used to understand degeneracies and interactions in a system.

2.0.1 Abstract Group Theory

A group is given by a set of elements $\mathcal{G} = \{A, B, C, ...\}$, for which a group multiplication is defined as a binary operation that combines two elements to give a third element of the group. This operation must satisfy the following four conditions:

1. The set of elements must be closed under group multiplication.
2. The associate law must hold, i.e., $A(BC) = (AB)C$.
3. Any group must contain a unit element E for which $EA = AE = A$ for any element $A \in \mathcal{G}$.
4. To each element $A \in \mathcal{G}$ there exists an inverse A^{-1} in the group for which $AA^{-1} = A^{-1}A = E$.

If the group multiplication is commutative, i.e., if $AB = BA$, then the group is said to be *Abelian*.

In the following we will focus on finite groups. The *order* of a group is given by the number of elements in the group. A finite group thus has a finite order. An example of a finite group of general order is the set of the so-called covering operations of a symmetrical object. A covering operation is a reflection, rotation or inversion of a given object that brings the object to a form which is indistinguishable from the original object, i.e., the object is kept invariant under the transformation.

[1] This section is build on chapters 1-3 of [14].

The elements of the groups are given by the symmetry of the object. In this case the group multiplication AB means that operation B must be performed before operation A. These operations can be written in matrix form in a chosen basis, and the group multiplication is then matrix multiplication. The unit operation, E, corresponds to doing nothing. In matrix form this is the identity matrix. The inverse of an operation is given by physical considerations. The inverse of a rotation is a rotation with the same angle around the same axis but in the opposite direction. A mirror is its own inverse. An example of a set of covering operations is the *Vierergruppe*, which is the rotational symmetry group of a rectangular crystal.

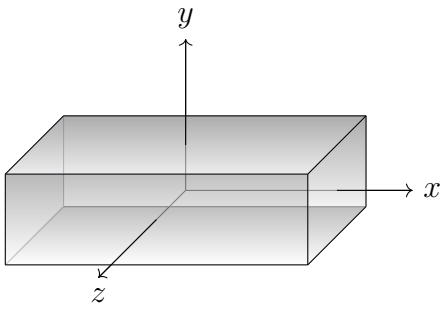

Fig. 2.1: The Vierergruppe consists of the symmetry elements covering a rectangular crystal. In addition to identity this group consists of three elements, i.e., rotations of π about the three axes; x, y and z.

	E	A	B	C
E	E	A	B	C
A	A	E	C	B
B	B	C	E	A
C	C	B	A	E

Table 2.1: Group-multiplication table of the Vierergruppe with elements $\{E, A, B, C\}$.

A group-multiplication table characterizes the group. The Vierergruppe consists of the elements $\{E, A, B, C\}$, where A, B and C are rotations by π around three orthogonal symmetry axes, see **Fig. 2.1**. It is therefore of order four. The multiplication table of this group is illustrated in **Table 2.1**. Each entry in the table is the product of the group element stated in the given row and column. All multiplication tables must obey the *rearrangement theorem*, which states that each row and column only contains each element once. This is a result of the fact that the group is closed and contains the inverse of each element of the group. The length of a column or row is equal to the number of elements, i.e., the order of the group. Thus, the group-multiplication table shows the rules of group theory.

The *period* of an element A is defined as

$$A, A^2, ..., A^{n-1}, A^n = E, \tag{2.1}$$

where n is the order of A. This sequence forms a group and if it does not contain all elements of the group, it forms a cyclic subgroup. Clearly, the elements of the subgroup must commute, and thus all cyclic groups are abelian. For an abelian group the group-multiplication table is symmetric around the diagonal. From **Table 2.1** it is clearly seen that the Vierergruppe is in fact an abelian group.

Groups can be split up into *classes*. Two symmetry operations, A, $B \in \mathcal{G}$, are said to be *conjugate* to each other if there exists another symmetry element, $X \in \mathcal{G}$, that relates A and B by a similarity transformation, i.e.,

$$B = X^{-1}AX. \tag{2.2}$$

If A and B are both conjugate to another element C of the same group, they must be each other's conjugate as well:

$$\begin{aligned} &C = X^{-1}AX = Y^{-1}BY \\ &A = XCX^{-1} = XY^{-1}BYX^{-1} = (YX^{-1})^{-1}BYX^{-1} \\ &A = Z^{-1}BZ, \quad \text{where} \quad Z = YX^{-1}. \end{aligned} \tag{2.3}$$

Here we have exploited the fact that groups are closed under group multiplication such that $Z \in \mathcal{G}$. Further, we have used that $XY^{-1} = (YX^{-1})^{-1}$. This means that a group can be divided into classes, which are sets of mutually conjugate elements. The identity element is always in a class for itself, since $X^{-1}EX = E$ for all elements $X \in \mathcal{G}$. All elements in an abelian group commute, such that

$$B = X^{-1}AX = X^{-1}XA = A. \tag{2.4}$$

This cannot be true, since all elements in the group must be unique. Therefore, all elements in abelian groups must be in their own class.

2.0.2 Representations

A *representation* of a group is a set of square matrices, where each matrix represents one element of the group. For an abstract group $\mathcal{G} = \{E, A, B, C, ...\}$, the representation of the element A is denoted $\Gamma(A)$. The matrix representations must fulfill the same multiplication table as the elements, thus

$$\Gamma(A)\Gamma(B) = \Gamma(AB). \tag{2.5}$$

If all the matrix representations are distinguishable, the order of this group is the same as the order of the group they are representing. In this case the representation is said to be *faithful*. The matrix representations of symmetry operations can often be reduced to block matrices. The goal is to seek an irreducible representation, since there is an infinite number of reducible representations but only a finite number of irreducible representations. The number of irreducible representations is equal to the number of classes of the symmetry point group. An irreducible representation is a representation that cannot be expressed in terms of other representations of lower dimensionality, where the dimensionality is given by the number of rows or columns of the representation. Reducible representations can be written in block form in terms of the irreducible representations. The advantage of block diagonal matrices is that the blocks are also representations of the operation, since they obey the same multiplication laws.

The great orthogonality theorem is essential to find the irreducible representations. This theorem states that for all nonequivalent, irreducible and unitary representations, it must be true that

$$\sum_R \Gamma^{(i)}(R)^*_{\mu\nu}\Gamma^{(j)}(R)_{\alpha\beta} = \frac{h}{l_i}\delta_{ij}\delta_{\mu\alpha}\delta_{\nu\beta}, \tag{2.6}$$

where R runs over all the elements of the group, l_i is the dimensionality of the ith representation $\Gamma^{(i)}$, δ_{ij} is the Kronecker delta and h is the order of the group. Another useful tool is *the dimensionality theorem* given by

$$\sum_i l_i^2 = h, \tag{2.7}$$

where i runs over all distinct irreducible representations[2]. The *character* of a symmetry operation is given by the trace of the irreducible matrix representation, $\mathrm{tr}[\Gamma(A)]$, i.e., the sum of the elements in the diagonal. Operations of the same class have the same character. Thus, the classes of symmetry operations can be distinguished by their character. If the group is not abelian and $AB = C$ and $BA = D$, then C and D still have the same character, $\chi_C = \chi_D$. This has to do with the general property of the trace, that it is unchanged under cyclic permutation of the matrices of which the trace is taken, i.e.,

$$\mathrm{tr}[ABC] = \mathrm{tr}[CAB] = \mathrm{tr}[BCA]. \tag{2.8}$$

Further, if $C = A \otimes B$ then $\chi_C = \chi_A\chi_B$.

The characters of all irreducible representations of a given group can be viewed in a so-called *character table*. The characters of each irreducible representation need also to fulfill the multiplication table of the group.

Properties of character tables

1. The sum of the squares of the dimensionality of all irreducible representations are equal to the order of the group. This is the dimensionality theorem, see Eq. (2.7).
2. The sum of the squares of the characters of any irreducible representation is equal to the order of the group.
3. The sum of the products of the corresponding characters of any two distinct irreducible representations must be zero. This originates from the orthogonality theorem, see Eq. (2.6).
4. All operations of the same class have the same character. This is referred to as *similarity*.
5. The number of irreducible representations is equal to the number of classes of the group. This is referred to as *completeness*.
6. All groups have a completely symmetric irreducible representation.

[2]Both theorems are proven in [14] pp. 20-25.

Representations of the Vierergruppe

A reducible representation of the Vierergruppe can be obtained from the elements of the $\mathbf{C_{2v}}$ group, since the Vierergruppe and the $\mathbf{C_{2v}}$ group are isomorphic. $\mathbf{C_{2v}}$ consists of the elements; C_2: a rotation of an angle of π around the z-axis, σ_v: a reflection in the xy-plane, and σ_v': a reflection in the yz-plane, besides the unit transformation. This can be written as three-dimensional matrices, using the cartesian coordinates depicted in **Fig. 2.1**,

$$\begin{aligned} E = \begin{bmatrix} 1 & 0 & 0 \\ 0 & 1 & 0 \\ 0 & 0 & 1 \end{bmatrix}, \quad A = \sigma_v = \begin{bmatrix} 1 & 0 & 0 \\ 0 & -1 & 0 \\ 0 & 0 & 1 \end{bmatrix}, \\ B = \sigma_v' = \begin{bmatrix} -1 & 0 & 0 \\ 0 & 1 & 0 \\ 0 & 0 & 1 \end{bmatrix}, \quad C = C_2 = \begin{bmatrix} -1 & 0 & 0 \\ 0 & -1 & 0 \\ 0 & 0 & 1 \end{bmatrix}. \end{aligned} \tag{2.9}$$

Since it is an abelian group, it has four classes, i.e., $\{E\}$, $\{A\}$, $\{B\}$ and $\{C\}$. We will now seek the irreducible representations of this group. From the dimensionality theorem, see Eq. (2.7), we know that

$$l_1^2 + l_2^2 + l_3^2 + l_4^2 = 4. \tag{2.10}$$

The only solution to this is $l_1 = l_2 = l_3 = l_4 = 1$. Thus, there must be four one-dimensional irreducible representations. This agrees with the fact that the number of classes must be equal to the number of irreducible representations. From the second property of character tables, we know that the sum of the squares of the characters in all four irreducible representations must sum to four. Therefore, all characters must be ± 1. From the sixth property we must write one of the representations with all characters equal to one. From the orthogonality theorem the rest is found. This is illustrated in **Table 2.2**.

	E	C_2	σ_v	σ_v'
Γ_1	1	-1	1	-1
Γ_2	1	-1	-1	1
Γ_3	1	1	1	1
Γ_4	1	1	-1	-1

Table 2.2: Character table of the Vierergruppe.

Reducible representations of the four elements can now be written in terms of these irreducible representations as

$$E = \begin{bmatrix} 1 & 0 & 0 & 0 \\ 0 & 1 & 0 & 0 \\ 0 & 0 & 1 & 0 \\ 0 & 0 & 0 & 1 \end{bmatrix}, \quad A = \sigma_v = \begin{bmatrix} 1 & 0 & 0 & 0 \\ 0 & -1 & 0 & 0 \\ 0 & 0 & 1 & 0 \\ 0 & 0 & 0 & -1 \end{bmatrix},$$
$$B = \sigma_v' = \begin{bmatrix} -1 & 0 & 0 & 0 \\ 0 & 1 & 0 & 0 \\ 0 & 0 & 1 & 0 \\ 0 & 0 & 0 & -1 \end{bmatrix}, \quad C = C_2 = \begin{bmatrix} -1 & 0 & 0 & 0 \\ 0 & -1 & 0 & 0 \\ 0 & 0 & 1 & 0 \\ 0 & 0 & 0 & 1 \end{bmatrix}. \tag{2.11}$$

These representations consists of the previous representations with an addiational component such that the dimensionality of the representations is the same as the order of the group. Since these are not irreducible representations, the trace of the diagonals do not agree with the characters of the character table, see **Table 2.2**.

2.0.3 Group Theory and Quantum Mechanics

In quantum mechanics, the relevant operators are symmetry operators that leave the Hamiltonian of the given system invariant. These operators can be specified by a real orthogonal transformation, $\mathbf{R}$, which relates the new coordinates $\mathbf{x}'$ with the old coordinates $\mathbf{x}$ by

$$\mathbf{x}' = \mathbf{R}\mathbf{x}. \tag{2.12}$$

This transformation $\mathbf{R}$ can represent a rotation of the coordinates, a reflection, an inversion or a combination of these. A new group, isomorphic to this group, can be introduced in which the elements of the group are transformation operators that acts on functions instead of coordinates. The operator that corresponds to $\mathbf{R}$ is denoted $\hat{P}_R$ and is defined through the following relation

$$\hat{P}_R f(\mathbf{R}\mathbf{x}) = f(\mathbf{x}), \tag{2.13}$$
$$\hat{P}_R f(\mathbf{x}) = f(\mathbf{R}^{-1}\mathbf{x}). \tag{2.14}$$

This means that $\hat{P}_R$ transforms the functional form of $f(x)$ such that it compensates for the way $\mathbf{R}$ transforms the coordinates. To investigate if the group of operators $\hat{P}_R$ is in fact isomorphic to the group of coordinate transformations $\mathbf{R}$, we must verify that

$$\hat{P}_S \hat{P}_R = \hat{P}_{SR}. \tag{2.15}$$

To do this we define the new function $g(\mathbf{x})$ as

$$\hat{P}_R f(\mathbf{x}) = f(\mathbf{R}^{-1}\mathbf{x}) = g(\mathbf{x}), \tag{2.16}$$

and using Eq. (2.14), we find that

$$\begin{aligned}\hat{P}_S[\hat{P}_R f(\mathbf{x})] &= \hat{P}_S g(\mathbf{x}) = g(\mathbf{S}^{-1}\mathbf{x}),\\ &= f[\mathbf{R}^{-1}(\mathbf{S}^{-1}\mathbf{x})] = f[(\mathbf{RS})^{-1}\mathbf{x}] = \hat{P}_{SR} f(\mathbf{x}).\end{aligned} \tag{2.17}$$

This proves the relation in Eq. (2.15), which says that the operation $\hat{P}_{SR}$ is the product of the operation $\hat{P}_S$ and $\hat{P}_R$ in the proper order. Now we will focus on a certain group of operators $\hat{P}_R$ that commute with the Hamiltonian $\hat{\mathcal{H}}$, i.e., $[\hat{P}_R, \hat{\mathcal{H}}] = 0$. The elements in this group will consists of all transformations that leave $\hat{\mathcal{H}}$ invariant. Such a set of operators are said to form *the group of the Schrödinger equation*. Applying one of these operators to the Hamiltonian results in

$$\hat{P}_R \hat{\mathcal{H}} \psi_n = \hat{P}_R E_n \psi_n, \tag{2.18}$$

$$\hat{\mathcal{H}} \hat{P}_R \psi_n = E_n \hat{P}_R \psi_n, \tag{2.19}$$

where ψ_n and E_n are the eigenvectors and eigenenergies of the Hamiltonian, respectively. Thus, knowing one eigenfunction of the Hamiltonian, the degenerate eigenfuntions can be found by applying symmetry operators that commutes with the Hamiltonian. If this procedure results in all the degenerate eigenfunctions, the degeneracy is said to be *normal*.

Basis Functions

Basis functions form a linearly independent set that span the space, such that every function in the space can be uniquely represented by a linear combination of these. Let $\phi_\kappa^{(j)}$ denote the basis function for the κth row of the jth irreducible representation. The so-called *partners* of this basis function are the other basis functions $\phi_\lambda^{(j)}$ required to complete the basis for the representation. The result of operating any element of the group on $\phi_\kappa^{(j)}$ can be written in terms of the basis functions as

$$\hat{P}_R \phi_\kappa^{(j)} = \sum_{\lambda=1}^{l_j} \phi_\lambda^{(j)} \Gamma^{(j)}(R)_{\lambda\kappa}. \tag{2.20}$$

Multiplying through $\Gamma^{(i)}(R)^*_{\lambda'\kappa'}$, summing over R on both sides, and applying the great orthogonality theorem, see Eq. (2.6), we obtain

$$\sum_R \Gamma^{(i)}(R)^*_{\lambda'\kappa'} \hat{P}_R \phi_\kappa^{(j)} = \frac{h}{l_j} \delta_{ij} \delta_{\kappa\kappa'} \phi_{\lambda'}^{(j)}. \tag{2.21}$$

The *projection* operator can now be defined as

$$\hat{\mathscr{P}}^{(j)}_{\lambda\kappa} = \frac{l_j}{h} \sum_R \Gamma^{(j)}(R)^*_{\lambda\kappa} \hat{P}_R. \tag{2.22}$$

It is evident from Eq. (2.21) that applying this operator on a basis function yields zero unless this basis function belongs to the κth row of $\Gamma^{(j)}$.

If this condition is satisfied, the operation results in the basis function $\phi_\lambda^{(j)}$. Knowing just one basis function, this provides a method for obtaining the partners of that basis. If $\lambda = \kappa$, then

$$\hat{\mathscr{P}}_{\kappa\kappa}^{(j)} \phi_\kappa^{(j)} = \phi_\kappa^{(j)}. \tag{2.23}$$

This shows that $\phi_\kappa^{(j)}$ is an eigenfunction of $\hat{\mathscr{P}}_{\kappa\kappa}^{(j)}$ with eigenvalue $\mathbb{1}$. This allow for a unique identification of the labels of a given basis function. Due to the fact that the projection operator is linear, any linear combination of basis functions from the κth row of $\Gamma^{(j)}$, expressed in terms of other basis functions, will also be an eigenfunction of $\hat{\mathscr{P}}_{\kappa\kappa}^{(j)}$. If $\Gamma^{(1)}$, $\Gamma^{(2)}$,..., $\Gamma^{(n)}$ are all the distinct irreducible representations of a group of operators $\hat{P}_R$, then any function F, in the space operated by $\hat{P}_R$, can be decomposed into a sum of the form

$$F = \sum_{j=1}^{n} \sum_{\kappa=1}^{l_j} f_\kappa^{(j)}, \tag{2.24}$$

where $f_\kappa^{(j)}$ belongs to the κth row of the irreducible representation[3]. Since we know how the projection operator works on the right hand side, i.e.,

$$\hat{\mathscr{P}}_{\kappa\kappa}^{(j)} f_{\kappa'}^{(j')} = \delta_{jj'} \delta_{\kappa\kappa'} f_\kappa^{(j)}, \tag{2.25}$$

combined with Eq. (2.24), we conclude that

$$\hat{\mathscr{P}}_{\kappa\kappa}^{(j)} F = f_\kappa^{(j)}. \tag{2.26}$$

This equation explains the name of the projection operator, since it projects out the part of any function that belongs to the κth row of the jth representation. The projection operator can be used to obtain the basis functions. The procedure is as follows: start with any function F, project into the κth row of the jth representation using $\hat{\mathscr{P}}_{\kappa\kappa}^{(j)}$ and finally find all partners using $\hat{\mathscr{P}}_{\lambda\kappa}^{(j)}$. This procedure is called the *basis-function generating machine*. Lastly, we want to rewrite the expression for the projection operator in terms of the characters of the given representation. Setting $\lambda = \kappa$ in Eq. (2.22) and summing over κ leads to the expression

$$\hat{\mathscr{P}}(j) = \sum_{\kappa\kappa} \hat{\mathscr{P}}_{\kappa\kappa}^{(j)} = \frac{l_j}{h} \sum_R \chi^{(j)}(R)^* \hat{P}_R, \tag{2.27}$$

since $\sum_\kappa \Gamma^{(j)}(R)_{\kappa\kappa}^* = \chi^{(j)}(R)^*$. Thus, knowing the character table of a given symmetry group, any function can be projected into a representation using this expression. This will be put into use in both **chapter 5** and **chapter 6**.

[3]This is proven in [14] pp. 40-41.

Chapter 3

Introduction to TMDs

TMDs are materials of the type MX_2 where M is a transition metal, i.e., elements in group 3 to 12 of the periodic table, and X is a chalcogen atom, i.e., elements from group 16 of the periodic table. One layer of the M-atoms is sandwiched in between two layers of X-atoms. To form bulk materials these layers are coupled through the weak Van der Waals (VdW) force like in graphite. This enables the experimentalists to produce transition metal dichalcogenide monolayers, which is a special type of 2D materials [15].

3.1 Properties of TMD Monolayers

Already in 1977 the photoelectrochemical properties of bulk TMDs were studied [16]. Both MoS_2 and WS_2 can experience a phototransition without photodecomposition, and this is a great advantage for solar energy conversion to electrical energy. The following years many other TMDs were found to be good candidates for solar cells, but the interest in TMDs was mainly focused on the high stability they can exhibit. Today, TMD monolayers of different kinds are stacked together or combined in nanohybrids monolayer TMDs to enhance this stability [17]. Several TMDs e.g. MoS_2, $MoSe_2$, WS_2, WSe_2 changes from having an indirect band gap to having a direct electronic and optical band gap when reducing the thickness to monolayer [18]. The high stability combined with the existence of a band gap and a good electron mobility make TMD monolayers good candidates for transistors. The mobility of monolayer TMDs is usually lower than for bulk, though this problem can be solved by coatings [19]. The existence of a direct band gap further make TMD monolayers promising candidates to use in optoelectronics. The majority of TMD monolayers are semiconducting though TMD monolayers with metallic behaviour exists. This results in a higher conductivity, which is relevant in the developement of efficient batteries as devices for energy storage [2]. Further, these monolayers can exhibit both magnetic [20], [21] and superconducting [22], [23] behaviour. The former case is of great importance when producing devices that explore the spin degree of freedom.

3.2 Fabrication of TMD Monolayers

TMD monolayers can be fabricated in several ways, of which two will be described briefly here. The first method, named exfoliation, exploits the fact that the layers off bulk compounds are coupled through the very weak VdW force. Adhesive tape is placed on the bulk material. Removing this tape will pull of one (or more) layers of the TMD. Thereafter, the adhesive tape is placed on a substrate on which it will deposit small

flakes of monolayers or multilayers of the TMD material. This amazingly simple and cheap method has been used widely ever since graphene was obtained experimentally for the first time in 2004 using this method [5]. The disadvantage of this method is that it is difficult to control the thickness of the sample placed on the substrate, such that the reproducibilty of TMD monolayers is small. An alternative to this method is chemical vapor deposition (CVD) [24]. This is a more complicated and expensive method, though it is much easier to control. To form TMDs using the CVD method, precursors of the material, i.e., a transition metal oxide and pure chalcogen, are placed in a furnace together with the substrate. The furnace is heated to temperatures between 650 and 1000 $^{\circ}$C with an inert gas flowing through the furnace, picking up the precursors and depositing it on the substrate.

Chapter 4

YbOCl

4.1 Introduction to YbOCl

In 1993 four lanthanide[1] oxychlorides, including ytterbium oxychloride (YbOCl), was realized [25]. Magnetic susceptibility data was obtained, which showed YbOCl to be paramagnetic. Song and Kauzlarich suggested that this was due to the unpaired electrons on Yb^{3+} (f^{13}) ions. In 2018 a numerical study of 108,423 unique, experimentally known 3d compounds were investigated [1]. A subset of promising exfoliable layered compounds were identified. A small subset of 258 compounds were investigated more thoroughly and the electronic and magnetic properties of these were investigated using density-functional theory (DFT) calculations. In this study YbOCl was characterized as a metal with ferromagnetic properties. This motivated Yao et al. [26] to realize this material experimentally using the CVD method described above. The structure was characterized using Raman scattering and YbOCl has never been realized this thin before with a thickness of $\simeq 6$ nm.

Monolayer YbOCl is a 2D MOX material, and it consists of a layer of Cl-Yb-O-O-Yb-Cl as seen in **Fig. 4.1**. In bulk YbOCl these layers are stacked through the VdW force. The electron configuration for the relevant elements is Yb: [Xe]$6s^2 4f^{14}$, O: [He]$2s^2 2p^4$ and Cl: [Ne]$3s^2 3p^5$. Thus, the ytterbium atoms lose one electron to the chlorine atoms and two electrons to the oxygen atoms which results in Yb^{3+}-ions. In the following we will investigate one layer of YbOCl using the classical Heisenberg model. This is done both with and without an external magnetic field.

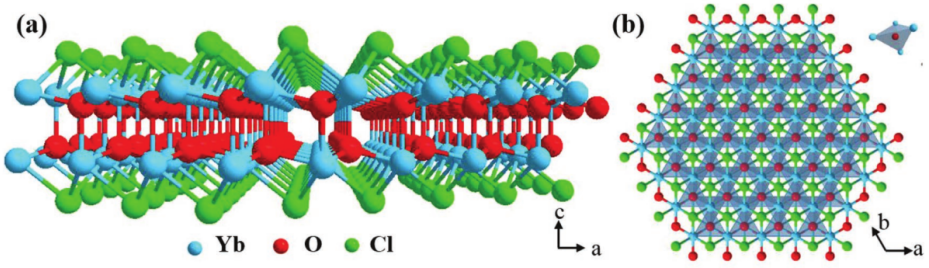

Fig. 4.1: Structure of YbOCl seen along the b crystalline axis **(a)** and the c crystalline axis **(b)**. In the upper right corner of **(b)**, a single Yb_4O tetrahedral unit is shown. Blue circle represents Yb, red circle: O and green circle: Cl. The figure is taken from the paper by Yao et al. [26].

[1]Lanthanides are elements with atomic numbers 57-71. The name stems from the fact that their chemical properties are similar to lanthanum.

4.2 Classical Heisenberg Model of Monolayer YbOCl

Monolayer YbOCl will now be studied theoretically using a classical approach. The structure illustrated along the c crystalline direction is seen in **Fig. 4.2**. Only the ytterbium atoms, located in two distinct sublayers denoted top (t) and bottom (b), are viewed.

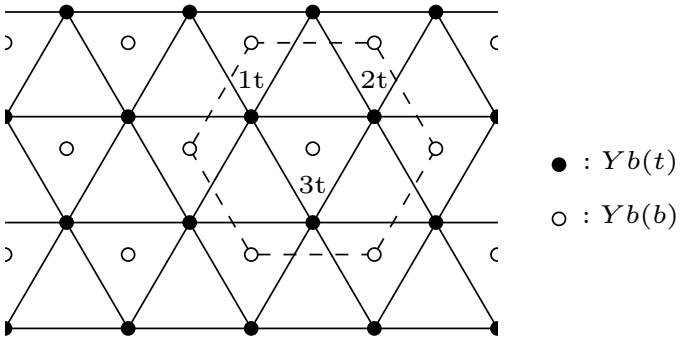

Fig. 4.2: Schematic top view of the Yb atoms of the top (black) and bottom (white) sublayers of YbOCl. One unit cell, indicated with the dashed hexagon, includes three Yb atoms of each sublayer. The three Yb atoms of the top sublayer has been enumerated $1t$, $2t$ and $3t$. The coupling lines between the Yb atoms in the top sublayer are illsutrated with solid lines.

Since the f-shell on each ytterbium atom is only missing a single electron to be filled, these sites can be viewed as if they are occupied by a single hole with spin $S = 1/2$. These couple through the oxygen atoms between them, but in this simplified model we assume that the spins couple directly. The Hamiltonian for the exchange interaction is

$$\mathcal{H}_t = J \sum_{\langle ij \rangle} \mathbf{S}_i \cdot \mathbf{S}_j, \tag{4.1}$$

which is refered to as the Heisenberg model. J denotes the exchange coupling constant and $\mathbf{S}_i$ denotes the spin of the electron at site i. The latter is a vector since the calculations are done in a classical picture. Only nearest neighbour contributions are included, which is indicated by the $\langle ij \rangle$ in the sum. The sign of J determines the configuration of the spins. When J is positive, Eq. (4.1) is minimized if $\mathbf{S}_i$ and $\mathbf{S}_j$ are antiparallel, which is an antiferromagnetic coupling. $J < 0$ yields a ferromagnetic coupling since Eq. (4.1) is minimized for parallel spins. Focusing on the top sublayer and knowing that the spins are configured in a triangular lattice, see **Fig. 4.1**, the Hamiltonian can be written as

$$\mathcal{H}_t = J_t \left[\mathbf{S}_{1t} \cdot (\mathbf{S}_{2t} + \mathbf{S}_{3t}) + \mathbf{S}_{2t} \cdot (\mathbf{S}_{1t} + \mathbf{S}_{3t}) + \mathbf{S}_{3t} \cdot (\mathbf{S}_{1t} + \mathbf{S}_{2t}) \right] N, \tag{4.2}$$

where $\mathbf{S}_{it}$, $i = 1, 2, 3$, are the three spins in one unit cell, see **Fig. 4.2**. N is the number of unit cells and J_t refers to the exchange integral for sublayer t. The latter is assumed to be constant.

This Hamiltonian can be expressed in terms of the length of the spin using

$$\mathbf{S}_t = \mathbf{S}_{1t} + \mathbf{S}_{2t} + \mathbf{S}_{3t}, \tag{4.3}$$

$$S_t^2 = S_{1t}^2 + S_{2t}^2 + S_{3t}^2 + 2\left(\mathbf{S}_{1t}\cdot\mathbf{S}_{2t} + \mathbf{S}_{2t}\cdot\mathbf{S}_{3t} + \mathbf{S}_{1t}\cdot\mathbf{S}_{3t}\right). \tag{4.4}$$

Exploiting the fact that one hole occupies each site such that $S_{1t}^2 = S_{1t}(S_{1t}+1) = 3/4 = S_{2t}^2 = S_{3t}^2$, the Hamiltonian for the top sublayer can be written as

$$\mathcal{H}_t = J_t\left(S_t^2 - \frac{9}{4}\right)N, \tag{4.5}$$

and similarly for sublayer b. The Hamiltonian describing the interactions between the spins of the two sublayers, still assuming only nearest neighbor coupling, is given by

$$\mathcal{H}_{tb} = J_{tb}\left(\mathbf{S}_{1b} + \mathbf{S}_{2b} + \mathbf{S}_{3b}\right)\cdot\left(\mathbf{S}_{1t} + \mathbf{S}_{2t} + \mathbf{S}_{3t}\right)N = J_{tb}\mathbf{S}_b\cdot\mathbf{S}_t N, \tag{4.6}$$

which results in the total Hamiltonian

$$\mathcal{H} = \mathcal{H}_t + \mathcal{H}_b + \mathcal{H}_{tb} = J_t\left(S_t^2 - \frac{9}{4}\right)N + J_b\left(S_b^2 - \frac{9}{4}\right)N + J_{tb}\mathbf{S}_t\cdot\mathbf{S}_b N. \tag{4.7}$$

Assuming that the two coupling constants are identical in the two sublayers, i.e., $J_t = J_b = J$, the total Hamiltonian becomes

$$\mathcal{H} = J\left(S_t^2 + S_b^2 - \frac{9}{2}\right)N + J_{tb}\mathbf{S}_t\cdot\mathbf{S}_b N. \tag{4.8}$$

We can now introduce the angle ϕ between $\mathbf{S}_t$ and $\mathbf{S}_b$, such that

$$\mathcal{H} = J\left(S_t^2 + S_b^2 - \frac{9}{2}\right)N + J_{tb}NS_tS_b\cos\phi. \tag{4.9}$$

The constant shift will be neglected since it has no influence on the choice of groundstate. Further, the length of the spins in the two sublayers are assumed to be identical, i.e., $S_t = S_b = S$, such that the Hamiltonian can be written as

$$\mathcal{H} = S^2N\left(2J + J_{tb}\cos\phi\right). \tag{4.10}$$

The total Hamiltonian is minimized to find the groundstate. The groundstate configuration of the spins depends on the sign of both J and J_{tb}. If both J and J_{tb} are negative, it is trivial to see that the Hamiltonian is minimized for $\phi = 0$ and maximized spin. This yields both an intralayer and interlayer ferromagnetic coupling. This groundstate configuration is depicted in **Fig. 4.3** (a).

If $J < 0$ but $J_{tb} > 0$, Eq. (4.10) is minimized for maximized spin and $\phi = \pi$, since this makes the second term negative. This results in a ferromagnetic coupling between the spins in the sublayers, though the total spin of each sublayer couple antiferromagnetically since $\phi = \pi$. This groundstate configuration is depicted in **Fig. 4.3** (b). When J is positive the groundstate configuration depends on the relative size of J and J_{tb}.

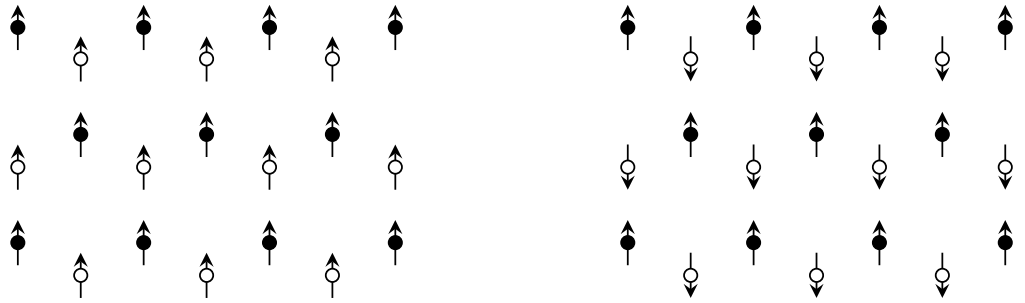

(a) (b)

Fig. 4.3: Illustration of a groundstate configuration exhibiting ferromagnetic interlayer coupling (a) and antiferromagnetic interlayer coupling (b). Both spin configurations exhibit a ferromagnetic intralayer coupling. The black and white circles represent the Yb sites in the top and bottom sublayer, respectively.

If J_{tb} is below (above) the line $J_{tb} = 2J$ ($J_{tb} = -2J$), Eq. (4.10) can never become negative, and it is minimized for $S = 0$. This is a non-magnetic phase. Since the spins are located in a triangular lattice, this means that they are oriented with an angle of $2\pi/3$ between all spins in the sublayer. This is illustrated in **Fig. 4.4**.

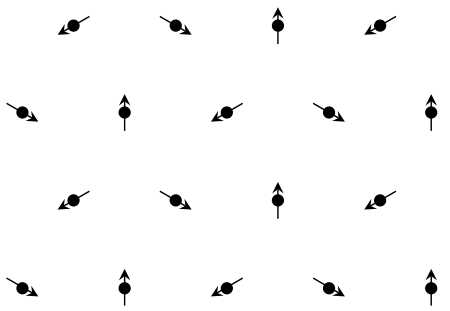

Fig. 4.4: Groundstate configuration of the spins on the Yb sites of one sublayer with $S = 0$.

If J_{tb} is positive and above the line $J_{tb} = 2J$, the energy is minimized for $\phi = \pi$. If J_{tb} is below the line $J_{tb} = -2J$, it is minimized for $\phi = 0$. Both cases are minimized for $S = S_{max}$, where S_{max} denotes the maximal length of the total spin, namely $S_{max} = 3/2$. The phasediagram of J and J_{tb} is illustrated in **Fig. 4.5**.

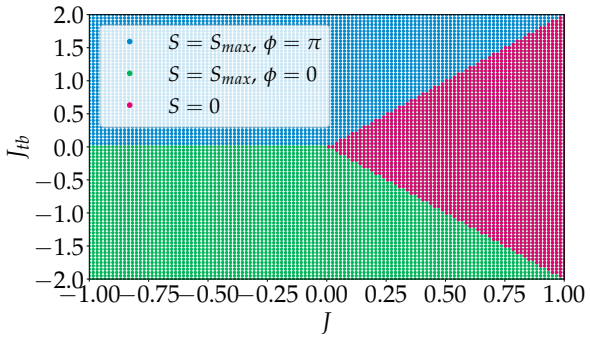

Fig. 4.5: Phase diagram of intra- and interlayer exchange coupling constants J and J_{tb}.

Including an External Magnetic Field

An external magnetic field, $\mathbf{B}$, will now be introduced. Including only the top sublayer, the Hamiltonian can be written as

$$\mathcal{H}_t^B = J_t \sum_{\langle ij \rangle} \mathbf{S}_i \cdot \mathbf{S}_j + g\mu_B \sum_i \mathbf{S}_i \cdot \mathbf{B}, \tag{4.11}$$

where $g \simeq 2$ is the Landé g-factor and μ_B is the Bohr magneton. Evaluating the sums and introducing the length of the spins, as in the previous section, the Hamiltonian becomes

$$\mathcal{H}_t^B = NJ_tS_t^2 - \text{const.} + Ng\mu_B\mathbf{B} \cdot \mathbf{S}_t \simeq NJ_tS_t^2 + Ng\mu_BBS_t\cos\theta. \tag{4.12}$$

Again, the constant shift is neglected. Further, θ, the angle between the total spin and the magnetic field, has been introduced. For $J_t < 0$ this Hamiltonian is minimized for $S = S_{max}$ and $\theta = \pi$. The case where $J_t > 0$ is slightly more complicated. The derivatives

$$\frac{\partial \mathcal{H}_t^B}{\partial S_t} = 2NJ_tS_t + Ng\mu_BB\cos\theta = 0, \tag{4.13}$$

$$\frac{\partial \mathcal{H}_t^B}{\partial \theta} = -Ng\mu_BBS\sin\theta = 0, \tag{4.14}$$

can be obtained. From Eq. (4.14), assuming that the magnetic field is non-zero, either the length of the spin or $\sin\theta$ must be zero. The condition $\sin\theta = 0$ requires that $\theta = n\pi$, for even n. For the second term in the Hamiltonian to be minimized, see Eq. (4.12), it is trivial to see that $\theta = \pi$ is the solution. Thus, the total spin is antiparallel to the magnetic field. Inserting this in Eq. (4.13), the length of the spin is found to be

$$S_t = \frac{g\mu_BB}{2J_t}. \tag{4.15}$$

Remember that $S_t = S_{1t} + S_{2t} + S_{3t}$. This means that the sum of the three spins in the unit cell will sum up to give this number. For a small external magnetic field, the total spin will be just above zero, and for increasing magnetic fields, the size of S_t will

increase until it reaches maximal value, i.e., when all spins in the unit cell are parallel. Inserting these results in the Hamiltonian we find the groundstate energy to be

$$E_t^B = -\frac{Ng^2\mu_B^2 B^2}{4J_t}. \tag{4.16}$$

This is a lower energy than for $S_t = 0$, so Eq. (4.16) is the groundstate energy for $J_t > 0$. That the spin is antiparallel to the magnetic field means that the spin magnetic moment is parallel to the magnetic field, due the negative sign in

$$\boldsymbol{\mu}_S = -\frac{e}{2m} g\mathbf{S}, \tag{4.17}$$

where e and m is the charge and mass of the relevant particle, respectively. If the magnetic moment is only present due to the presence of the external magnetic field, the material is paramagnetic. Now we include both sublayers, and the coupling between them, together with the magnetic field. In this case the Hamiltonian is given by

$$\mathcal{H} = J\left(S_t^2 + S_b^2 - \frac{9}{2}\right)N + J_{tb}\mathbf{S}_t \cdot \mathbf{S}_b N + g\mu_B \mathbf{B} \cdot (\mathbf{S}_t + \mathbf{S}_b)N. \tag{4.18}$$

As previously we assume that $J_t = J_b = J$. When both J and J_{tb} are negative, a ferromagnetic coupling arise between the spins in the sublayers and between the sublayers as illustrated in **Fig. 4.3** (a). These spins will be antiparallel to the external magnetic field. If both $J > 0$ and $J_{tb} > 0$, the second term is minimized if $\mathbf{S}_t$ and $\mathbf{S}_b$ are antiparallel. Assuming this, and that the magnetic field is perpendicular to the spins, the inner products can be parametrized using only one angle ϕ, i.e., the angle between $\mathbf{S}_t$ and $\mathbf{B}$, and $\mathbf{S}_b$ and $\mathbf{B}$. Thus, the angle between $\mathbf{S}_t$ and $\mathbf{S}_b$ is 2ϕ. The Hamiltonian can then be written as

$$\mathcal{H} = JN\left(S_t^2 + S_b^2\right) + J_{tb}NS_tS_b\cos 2\phi + Ng\mu_B B(S_t + S_b)\cos\phi. \tag{4.19}$$

The length of the two summed spins are assumed to be identical, i.e., $S_t = S_b = S$, such that the Hamiltonian can be written as

$$\mathcal{H} = NS^2(2J + J_{tb}\cos 2\phi) + 2Ng\mu_B BS\cos\phi. \tag{4.20}$$

This Hamiltonian can now be minimized with respect to ϕ and S for various magnitudes of J_{tb} and B. A phase diagram for J_{tb}/J and B/μ_B can thus be found numerically. This results in three different regimes, see **Fig. 4.6**.

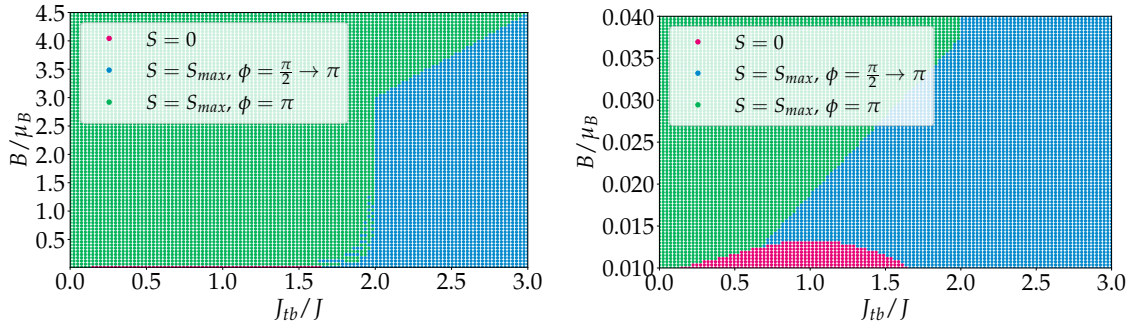

Fig. 4.6: Phase diagram between the two parameters, $\frac{B}{\mu_B}$ and $\frac{J_{tb}}{J}$ for small (a) and bigger (b) external magnetic fields for $J_{tb} > 0$ and $J > 0$.

When J_{tb}/J is small the Hamiltonian is minimized for the maximal value of S, and with $\phi = \pi$. This is viewed as the green area in the phase diagram, see **Fig. 4.6** (a). Remember that ϕ is the angle between S and B such that the angle between the total spins of the two sublayers are twice this angle. The condition $S = S_{max}$ means that the three spins in the unit cell of one layer are parallely oriented, whereas the condition $\phi = \pi$ requires that the total spin of each layer is parallel to each other. The material is thus ferromagnetic in this regime as illustrated in **Fig. 4.3** (a), and the spins are pointing antiparallel to the external magnetic field. In the pink regime the Hamiltonian is minimized for $S = 0$ and this is a non-magnetic regime. This configuration is depicted in **Fig. 4.4**. In the last regime, i.e., for bigger J_{tb}/J, the Hamiltonian is minimized for $S = S_{max}$ and $\phi = \frac{\pi}{2} \to \pi$ for increasing magnetic fields. At which magnitude of the field ϕ reaches ϕ depends on the magnitude of J_{tb}/J. The same phase diagram for small magnetic fields is shown in **Fig. 4.6** (b). Here, the non-magnetic regime is clearly observed. Looking at the Hamiltonian, see Eq. (4.20), we can try to understand these results analytically.

When J_{tb} is smaller than $2J$, the first terms can never become negative regardless of the value of ϕ. Thus, it is trivial to see that the Hamiltonian is minimized for $S = 0$ for small magnetic fields and for greater magnetic fields when the latter term is negative, i.e., when $\phi = \pi$. When J_{tb} becomes greater than J, the first term can now become negative. Thus, for a small magnetic field it is advantegous to maximize the length of the spins and choose $\phi = \pi/2$. In this case the term with the magnetic field becomes zero. For increasing magetic fields the last term in Eq. (4.20) becomes more dominent until the magnitude of this surpasses the other two and $\phi = \pi$. The non-magnetic region with $S = 0$ is much smaller in the presence of the external magnetic field. Thus, in a specific part of the phase diagram between J_{tb} and J, the compound is paramagnetic in agreement with experimental results [25].

For $J > 0$ and $J_{tb} < 0$ Eq. (4.20) is minimized for $\phi = \pi$. For small magnetic fields the spin is just above zero though it increases with increasing magnetic field until it reaches the maximal value. The magnitude of the field at which the spin reaches the maximal value depends on the relative size of J_{tb} compared to J, see **Fig. 4.7** (a).

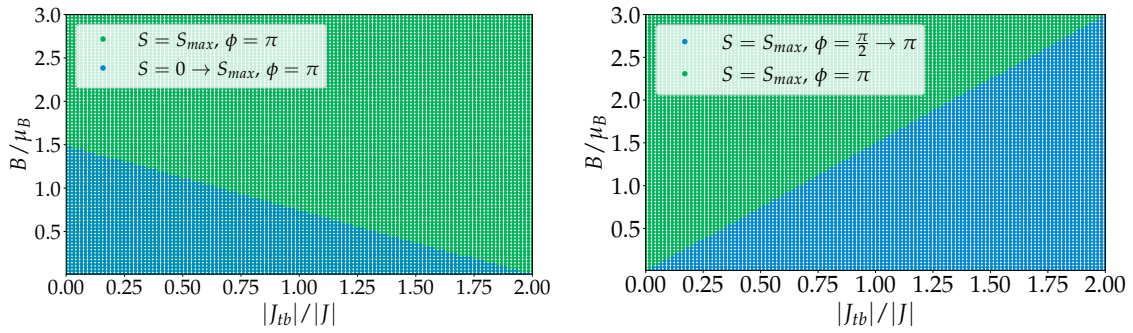

(a) (b)

Fig. 4.7: Phase diagram between $\frac{B}{\mu_B}$ and $\frac{J_{tb}}{J}$ for $J_{tb} < 0$ and $J > 0$ (a), and for $J_{tb} > 0$ and $J < 0$ (b) .

When $J < 0$ and $J_{tb} > 0$ Eq. (4.20) is minimized for $S = S_{max}$ everywhere, though ϕ varies. For small magnetic fields $\phi = \pi/2$ which set both the term including B to zero and makes the term including J_{tb} negative. For increasing magnetic fields, $\phi \to \pi$. The magnitude of the field at which $\phi = \pi$ depends on the relative size of J_{tb} compared to J, see **Fig. 4.7** (b).

4.3 Conclusion

Monolayer YbOCl has been studied in this section. Focusing on the single hole occupying each Yb site in a triangular lattice, these spin $\frac{1}{2}$ particles have been studied through the Heisenberg model. The groundstate of monolayer YbOCl was found to depend on the relative sizes of the exchange coupling constant between spins in the same sublayer J and the exchange interaction coupling strength between spins located in two different sublayers J_{tb}. Further, this depends on the sign of both J and J_{tb}. A non-magnetic region with $S = 0$ was obtained. Outside this region the Hamiltonian, see Eq. (4.10), was minimized for maximized total spin of one unit cell, though the size of ϕ depended on the sign and sizes of J_{tb} and J. One region exhibited antiferromagnetic interlayer coupling whereas the other exhibited ferromagnetic interlayer coupling between the spins. Both regions exhibited ferromagnetic intralayer couplings. All phases are depicted in **Fig. 4.5**. Thereafter, an external magnetic field was introduced. Again, the groundstate configuration was dependent on the relative size and signs of J_{tb} and J. For $J_{tb} < 0$ and $J < 0$ both a ferromagnetic intra- and interlayer magnetic coupling minimizes the Hamiltonian, see Eq. (4.20). These spins were oriented antiparallel to the magnetic field. For $J_{tb} > 0$ and $J > 0$, $J_{tb} > 0$ and $J < 0$ and $J_{tb} < 0$ and $J > 0$ various phases was observed. The phase digram between B/μ_B and J_{tb}/J for these three cases are depicted in **Fig. 4.6** and **Fig. 4.7**. Except for a small region with $S = 0$, the spins are oriented antiparallely to the external magnetic field. The non-magnetic region with $S = 0$ was much smaller in the presence of the external magnetic field. Thus, in a specific part of the phase diagram between J_{tb} and J, the compound is paramagnetic in agreement with the experimental results [25].

Chapter 5

VS_2

5.1 Introduction to VS_2

Vanadium disulfide (VS_2) is a TMD that corresponds to layers of S-V-S that, when stacked, form bulk VS_2. These layers couple through the VdW force. Two phases of crystal structure is observed for VS_2, i.e., the 2H and the 1T phases. The geometry of these will be introduced further below. In 2016 VS_2 was investigated by Wang et al. using DFT calculations [2]. This study showed that for monolayer VS_2 the 2H phase is more stable than the 1T phase, and oppositely for bulk VS_2. The DFT C2DB (computational 2D materials database) from DTU [3] agree with this. Both 2H monolayer VS_2 and 1T bulk VS_2 have been shown to exhibit metallic behaviour. As discussed previously many TMDs are semiconducting with low conductivity, including the highly investigated MoS_2, which is a disadvantage in several technologies, including energy storage. Wang et al. conclude that VS_2 exhibit a lower adsorption energy and a higher ion diffusion rate compared to other 2D materials. This makes both bulk and monolayer VS_2 promising candidates to be the anode material in sodium and lithium ion batteries. The disadvantage of VS_2 is that it exhibits poor stability due to Peierls distortion [27]. Lu li et al. reported that VS_2 can become stable in a lithium-ion battery by coating it with a $\simeq 2.5$ nm thick titanium disulfide layer, which is found from DFT to be less susceptible to Peierls distortion. Further, VS_2 has shown to exhibit ferromagnetic behaviour which suggests it to be a good candidate for spintronic devices [28].

In the following sections both the 1T and 2H phase of VS_2 will be investigated separately. To begin with, the model complex VS_6 will be studied. First, the tight binding model in the Slater Koster decomposition will be used to obtain the energy spectrum of the single molecule. This will be further studied in the subspace of the d-orbitals present on the vanadium atom. Using group theory the symmetries of the molecule will be investigated to understand the obtained energy spectrum. A specific high-symmetrical case of the 1T phase will be explored. Subsequently, monolayer VS_2 is considered. The band structures will be obtained using the tight binding model in the Slater Koster decomposition together with the Hubbard model. These band structures will be compared to DFT calculations.

5.2 Model Complex VS_6

Both the 1T and 2H structure of the hypothetical model complex VS_6 will be studied in the following to give an intuition of the compound prior the investigation of monolayer VS_2. A side view and a top view of these two phases are illustrated in **Fig. 5.1** and **Fig. 5.2**, respectively. The vanadium atom is stacked between two sublayers of sulfur atoms, which will be denoted the top (t) and bottom (b) sublayers. For the calculations in this section to be relevant, when considering monolayer VS_2, the stoichiometry for VS_2 and not VS_6 will be used here. One unit cell of VS_2 only consists of two sulfur atoms; this will be introduced further in the **Chapter 5.3**. Vanadium and sulfur have the electron configurations $[Ar]4s^2 3d^3$ and $[Ne]3s^2 3p^4$, respectively. Both sulfur atoms in the unit cell will acquire two electrons from the vanadium atom to fill their outermost p-shells. Thus, a unit cell is made up of two S^{2-}-ions and one V^{4+}-ion. This leaves a single electron in an unfilled d-shell on the vanadium atom.

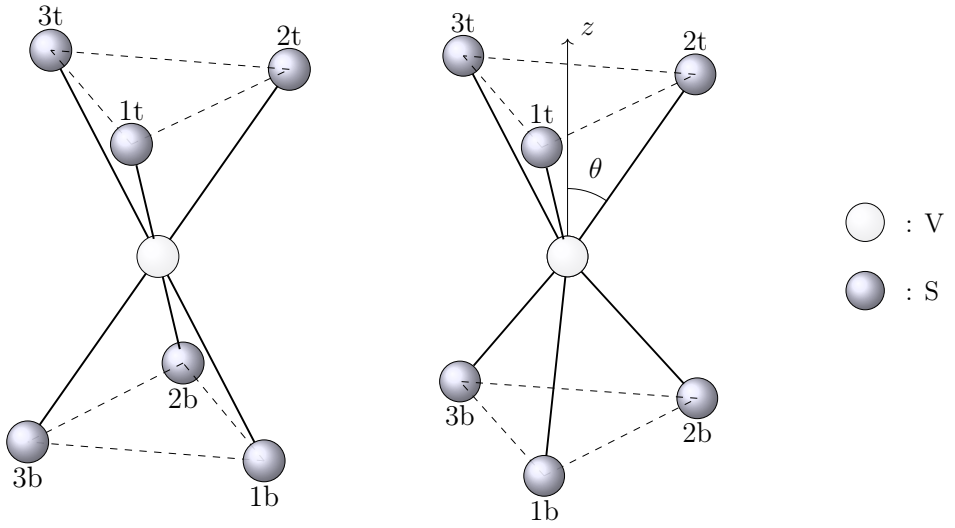

(a) 1T (b) 2H

Fig. 5.1: The 1T (a) and 2H phase (b) of the molecule VS_6 for $\theta = 37°$, where θ is the angle between the z-axis and the sulfur atoms in the top sublayer of the molecule as indicated. The white atoms illustrates the vanadium atom in the middle sublayer and the grey atoms illustrates the sulfur atoms in the top (t) and bottom (b) sublayer.

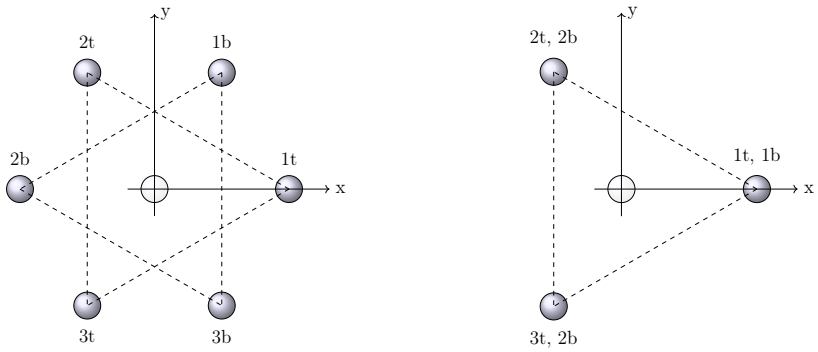

(a) 1T (b) 2H

Fig. 5.2: Top view of the 1T (a) and 2H structure (b) of the molecule VS_6. Furthermore, the chosen coordinate system is depicted.

The energy spectrum can be obtained using the tight binding model, which in second quantization can be written as

$$\hat{\mathcal{H}}_t = \xi \sum_{i,\sigma} \hat{c}^\dagger_{i,\sigma} \hat{c}_{i,\sigma} - t \sum_{\langle i,j \rangle} \sum_{\sigma} \left(\hat{c}^\dagger_{i,\sigma} \hat{c}_{j,\sigma} + h.c. \right). \tag{5.1}$$

Here ξ refer to the onsite energies, t is the hopping integral and h.c. refers to the Hermitian conjugate terms. $\hat{c}^\dagger_{i,\sigma}$ and $\hat{c}_{i,\sigma}$ are the creation and annihilation operators, respectively, for an electron on site i with spin σ. Only nearest neighbour interactions are included. For simplicity the spin-indices will be omitted in the following. In both the 1T and the 2H phase there is six times three p-orbitals and one times five d-orbitals. The Hamiltonian in Eq. (5.1) can now be written in matrix form in the basis of these orbitals in the following order

$$\begin{aligned} |\Psi\rangle = \{&|d_{xy}\rangle, |d_{yz}\rangle, |d_{zx}\rangle, |d_{x^2-y^2}\rangle, |d_{z^2}\rangle, |p^{1t}_x\rangle, |p^{1t}_y\rangle, |p^{1t}_z\rangle, |p^{2t}_x\rangle, |p^{2t}_y\rangle, |p^{2t}_z\rangle, \\ &|p^{3b}_x\rangle, |p^{3b}_y\rangle, |p^{3b}_z\rangle, |p^{1b}_x, p^{1b}_y\rangle, |p^{1b}_z\rangle, |p^{2b}_x\rangle, |p^{2b}_y\rangle, |p^{2b}_z\rangle, |p^{3b}_x\rangle, |p^{3b}_y\rangle, |p^{3b}_z\rangle\}, \end{aligned} \tag{5.2}$$

as

$$\mathcal{H} = \begin{bmatrix} \mathcal{H}_d & V_{dp} \\ V_{pd} & \mathcal{H}_p \end{bmatrix}. \tag{5.3}$$

$\mathcal{H}_d$ is a diagonal 5x5 matrix with ξ_d on the diagonal whereas $\mathcal{H}_p$ is a 18x18 matrix with ξ_p on the diagonal, where ξ_d and ξ_p are the onsite energies of the d- and p-orbitals, respectively. Thus, the onsite energies of all p-orbitals are assumed to be degenerate prior the interaction with the d-orbitals and similar for the d-orbitals. The two off-diagonal blocks of the Hamiltonian V_{dp} and V_{pd} couple the d-orbitals to the p-orbitals and vice versa.

The elements of V_{dp} and V_{pd} can be written in terms of the interatomic matrix elements $E_{i,j}(\mathbf{r}_{n,n'}) = \langle n, i|\hat{\mathcal{H}}_t|n', j\rangle$ found by John Clarke Slater and George Fred Koster [29],

$$E_{x,xy} = \sqrt{3}l^2 m V_{pd\sigma} + m(1-2l^2)V_{pd\pi}, \tag{5.4}$$
$$E_{x,yz} = \sqrt{3}lmn V_{pd\sigma} - 2lmn V_{pd\pi}, \tag{5.5}$$
$$E_{x,zx} = \sqrt{3}l^2 n V_{pd\sigma} + n(1-2l^2)V_{pd\pi}, \tag{5.6}$$
$$E_{x,x^2-y^2} = \frac{\sqrt{3}}{2}l(l^2-m^2)V_{pd\sigma} + l(1-l^2+m^2)V_{pd\pi}, \tag{5.7}$$
$$E_{y,x^2-y^2} = \frac{\sqrt{3}}{2}m(l^2-m^2)V_{pd\sigma} - m(1+l^2-m^2)V_{pd\pi}, \tag{5.8}$$
$$E_{z,x^2-y^2} = \frac{\sqrt{3}}{2}n(l^2-m^2)V_{pd\sigma} - n(l^2-m^2)V_{pd\pi}, \tag{5.9}$$
$$E_{x,3z^2-r^2} = l\left[n^2-(l^2+m^2)/2\right]V_{pd\sigma} - \sqrt{3}ln^2 V_{pd\pi}, \tag{5.10}$$
$$E_{y,3z^2-r^2} = m\left[n^2-(l^2+m^2)/2\right]V_{pd\sigma} - \sqrt{3}mn^2 V_{pd\pi}, \tag{5.11}$$
$$E_{z,3z^2-r^2} = n\left[n^2-(l^2+m^2)/2\right]V_{pd\sigma} + \sqrt{3}n(l^2+m^2)V_{pd\pi}, \tag{5.12}$$

where $\hat{\mathcal{H}}_t$ is the tight binding Hamiltonian in Eq. (5.1). The matrix elements not stated here can be found by cyclically permuting x, y and z. For simplicity, the $3r^2-z^2$ d-orbital will be referred to as the z^2 d-orbital. $V_{pd\pi}$ and $V_{pd\sigma}$ are the bond integrals for π and σ bonds, respectively. A method for obtaining an estimate of the numerical values of these is given in **Appendix A**. Further, the interatomic matrix elements are expressed in terms of the normalized vector between the vanadium atom and the sulfur atoms $\mathbf{r} = (r_x, r_y, r_z) = d(l, m, n)$, where we have chosen $d = 1$, and l, m and n is given by

$$l = \sin\theta\cos\phi \quad , \quad m = \sin\theta\sin\phi \quad , \quad n = \cos\theta. \tag{5.13}$$

To obtain the numerical values for l, m and n for the atoms in the molecule the coordinate system depicted in **Fig. 5.1** can be transformed into spherical coordinates, and θ and ϕ for each atom can be obtained. The interatomic matrix elements can thus be found for each sulfur atom.

5.2.1 1T Structure

First, the 1T structure will be considered. The eigenenergies of the 23x23 matrix, see Eq. (5.3), is obtained numerically, setting $\xi_d = 0$, $\xi_p = 1$, $\frac{V_{pd\sigma}}{\xi_p} = 0.35$, $\frac{V_{pd\pi}}{\xi_p} = 0.1$ and $\theta = 37°$. σ bonds are in generel stronger than π bonds, since this allows the electrons to mainly be localized between the two nuclei; therefore, we choose $V_{pd\sigma} > V_{pd\pi}$. We are seeking the bonding orbitals of the d-electron, so we focus on the five lowest eigenenergies. These should all be below zero since $\xi_d = 0$. In **Fig. 5.3** these eigenenergies are depicted together with the orbitals included in the eigenvector for the given eigenenergy. It is evident that two of the three energy levels are two-fold degenerate. This problem can be simplified by projecting into the d-subspace.

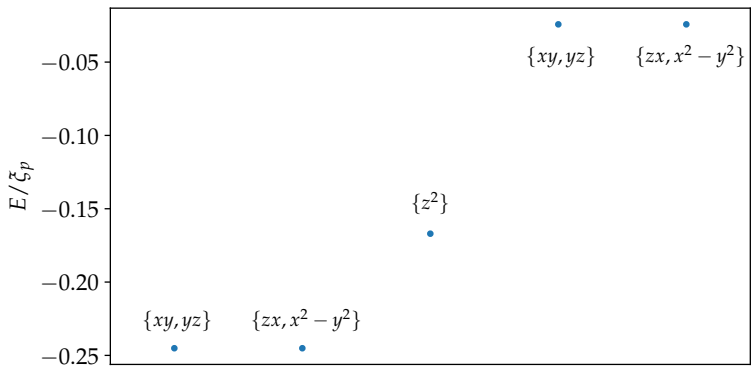

Fig. 5.3: Illustration of the five lowest eigenenergy levels E, obtained numerically from the 23x23 matrix in Eq. (5.3) with $\xi_d = 0$, $\xi_p = 1$, $\frac{V_{pd\sigma}}{\xi_p} = 0.35$, $\frac{V_{pd\pi}}{\xi_p} = 0.1$ and $\theta = 37°$ for 1T-VS_6. The orbitals included in the eigenstates of each eigenenergy are illustrated.

Subspace of the d-orbitals

The Hamiltonian describing the system can be split up into a part that describes the d-orbitals, a part that describes the p-orbitals and then a term that describes the interaction between these orbitals,

$$\hat{\mathcal{H}} = \hat{\mathcal{H}}_p + \hat{\mathcal{H}}_d + \hat{V}. \tag{5.14}$$

Since we are only investigating a single electron, the eigenstate can be expressed as a sum of a p- and d-part of the state[1] as

$$|\psi\rangle = |\psi_p\rangle + |\psi_d\rangle. \tag{5.15}$$

The projection operators $\hat{\mathscr{P}}_d$ and $\hat{\mathscr{P}}_p$ for the d-subspace and the p-subspace, respectively, can be applied to rewrite the Hamiltonian. These projection operators must sum to identity, $\hat{\mathscr{P}}_p + \hat{\mathscr{P}}_d = \mathbb{1}$, and are defined to project the eigenstate of the full Hamiltonian into the subspace of either the d- or the p-orbitals, as

$$\hat{\mathscr{P}}_d|\psi\rangle = E|\psi_d\rangle \quad , \quad \hat{\mathscr{P}}_p|\psi\rangle = E|\psi_p\rangle. \tag{5.16}$$

Using these two operators yields

$$\hat{\mathcal{H}}_d|\psi_d\rangle + \hat{V}_{dp}|\psi_p\rangle = E|\psi_d\rangle, \tag{5.17}$$

$$\hat{\mathcal{H}}_p|\psi_p\rangle + \hat{V}_{pd}|\psi_d\rangle = E|\psi_p\rangle. \tag{5.18}$$

Here V_{dp} and V_{pd} refer to the 5x18 and 18x5 off-diagonal blocks of Eq. (5.3), respectively, as described in the previous section. Isolating $|\psi_p\rangle$ in Eq. (5.18) and inserting this in Eq. (5.17) leads to the expression

$$\hat{\mathcal{H}}_d|\psi_d\rangle + \hat{V}_{dp}\frac{1}{E - \hat{\mathcal{H}}_p}\hat{V}_{pd}|\psi_d\rangle = E|\psi_d\rangle. \tag{5.19}$$

[1]For a multi-electron system this would be a product not a sum.

Using that $|\psi_d\rangle$ and $|\psi_p\rangle$ are eigenstates of $\hat{\mathcal{H}}_d$ and $\hat{\mathcal{H}}_p$, respectively, and introducing the eigenenergy of $V_{dp}V_{pd}$ as ξ^2, this can be written as

$$\xi_d|\psi_d\rangle + \frac{\xi^2}{E-\xi_p}|\psi_d\rangle = E|\psi_d\rangle. \tag{5.20}$$

Setting $\xi_d = 0$, E is isolated as

$$E_\pm = \frac{\xi_p}{2}\left(1 \pm \sqrt{1+\left(\frac{2\xi}{\xi_p}\right)^2}\right). \tag{5.21}$$

Since we are seeking the bonding orbitals and since ξ_p is chosen to be positive, the plus solution is discarded. Numerically, all ξ's are found to be positive both for the 1T and 2H structure and thus all E's are found to be negative, as expected. Thus, knowing the eigenenergies of the 5x5 Hamiltonian $V_{pd}^\dagger V_{pd}$ in the d-subspace, the five lowest eigenenergies of the full Hamiltonian can be found from

$$E = \frac{\xi_p}{2}\left(1 - \sqrt{1+\left(\frac{2\xi}{\xi_p}\right)^2}\right). \tag{5.22}$$

Therefore, in the d-subspace the same degeneracy is observed as in **Fig. 5.3**. Each eigenstate is a superposition of d-orbitals, which can be found by investigating the numerically obtained eigenvectors in the d-subspace. The orbitals included in the eigenvectors of each eigenvalue are indicated in **Fig. 5.3**. The eigenvector of one of the two lowest eigenenergies of the 5x5 matrix is a linear combination of the xy d-orbital and the yz d-orbital. The other is a linear combination of the zx d-orbital and the x^2-y^2 d-orbital. Similar results were found for the two degenerate high energy levels. This indicates that xy and yz only couples to each other and similarly for zx and x^2-y^2. Further, it indicates that they couple in exactly the same way such that the energy level splitting results in degeneracy. The non-degenerate energy level in the middle is fully expressed in terms the z^2 d-orbital. This indicates that the z^2 d-orbital does not couple to any of the other d-orbitals. Now the question is why only some d-orbitals couple to each other and further why xy and yz couple in the same way as zx and x^2-y^2. To be able to answer these questions, the symmetries of the 1T-VS_6 must be explored. This will be considered in **section 5.2.1**. First, the d-subspace will be investigated in a more analytical manner. The matrix $V_{dp}V_{pd}$ expressed in terms of $V_{pd\pi}$, $V_{pd\sigma}$ and θ in the basis $\{xy, yz, zx, x^2-y^2, z^2\}$ can be written analytically as

$$V_{pd}^\dagger V_{pd} = \begin{bmatrix} M_{1,1} & M_{1,2} & 0 & 0 & 0 \\ M_{1,2} & M_{2,2} & 0 & 0 & 0 \\ 0 & 0 & M_{2,2} & -M_{1,2} & 0 \\ 0 & 0 & -M_{1,2} & M_{1,1} & 0 \\ 0 & 0 & 0 & 0 & M_{5,5} \end{bmatrix}, \tag{5.23}$$

with

$$M_{1,1} = \frac{3}{4}\sin^2\theta\left(4V_{pd\pi}^2(1+\cos^2\theta) + 3V_{pd\sigma}^2\sin^2\theta\right), \tag{5.24}$$

$$M_{1,2} = \frac{3}{2}\left(4V_{pd\pi}^2 - 3V_{pd\sigma}^2\right)\cos\theta\sin^3\theta, \tag{5.25}$$

$$M_{2,2} = \frac{3}{4}\left[4V_{pd\pi}^2\left(\frac{1}{2} + \cos^2\theta + \cos 4\theta\right) + 3V_{pd\sigma}^2\sin^2 2\theta\right], \tag{5.26}$$

$$M_{5,5} = \frac{3}{8}\left[12V_{pd\pi}^2\sin^2 2\theta + V_{pd\sigma}^2(3\cos 2\theta + 1)^2\right]. \tag{5.27}$$

It is clear from Eq. (5.23) that the reduced matrix is block diagonal. Further, the eigenvalues of the two 2x2 blocks are identical and the z^2-orbital is not coupling to any of the other d-orbitals.

Symmetry of the 1T phase

By inspection of the symmetries of the compound, 1T-VS_6 is found to belong to the point group $\mathbf{D_{3d}}$ for $\theta = 37°$ and can therefore be described by its character table viewed in **Table 5.1**. As always one element of the group is identity. Looking at **Fig. 5.1** it is clear that the molecule is symmetric in rotations of $\pm 2\pi/3$ around the z-axis. This gives the two elements $2C_3$ seen in the character table. Further, it is symmetric in rotations of π around a vector pointing from the origin in a direction parallel to the vector from p-orbital $1t$ to p-orbital $2t$ but with a zero z-component. This transformation lets $3t \to 1b$, $1t \to 3b$ and $2t \to 2b$. Similar rotations around the vector between $2t$ and $3t$ and the vector between $1t$ and $3t$ exists. This is the three C_2' elements. Inversion, represented by the element i, lets $x \to -x$, $y \to -y$ and $z \to -z$. Further, the Hamiltonian is invariant under a rotation of $\pm\pi/2$ around the z-axis followed by a reflection in the xy-plane. This transformation is represented by the two S_6 elements. Lastly, the molecule is symmetric under reflection in the planes spanned by the coupling lines, referred to as σ_d. This results in a total number of twelve symmetry elements. The dimensionality theorem, see Eq. (2.7), can only be obeyed by four one-dimensional irreducible representations and two two-dimensional irreducible representations, thus leading to a total number of six irreducible representations. The characters of these can be read off in **Table 5.1**. Further, this table illustrates which irreducible representations different quadratic functions belong to. This is very useful when investigating d-orbitals that can be described by quadratic functions. What it means that a quadratic function belong to a specific representation will become clear below.

$\mathbf{D_{3d}}$	E	$2C_3$	$3C_2'$	i	$2S_6$	$3\sigma_d$	Quadratic Functions
A_{1g}	1	1	1	1	1	1	(x^2+y^2, z^2)
A_{2g}	1	1	-1	1	1	-1	–
E_g	2	-1	0	2	-1	0	$(x^2-y^2, xy)(zx, yz)$
A_{1u}	1	1	1	-1	-1	-1	–
A_{2u}	1	1	-1	-1	-1	1	–
E_u	2	1	1	1	1	1	–

Table 5.1: Character table of the $\mathbf{D_{3d}}$ point group [30].

From the character table of $\mathbf{D_{3d}}$ we see that all d-orbitals, except for d_{z^2}, belongs to the same representation, namely the E_g representation. These four d-orbitals in the E_g representation are, however, still split into two "groups" marked by parentheses so, what does this mean? We know from the numerical results that xy only couples to x^2-y^2 and that zx only couples to yz. To understand why, and answer the question of why they couple identically, we need to explore the symmetries of the 1T phase of the molecule further. First, a reducible representation of the symmetry operators will be formulated, which is used to apply the projection operator in Eq. (2.22) to the various d-orbitals. This motivates a formulation of an irreducible representation of the symmetry operations. Using this the matrix elements of Eq. (5.23) can be investigated.

The relevant symmetry operators can be written in this three-dimensional reducible representation using the coordinate system depicted in **Fig. 5.2**, as

$$
\begin{aligned}
&\Gamma(E) = \begin{bmatrix} 1 & 0 & 0 \\ 0 & 1 & 0 \\ 0 & 0 & 1 \end{bmatrix}, \qquad \Gamma(i) = \begin{bmatrix} -1 & 0 & 0 \\ 0 & -1 & 0 \\ 0 & 0 & -1 \end{bmatrix}, \\
&\Gamma(C_3(2\pi/3)) = \begin{bmatrix} \cos\left(\frac{2\pi}{3}\right) & -\sin\left(\frac{2\pi}{3}\right) & 0 \\ \sin\left(\frac{2\pi}{3}\right) & \cos\left(\frac{2\pi}{3}\right) & 0 \\ 0 & 0 & 1 \end{bmatrix}, \\
&\Gamma(C_3(-2\pi/3)) = \Gamma(C_3)^2, \\
&\Gamma(S_6(\pi/3)) = \begin{bmatrix} 1 & 0 & 0 \\ 0 & 1 & 0 \\ 0 & 0 & -1 \end{bmatrix} \begin{bmatrix} \cos\left(\frac{\pi}{3}\right) & -\sin\left(\frac{\pi}{3}\right) & 0 \\ \sin\left(\frac{\pi}{3}\right) & \cos\left(\frac{\pi}{3}\right) & 0 \\ 0 & 0 & 1 \end{bmatrix}, \\
&\Gamma(-S_6) = \Gamma(S_6(-\pi/3)).
\end{aligned}
\tag{5.28}
$$

Here, $2C_2''$ and $3\sigma_d$ have been excluded since the characters of these symmetry operations are zero in the E_g representation. We can show that the xy-orbital is in fact in the E_g representation by projecting the xy-orbital into this representation. Using Eq. (2.27)

we get

$$\begin{aligned}\hat{\mathscr{P}}(E_g)\,xy &= \frac{l_{E_g}}{h}\sum_R \chi^{E_g}(R)^*\hat{P}_R\,xy \\ &= \frac{2}{12}\left[2\hat{P}_E - \hat{P}_{C_3} - \hat{P}_{C_3^2} + 2\hat{P}_i - \hat{P}_{S_6(\pi/3)} - \hat{P}_{S_6(-\pi/3)}\right]xy \\ &= \frac{1}{6}\Bigg[2xy - \left(-\frac{xy}{2} - \frac{\sqrt{3}}{4}(x^2-y^2)\right) - \left(-\frac{xy}{2} + \frac{\sqrt{3}}{4}(x^2-y^2)\right) + 2xy \\ &- \left(-\frac{xy}{2} + \frac{\sqrt{3}}{4}(x^2-y^2)\right) - \left(-\frac{xy}{2} - \frac{\sqrt{3}}{4}(x^2-y^2)\right)\Bigg] \\ &= xy. \end{aligned} \tag{5.29}$$

The x^2-y^2 orbital is defined as $-\frac{1}{2}(x^2-y^2)$ where the $1/2$ is a normalization factor. Since this gives back xy it must indeed belong to this representation. That a quadratic function belong to a particular representation therefore means that applying the symmetry operators in the group multiplied with the characters in that representation leaves the quadratic function invariant. A similar calculation can be done for x^2-y^2, yz and zx which yields the same conclusion. Here it is also seen that the xy orbital only mixes with the x^2-y^2 orbital when either one of the symmetry operations are applied. Focusing on the S_6 symmetry we see that

$$\hat{P}_{S_6}\,xy = -\frac{xy}{2} - \frac{\sqrt{3}}{2}\left(-\frac{1}{2}\left[x^2-y^2\right]\right), \tag{5.30}$$

$$\hat{P}_{S_6}\,yz = -\frac{yz}{2} - \frac{\sqrt{3}}{2}zx, \tag{5.31}$$

$$\hat{P}_{S_6}\left(-\frac{1}{2}\left[x^2-y^2\right]\right) = -\frac{1}{2}\left(-\frac{1}{2}\left[x^2-y^2\right]\right) + \frac{\sqrt{3}}{2}xy, \tag{5.32}$$

$$\hat{P}_{S_6}\,zx = -\frac{zx}{2} + \frac{\sqrt{3}}{2}yz. \tag{5.33}$$

From these four equations it is evident that xy and x^2-y^2 only mix together when $\hat{P}_{S_6}$ is applied and similar for zx and yz. Further, we see that xy mixes with x^2-y^2 in exactly the same way as yz mixes with zx. A similar pattern can be seen applying any other symmetry operator on these four d-orbitals.

These transformations can be used to write a two-dimensional irreducible representation of the operators in the $\mathbf{D_{3d}}$ point group according to the E_g representation in the basis $\{xy, (x^2 - y^2)\}$ as

$$\Gamma(E) = \Gamma^{(j)}(i) = \begin{bmatrix} 1 & 0 \\ 0 & 1 \end{bmatrix}, \tag{5.34}$$

$$\Gamma(C_3) = \Gamma(-S_6) = \begin{bmatrix} -\frac{1}{2} & \frac{\sqrt{3}}{2} \\ -\frac{\sqrt{3}}{2} & -\frac{1}{2} \end{bmatrix}, \tag{5.35}$$

$$\Gamma(S_6) = \Gamma(C_3^2) = \begin{bmatrix} -\frac{1}{2} & -\frac{\sqrt{3}}{2} \\ \frac{\sqrt{3}}{2} & -\frac{1}{2} \end{bmatrix}, \tag{5.36}$$

$$\Gamma(C_2''(1a - 2a)) = \Gamma(\sigma_d(3a)) = \begin{bmatrix} \frac{1}{2} & \frac{\sqrt{3}}{2} \\ \frac{\sqrt{3}}{2} & -\frac{1}{2} \end{bmatrix}, \tag{5.37}$$

$$\Gamma(C_2''(3a - 1a)) = \Gamma(\sigma_d(2a)) = \begin{bmatrix} \frac{1}{2} & -\frac{\sqrt{3}}{2} \\ -\frac{\sqrt{3}}{2} & -\frac{1}{2} \end{bmatrix}, \tag{5.38}$$

$$\Gamma(C_2''(3a - 2a)) = \Gamma(\sigma_a(1a)) = \begin{bmatrix} -1 & 0 \\ 0 & 1 \end{bmatrix}. \tag{5.39}$$

Writing these irreducible representations in the basis $\{yz, zx\}$ yields an identical result. This indicates that xy and yz does in fact couple in the same way as $(x^2 - y^2)$ and zx. Note that the characters of the irreducible representations in Eq. (5.34)-(5.39) agree with the characters listed in **Table 5.1**. The projection operator in Eq. (2.22) that projects a basis function onto the κth row of the jth representation can now be explored. First, yz is projected onto the first row of the irreducible representation

$$\begin{aligned}
\hat{\mathscr{P}}_{11}\, yz = \frac{1}{3}\Big[&\Gamma_{11}(E)\hat{P}_E + \Gamma_{11}(C_3)\hat{P}_{C_3} + \Gamma_{11}(C_3^2)\hat{P}_{C_3^2} + \Gamma_{11}(\sigma_d(1a))\hat{P}_{\sigma_d(1a)} \\
&+ \Gamma_{11}(\sigma_d(2a))\hat{P}_{\sigma_d(2a)} + \Gamma_{11}(\sigma_d(3a))\hat{P}_{\sigma_d(3a)}\Big] yz \\
= \frac{1}{3}\Bigg[&yz - \frac{1}{2}\left(-\frac{1}{2}yz + \frac{\sqrt{3}}{2}zx\right) - \frac{1}{2}\left(-\frac{1}{2}yz - \frac{\sqrt{3}}{2}zx\right) - (-yz) \\
&+ \frac{1}{2}\left(\frac{1}{2}yz - \frac{\sqrt{3}}{2}zx\right) + \frac{1}{2}\left(\frac{1}{2}yz + \frac{\sqrt{3}}{2}zx\right)\Bigg] \\
= &\, yz.
\end{aligned} \tag{5.40}$$

This verifies that yz belongs to the first row of the two-dimensional irreducible representation. Applying $\hat{\mathscr{P}}_{11}^{(j)}$ to xy yields the same conclusion. Similarly,

$$\begin{aligned}
&\hat{\mathscr{P}}_{22}^{(j)}\,(x^2 - y^2) = (x^2 - y^2), \quad \hat{\mathscr{P}}_{22}^{(j)}\, zx = zx, \\
&\hat{\mathscr{P}}_{22}^{(j)} yz = 0, \quad \hat{\mathscr{P}}_{22}^{(j)} xy = 0, \quad \hat{\mathscr{P}}_{11}^{(j)} zx = 0, \quad \hat{\mathscr{P}}_{11}^{(j)}(x^2 - y^2) = 0.
\end{aligned} \tag{5.41}$$

The overlap between xy and yz can now be obtained

$$\begin{aligned}\langle xy|\hat{\mathcal{H}}|yz\rangle &= \langle xy|\hat{U}(S_6)^\dagger\hat{U}(S_6)\hat{\mathcal{H}}\hat{U}(S_6)^\dagger\hat{U}(S_6)|yz\rangle = \langle xy|\hat{U}(S_6)^\dagger\hat{\mathcal{H}}\hat{U}(S_6)|y\rangle \\ &= \left(-\frac{1}{2}\langle xy| - \frac{\sqrt{3}}{2}\langle x^2-y^2|\right)\hat{\mathcal{H}}\left(-\frac{1}{2}|yz\rangle - \frac{\sqrt{3}}{2}|zx\rangle\right) \\ &= \frac{1}{4}\langle xy|\hat{\mathcal{H}}|yz\rangle + \frac{\sqrt{3}}{4}\langle xy|\hat{\mathcal{H}}|zx\rangle \\ &\quad + \frac{\sqrt{3}}{4}\langle x^2-y^2|\hat{\mathcal{H}}|yz\rangle + \frac{3}{4}\langle x^2-y^2|\hat{\mathcal{H}}|zx\rangle \\ &= \frac{1}{4}\langle xy|\hat{\mathcal{H}}|yz\rangle + \frac{3}{4}\langle x^2-y^2|\hat{\mathcal{H}}|zx\rangle. \end{aligned} \tag{5.42}$$

A unitary operator must always obey $\hat{U}(S_6)^\dagger\hat{U}(S_6) = \mathbb{1}$, and the first equality sign is obeyed. That this operator, as any other operator of the E_g representation, must leave the Hamiltonian invariant, requires that $\hat{U}(S_6)\hat{\mathcal{H}}\hat{U}(S_6)^\dagger = \hat{\mathcal{H}}$. Thereafter, $\hat{U}^\dagger(S_6)$ is applied on $\langle xy|$ and $\hat{U}(S_6)$ on $|yz\rangle$. This results in four terms of which the two are zero due to the fact that the involved orbitals belong to different rows of the irreducible representations, as shown above, and therefore do not couple. For the last equality sign to be obeyed, it is required that

$$\langle xy|\hat{\mathcal{H}}|yz\rangle = \langle x^2-y^2|\hat{\mathcal{H}}|zx\rangle. \tag{5.43}$$

This proves that the orbitals must couple in the same way, which leads to the degeneracy viewed in **Fig. 5.3**. The proof can be reproduced using any other symmetry of the E_g representation.

High symmetrical case of the 1T phase

Plotting all eigenenergies as a function of θ, the spectrum viewed in **Fig. 5.4** is obtained. In general there are three curves, as expected, two two-fold degenerate energies and one non-degenerate. The degeneracy increases at four points for $\theta \in [0, \pi]$, two of them which are marked with red lines, i.e., $\theta = \arctan(\sqrt{2})$ and $\theta = \pi - \arctan(\sqrt{2})$. A change in degeneracy indicates a change in the symmetry of the molecule, though accidental degeneracies can occur.

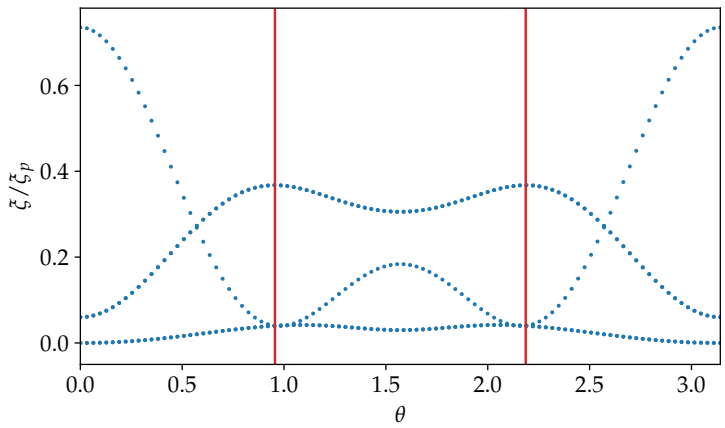

Fig. 5.4: The five eigenenergies of Eq. (5.23) as a function of θ with $\frac{V_{pd\sigma}}{\xi_p} = 0.35$ and $\frac{V_{pd\pi}}{\xi_p} = 0.1$. The two red lines marks $\theta = \arctan(\sqrt{2})$ and $\pi - \arctan(\sqrt{2})$.

The symmetry of the 1T molecule increases when all coupling lines are perpendicular to each other. Using the coordinate system depicted in **Fig. 5.2**, these three vectors can be written as

$$\mathbf{v}_{1t} = \begin{bmatrix} \sin\theta \\ 0 \\ \cos\theta \end{bmatrix}, \qquad \mathbf{v}_{2t} = \begin{bmatrix} \cos\left(\frac{2\pi}{3}\right)\sin\theta \\ \sin\left(\frac{2\pi}{3}\right)\sin\theta \\ \cos\theta \end{bmatrix}, \qquad \mathbf{v}_{3t} = \begin{bmatrix} \cos\left(-\frac{2\pi}{3}\right)\sin\theta \\ \sin\left(-\frac{2\pi}{3}\right)\sin\theta \\ \cos\theta \end{bmatrix}. \tag{5.44}$$

Demanding that $\mathbf{v}_{1t} \cdot \mathbf{v}_{2t} = 0$ results in the following angles

$$\theta = \begin{cases} -\arctan\left(\sqrt{2}\right) + 2\pi c_1, & c_1 \in \mathbb{Z} \\ \pi - \arctan\left(\sqrt{2}\right) + 2\pi c_1, & c_1 \in \mathbb{Z} \\ \arctan\left(\sqrt{2}\right) + 2\pi c_1, & c_1 \in \mathbb{Z} \\ -\pi - \arctan\left(\sqrt{2}\right) + 2\pi c_1, & c_1 \in \mathbb{Z}. \end{cases} \tag{5.45}$$

Looking at angles greater than zero, the first two angles, that increases the symmetry of the molecule, is $\theta = \arctan\left(\sqrt{2}\right)$ and $\theta = \pi - \arctan\left(\sqrt{2}\right)$. In **Fig. 5.4** these angles are marked with red lines. The shape of the molecule in this highly symmetrical case is illustrated in **Fig. 5.5**.

The five lowest eigenenergies of the full Hamiltonian of 1T-VS_6, see Eq. (5.3), is found for $\theta = \arctan(\sqrt{2})$ and is depicted in **Fig. 5.6**. To obtain this spectrum the coordinate system illustrated in **Fig. 5.5** (b) is used.

Comparing this spectrum to **Fig. 5.3**, it is evident that the spectrum has changed. Again, the included d-orbitals in the eigenvectors are viewed in the figure and in this case each eigenvector is only made up of a single d-orbital. Since the symmetry of 1T-VS_6 is increased at this angle, the number of symmetry elements also increases. 1T-VS_6 for $\theta = \arctan(\sqrt{2})$ is illustrated in a rotated view in **Fig. 5.5** (b) and it is clear to see that the symmetry has changed.

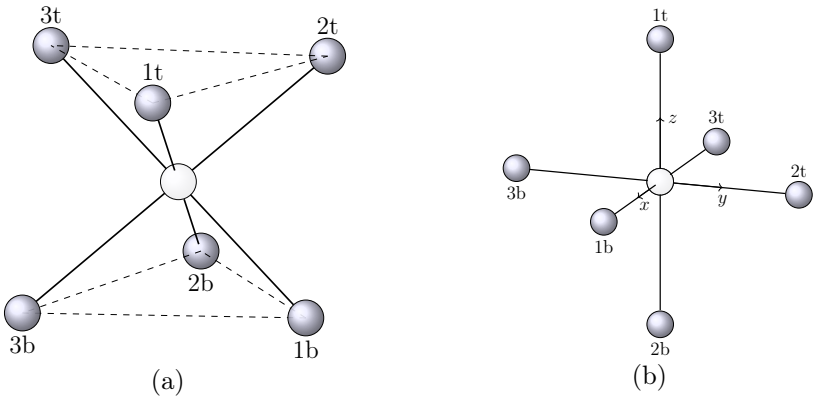

Fig. 5.5: 1T octahedral structure with $\theta = \arctan(\sqrt{2})$, in the same direction view as in **Fig. 5.1** (a) and in a rotated direction view (b) that emphasizes the higher symmetry.

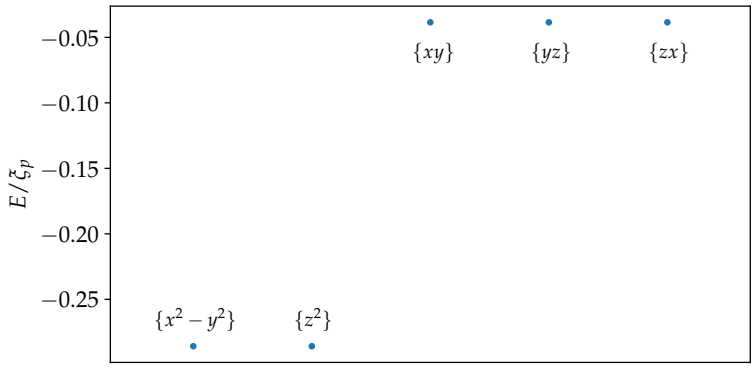

Fig. 5.6: Illustration of the five eigenenergy levels E obained numerically with $\xi_d = 0$, $\xi_p = 1$, $\frac{V_{pd\sigma}}{\xi_p} = 0.35$, $\frac{V_{pd\pi}}{\xi_p} = 0.1$ and $\theta = \arctan(\sqrt{2})$ for 1T-VS_6.

The symmetry of the molecule is now described by the $\mathbf{O_h}$ point group with the total number of 48 elements. The character table of this group is depicted in **Table 5.2**. E and i is the unit transformation and inversion, respectively. C_3 are rotations of $2\pi/3$ around axes located at the center of three sulfur atoms. C_2 denotes rotations of π around the axis $\frac{1}{\sqrt{2}}(x+y)$, see **Fig. 5.5** (b), or similar rotations. C_4 and C_2' are rotations of $\pi/2$ and π around the x-, y- and z-axis, respectively. σ_h represent the three reflections in the xy-, yz- and zx-plane. σ_d are reflections in planes spanned by e.g. the z-axis and the $\frac{1}{\sqrt{2}}(x+y)$. Lastly, $S_4 = C_4 \oplus \sigma_h$ and $S_6 = c_6 \oplus \sigma_h$.

$\mathbf{O_h}$	E	$8C_3$	$6C_2$	$6C_4$	$3C_2' = C_4^2$	i	$6S_4$	$8S_6$	$3\sigma_h$	$6\sigma_d$	Quadratic Functions
A_{1g}	1	1	1	1	1	1	1	1	1	1	$(x^2+y^2+z^2)$
A_{2g}	1	1	-1	-1	1	1	-1	1	1	-1	–
E_g	2	-1	0	0	2	2	0	-1	2	0	$(2z^2-x^2-y^2, x^2-y^2)$
T_{1g}	3	0	-1	1	-1	3	1	0	-1	-1	–
T_{2g}	3	0	1	-1	-1	3	-1	0	-1	1	(zx, yz, xy)
A_{1u}	1	1	1	1	1	-1	-1	-1	-1	-1	–
A_{2u}	1	1	-1	-1	1	-1	1	-1	-1	1	–
E_u	2	-1	0	0	2	-2	0	1	-2	0	–
T_{1u}	3	0	-1	1	-1	-3	-1	0	1	1	–
T_{2u}	3	0	1	-1	-1	-3	1	0	1	-1	–

Table 5.2: Character table of the $\mathbf{O_h}$ point group [31].

In this table we see that xy, yz and zx belongs to the same representation, i.e., the T_{2g} representation, and that z^2 and x^2-y^2 belongs to the same representation, E_g. This explains the degeneracy observed in the spectrum in this high symmetrical case.

5.2.2 2H Structure

The 2H phase of VS_6 will now be investigated using a similar approach as for the 1T phase. Here the atoms in the lower sublayer are rotated by 60° compared to the 1T phase, see **Fig. 5.1** (a). This results in the five lowest eigenenergies depicted in **Fig. 5.7**. At first sight, this looks very similar to the spectrum for the 1T phase with two two-fold degenerate energy levels and one non-degenerate. The difference between the two cases appear from the eigenstates. As for the 1T phase, the eigenstate belonging to the energy level with no degeneracy is solely made up of the z^2 d-orbital. The eigenfunctions for the two higher energies are both superpositions of the xy d-orbital and the x^2-y^2 d-orbital whereas the eigenfunctions for the two lower energies are superpositions of the yz and the zx d-orbitals. The reason for this will be investigated using group theory in the following subsection.

Comparing the two lowest energies in **Fig. 5.7** with the two lowest energies in **Fig. 5.3**, it is evident that the lowest energies in the 1T phase is slightly lower than the lowest energies in the 2H phase. This indicates that the 1T phase of monolayer VS_2 is more stable than the 2H phase. This does not agree with DFT calculations [2]. This could be explained by the choice of θ in these calculations. Later, when investigating monolayer VS_2, the relaxed structure is collected from C2DB [3]. These lattice parameters yield an energyspectrum where the lowest energy level is the z^2 level, and in that case the 2H phase is more stable compared to the 1T phase in agreement with DFT calculations.

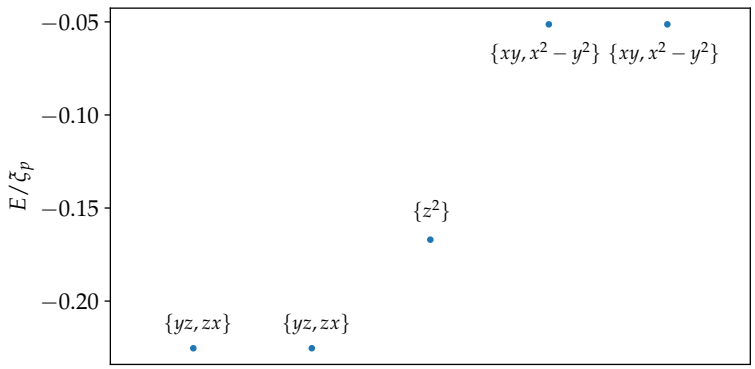

Fig. 5.7: Illustration of the five lowest eigenenergy levels E obtained numerically with $\xi_d = 0$, $\xi_p = 1$, $\frac{V_{pd\sigma}}{\xi_p} = 0.35$, $\frac{V_{pd\pi}}{\xi_p} = 0.1$ and $\theta = 37°$ for the 2H phase.

$V_{pd}^\dagger V_{pd}$ for the 2H phase can now be obtained analytically. In the basis $\{xy, yz, zx, x^2 - y^2, z^2\}$ in terms of θ, $V_{pd\pi}$ and $V_{pd\sigma}$ this is

$$V_{pd}^\dagger V_{pd} = \begin{bmatrix} M_{1,1} & 0 & 0 & 0 & 0 \\ 0 & M_{2,2} & 0 & 0 & 0 \\ 0 & 0 & M_{2,2} & 0 & 0 \\ 0 & 0 & 0 & M_{1,1} & 0 \\ 0 & 0 & 0 & 0 & M_{5,5} \end{bmatrix}, \tag{5.46}$$

where

$$M_{1,1} = \frac{3}{8}\sin^2\theta\left[12V_{pd\pi}^2(1+\cos 2\theta) + V_{pd\sigma}^2(1-3\cos 2\theta)\right], \tag{5.47}$$

$$M_{2,2} = \frac{3}{8}\left[2V_{pd\pi}^2(2+\cos 2\theta+\cos 4\theta + 3V_{pd\sigma}^2(1-\cos 4\theta)\right], \tag{5.48}$$

$$M_{5,5} = \frac{9}{4}\left[V_{pd\pi}^2(1-\cos 4\theta) + V_{pd\sigma}^2\left(\frac{11}{12}+\cos 2\theta+\frac{3}{4}\cos 4\theta\right)\right]. \tag{5.49}$$

It is evident that this matrix is diagonal and that only three unique values enter in this diagonal. This will be explained in the following subsection.

Symmetry of the 2H phase

The symmetry of 2H-VS_6 will now be investigated. The 2H phase belongs to the $\mathbf{D_{3h}}$ point group with the same number of symmetry elements as $\mathbf{D_{3d}}$, i.e., twelve elements. The character table of this group is depicted in **Table 5.3**. A part of the elements of the $\mathbf{D_{3d}}$ point group recur in $\mathbf{D_{3h}}$, namely E and the two C_3 rotations. Additionally, 2H-VS_6 is symmetric under a rotation of π about a vector with x- and y-components of a vector pointing from the origin towards either of the three atoms in the top sublayer but with a zero z-component.

This gives the three $C_2^{'}$ elements, one for each atom in the top sublayer. Contrary to the 1T phase, the 2H phase is symmetric under reflection in the xy-plane and this element is denoted $\sigma_h(xy)$. Further, 2H-VS_6 is invariant under a rotation of $\pm 2\pi/3$ around the z-axis followed by a reflection in the xy-plane. These transformations are denoted S_3. Lastly, the molecule is invariant under reflections in the planes spanned by the coupling lines perpendicular to the xy-plane. This is the three σ_v elements which corresponds to the three σ_d elements in $\mathbf{D_{3d}}$.

$\mathbf{D_{3h}}$	E	$2C_3(z)$	$3C_2'$	$\sigma_h(xy)$	$2S_3$	$3\sigma_v$	Quadratic Functions
$A_1^{'}$	1	1	1	1	1	1	(x^2+y^2, z^2)
$A_2^{'}$	1	1	-1	1	1	-1	–
$E^{'}$	2	-1	0	2	-1	0	(x^2-y^2, xy)
$A_1^{''}$	1	1	1	-1	-1	-1	–
$A_2^{''}$	1	1	-1	-1	-1	1	–
$E^{''}$	2	-1	0	-2	1	0	(zx, yz)

Table 5.3: Character table of the $\mathbf{D_{3h}}$ point group [32].

In the character table for $\mathbf{D_{3h}}$, it is evident that xy and x^2-y^2 belong to a different representation than yz and zx in contrast to the former case. As for the 1T phase, z^2 belongs to its own representation. The two-dimensional irreducible representations of all elements in $\mathbf{D_{3h}}$ according to the $E^{''}$ representation in the basis $\{yz, zx\}$ can now be formulated, following the same procedure as in **section 5.2.1**,

$$\Gamma(E) = \begin{bmatrix} 1 & 0 \\ 0 & 1 \end{bmatrix}, \quad \Gamma(C_3) = \begin{bmatrix} -\frac{1}{2} & -\frac{\sqrt{3}}{2} \\ \frac{\sqrt{3}}{2} & -\frac{1}{2} \end{bmatrix}, \quad \Gamma(C_3^2) = \begin{bmatrix} -\frac{1}{2} & \frac{\sqrt{3}}{2} \\ -\frac{\sqrt{3}}{2} & -\frac{1}{2} \end{bmatrix},$$

$$\Gamma(C_2'(1a)) = \begin{bmatrix} 1 & 0 \\ 0 & -1 \end{bmatrix}, \quad \Gamma(C_2'(2a)) = \begin{bmatrix} -\frac{1}{2} & \frac{\sqrt{3}}{2} \\ \frac{\sqrt{3}}{2} & \frac{1}{2} \end{bmatrix}, \quad \Gamma(C_2'(3a)) = \begin{bmatrix} -\frac{1}{2} & -\frac{\sqrt{3}}{2} \\ -\frac{\sqrt{3}}{2} & \frac{1}{2} \end{bmatrix},$$

$$\Gamma(\sigma_h) = \begin{bmatrix} -1 & 0 \\ 0 & -1 \end{bmatrix}, \quad \Gamma(S_3) = \begin{bmatrix} \frac{1}{2} & \frac{\sqrt{3}}{2} \\ -\frac{\sqrt{3}}{2} & \frac{1}{2} \end{bmatrix}, \quad \Gamma(-S_3) = \begin{bmatrix} \frac{1}{2} & -\frac{\sqrt{3}}{2} \\ \frac{\sqrt{3}}{2} & \frac{1}{2} \end{bmatrix},$$

$$\Gamma(\sigma_v(1a)) = \begin{bmatrix} -1 & 0 \\ 0 & 1 \end{bmatrix}, \quad \Gamma(\sigma_v(2a)) = \begin{bmatrix} \frac{1}{2} & -\frac{\sqrt{3}}{2} \\ -\frac{\sqrt{3}}{2} & -\frac{1}{2} \end{bmatrix}, \quad \Gamma(\sigma_v(3a)) = \begin{bmatrix} \frac{1}{2} & \frac{\sqrt{3}}{2} \\ \frac{\sqrt{3}}{2} & -\frac{1}{2} \end{bmatrix}.$$

Again, note that the characters of these irreducible representations are equal to the characters stated in **Table 5.3**. Using the projection operator, see Eq. (2.22), in terms of these irreducible representations, we can show that yz belongs to the first row and zx belongs to the second row, i.e.,

$$\hat{\mathscr{P}}_{11} yz = yz, \quad \hat{\mathscr{P}}_{22} yz = 0, \quad \hat{\mathscr{P}}_{22} zx = zx, \quad \hat{\mathscr{P}}_{11} zx = 0. \tag{5.50}$$

Likewise, a two-dimensional irreducible representation can be formulated for the elements of the E' representation in the basis $\{xy, x^2-y^2\}$, where it can be shown that xy

belongs to the first row and $x^2 - y^2$ belongs to the second row. The diagonal element $\langle yz|\hat{\mathcal{H}}|yz\rangle$ can now be written as

$$\begin{aligned}\langle yz|\hat{\mathcal{H}}|yz\rangle &= \langle yz|\hat{U}^\dagger(S_3)\hat{U}(S_3)\hat{\mathcal{H}}\hat{U}^\dagger(S_3)\hat{U}(S_3)|yz\rangle = \langle yz|\hat{U}^\dagger(S_3)\hat{\mathcal{H}}\hat{U}(S_3)|yz\rangle \\ &= \left(\frac{1}{2}\langle yz| - \frac{\sqrt{3}}{2}\langle zx|\right)\hat{\mathcal{H}}\left(\frac{1}{2}|yz\rangle - \frac{\sqrt{3}}{2}|zx\rangle\right) \\ &= \frac{1}{4}\langle yz|\hat{\mathcal{H}}|yz\rangle + \frac{3}{4}\langle zx|\hat{\mathcal{H}}|zx\rangle. \end{aligned} \tag{5.51}$$

The cross terms proportional to $\langle yz|\hat{\mathcal{H}}|zx\rangle$ and $\langle zx|\hat{\mathcal{H}}|yz\rangle$ are zero as a result of the fact that yz and zx belong to two different rows of the E'' representation. For the equality sign in Eq. (5.51) to be obeyed, it requires that

$$\langle yz|\hat{\mathcal{H}}|yz\rangle = \langle zx|\hat{\mathcal{H}}|zx\rangle. \tag{5.52}$$

This result is independent of the choice of symmetry operator. Using the same procedure it can be shown that all off-diagonal elements are zero and that $\langle xy|\hat{\mathcal{H}}|xy\rangle = \langle x^2 - y^2|\hat{\mathcal{H}}|x^2 - y^2\rangle$, in agreement with Eq. (5.46).

The spectrum of 2H-VS_6 thus looks very similar to the spectrum obtained in the 1T phase, see **Fig. 5.7** and **Fig. 5.3**, though the degeneracy here has nothing to do with the direct coupling between the d-orbitals; rather, that the shift in the energies, due to the presence of the p-orbitals, leads to a similar degeneracy.

5.3 Tight Binding Model of Monolayer VS_2

In this section the band structure of monolayer VS_2 for both the 2H and 1T phase will be obtained using the tight binding method. This is done with inspiration from Ridolfi et al. [33]. Further, the Coulomb interaction will be included using the Hubbard model. The results will then be compared to DFT results of the same structures taken from C2DB [3]. The relaxed structures of the two phases of VS_2 have been collected from this database, such that the band structure obtained in the following is based on exactly the same structure as for the band structure obtained with DFT.

5.3.1 2H Structure

In **Fig. 5.8** a top view of the structure of monolayer 2H-VS_2 is illustrated together with the two lattice vectors $\mathbf{a}_1$ and $\mathbf{a}_2$. Seen from above the structure is strikingly similar to graphene though VS_2, in contrary to graphene, also extends spatially along the S-V-S direction, see **Fig. 5.1** (b). One unit cell contains one vanadium atom and two sulfur atoms, one in the top (t) sublayer and one in the bottom (b) sublayer. We will thus be working in this three-atom basis. The unit cell is marked with dashed lines. Note that since the x and y coordinates of the two sulfur atoms coincide, both are not evident in **Fig. 5.8**.

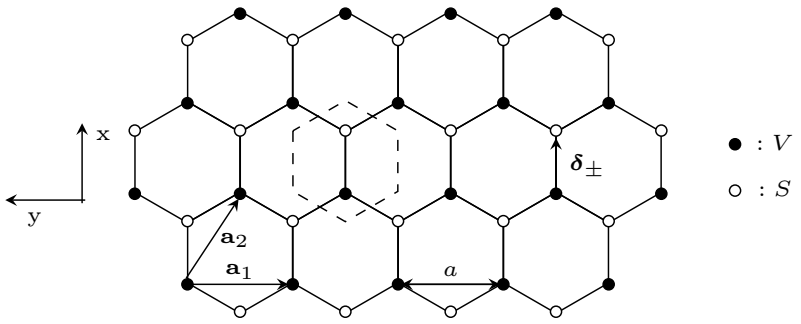

Fig. 5.8: Top view of monolayer 2H-VS_2 in real space. The black dots illustrates the vanadium atoms whereas the white dots illustrates the sulfur atoms. The unit cell is shown with dashed lines and the lattice vectors $\mathbf{a}_1$ and $\mathbf{a}_2$ are indicated. Further, the two vectors $\boldsymbol{\delta}_\pm$ that connect the vanadium atom with the two sulfur atoms in one unit cell, is shown. Lastly, the used coordinate system is illustrated.

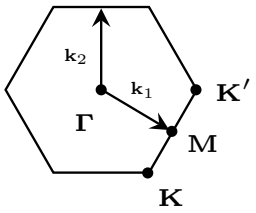

Fig. 5.9: Brillouin zone for the 2H phase of monolayer VS_2. $\mathbf{k}_1$ and $\mathbf{k}_2$ are the reciprocal lattice vectors and $\mathbf{\Gamma}$, $\mathbf{K}$, $\mathbf{K}'$ and $\mathbf{M}$ are the high-symmetrical points.

Using the same coordinate system as depicted in **Fig. 5.8**, the two lattice vectors can be written as

$$\mathbf{a}_1 = (0, -a, 0) \quad , \quad \mathbf{a}_2 = \left(\frac{\sqrt{3}}{2} a, -\frac{a}{2}, 0 \right). \tag{5.53}$$

The distance a is found from DFT [3] to be $a = 3.186$ Å. The brillouin zone in reciprocal space also forms a hexagon, see **Fig. 5.9**. The reciprocal lattice vectors is found from $\mathbf{a}_1$ and $\mathbf{a}_2$ to be

$$\mathbf{k}_1 = \frac{-2\pi}{\sqrt{3}a} \left(1, \sqrt{3}, 0 \right) \quad , \quad \mathbf{k}_2 = \frac{4\pi}{\sqrt{3}a} \left(1, 0, 0 \right). \tag{5.54}$$

The high-symmetrical points in $\mathbf{k}$-space illustrated in **Fig. 5.9** are given by

$$\begin{aligned} \mathbf{\Gamma} = (0,0,0), \quad \mathbf{M} &= \left(\frac{-\pi}{\sqrt{3}a}, \frac{-\pi}{a}, 0 \right), \\ \mathbf{K}' = \left(0, -\sqrt{\frac{16}{9}} \frac{\pi}{a}, 0 \right), \quad \mathbf{K} &= \left(\frac{-2\pi}{\sqrt{3}a}, \frac{-2\pi}{3a}, 0 \right). \end{aligned} \tag{5.55}$$

Let $\mathbf{r}_i$ denote the location of the vanadium atom in unit cell i. Since there is five d-orbitals on the vanadium atom, we define the states

$$\begin{aligned} |\mathbf{r}_i; d_1\rangle = |d_{xy}\rangle, \quad |\mathbf{r}_i; d_2\rangle = |d_{yz}\rangle, \quad |\mathbf{r}_i; d_3\rangle = |d_{zx}\rangle, \\ |\mathbf{r}_i; d_4\rangle = |d_{x^2-y^2}\rangle, \quad |\mathbf{r}_i; d_5\rangle = |d_{z^2}\rangle. \end{aligned} \tag{5.56}$$

Each sulfur atom in the unit cell have three p-orbitals, so we define the states

$$|\mathbf{r}_i + \boldsymbol{\delta}_\pm; p_1\rangle = |p_x^{t/b}\rangle, \quad |\mathbf{r}_i + \boldsymbol{\delta}_\pm; p_2\rangle = |p_y^{t/b}\rangle, \quad |\mathbf{r}_i + \boldsymbol{\delta}_\pm; p_3\rangle = |p_z^{t/b}\rangle, \tag{5.57}$$

where δ_+ and δ_- are the vectors pointing from the vanadium atom to the sulfur atoms in the top and bottom sublayers, respectively, see **Fig. 5.8**.

Using this basis the Hamiltonian can be written as

$$\begin{aligned}\hat{\mathcal{H}} = &\sum_{\mathbf{r}_i,\mu} \xi^d_\mu \hat{d}^\dagger_{i,\mu}\hat{d}_{i,\mu} + \sum_{\mathbf{r}_i,\nu} \xi^p_\nu \left[\left(\hat{p}^t_{i,\nu}\right)^\dagger \hat{p}^t_{i,\nu} + \left(\hat{p}^b_{i,\nu}\right)^\dagger \hat{p}^b_{i,\nu} \right] \\ &+ \sum_{\mathbf{r}_i} \sum_{\mu\nu} \left[t^t_{\mu\nu} \hat{d}^\dagger_{i,\mu}\hat{p}^t_{i,\nu} + t^b_{\mu\nu}\hat{d}^\dagger_{i,\mu}\hat{p}^b_{i,\nu} + h.c. \right] \\ &+ \sum_{\mathbf{r}_i} \sum_{\mathbf{r}_j=\mathbf{r}_i+\mathbf{a}_1-\mathbf{a}_2} \sum_{\mu\nu} \left[t^{r,t}_{\mu\nu} \hat{d}^\dagger_{i,\mu}\hat{p}^t_{j,\nu} + t^{r,b}_{\mu\nu}\hat{d}^\dagger_{i,\mu}\hat{p}^b_{j,\nu} + h.c. \right] \\ &+ \sum_{\mathbf{r}_i} \sum_{\mathbf{r}_j=\mathbf{r}_i-\mathbf{a}_2} \sum_{\mu\nu} \left[t^{l,t}_{\mu\nu} \hat{d}^\dagger_{i,\mu}\hat{p}^t_{j,\nu} + t^{l,b}_{\mu\nu}\hat{d}^\dagger_{i,\mu}\hat{p}^b_{j,\nu} + h.c. \right].\end{aligned} \tag{5.58}$$

The operator $\hat{d}^\dagger_{i,\mu}$ ($\hat{d}_{i,\mu}$) creates (annihilates) an electron in orbital μ on the vanadium atom at $\mathbf{r}_i$ in unit cell i. Similarly, the operators $(\hat{p}^{t,b}_{j,\nu})^\dagger$ and $\hat{p}^{t,b}_{j,\nu}$ creates and annihilates an electron on the sulfur atom at site $\mathbf{r}_i + \boldsymbol{\delta}_\pm$ in orbital ν in the top or bottom sublayer, respectively. The three first terms of the Hamiltonian state the onsite energies of the d- and p-orbitals of the three atoms in the unit cell. Further, the Hamiltonian consists of six terms where an electron can hop from a p-orbital to any nearest neighbor d-orbital. The Hermitian conjugate of these terms includes hopping from a d-orbital to any nearest neighbour p-orbital. For simplicity the spin indices are omitted for now. The following onsite energies and hopping amplitudes have been defined as

$$\xi^d_\mu = \langle \mathbf{r}_i; d_\mu | \hat{\mathcal{H}}_t | \mathbf{r}_i; d_\mu \rangle, \tag{5.59}$$
$$\xi^p_\nu = \langle \mathbf{r}_i + \boldsymbol{\delta}_\pm; p_\nu | \hat{\mathcal{H}}_t | \mathbf{r}_i + \boldsymbol{\delta}_\pm; p_\nu \rangle, \tag{5.60}$$
$$t^t_{\mu\nu} = \langle \mathbf{r}_i; d_\mu | \hat{\mathcal{H}}_t | \mathbf{r}_i + \boldsymbol{\delta}_+; p_\nu \rangle, \tag{5.61}$$
$$t^b_{\mu\nu} = \langle \mathbf{r}_i; d_\mu | \hat{\mathcal{H}}_t | \mathbf{r}_i + \boldsymbol{\delta}_-; p_\nu \rangle, \tag{5.62}$$
$$t^{r,t}_{\mu\nu} = \langle \mathbf{r}_i; d_\mu | \hat{\mathcal{H}}_t | \mathbf{r}_i + \boldsymbol{\delta}_+ + \mathbf{a}_1 - \mathbf{a}_2; p_\nu \rangle, \tag{5.63}$$
$$t^{r,b}_{\mu\nu} = \langle \mathbf{r}_i; d_\mu | \hat{\mathcal{H}}_t | \mathbf{r}_i + \boldsymbol{\delta}_- + \mathbf{a}_1 - \mathbf{a}_2; p_\nu \rangle, \tag{5.64}$$
$$t^{l,t}_{\mu\nu} = \langle \mathbf{r}_i; d_\mu | \hat{\mathcal{H}}_t | \mathbf{r}_i + \boldsymbol{\delta}_+ - \mathbf{a}_2; p_\nu \rangle, \tag{5.65}$$
$$t^{l,b}_{\mu\nu} = \langle \mathbf{r}_i; d_\mu | \hat{\mathcal{H}}_t | \mathbf{r}_i + \boldsymbol{\delta}_- - \mathbf{a}_2; p_\nu \rangle, \tag{5.66}$$

where $\hat{\mathcal{H}}_t$ is the tight binding Hamiltonian, see Eq. (5.1). The numerical values for these can be obtained using the Slater Koster decomposition introduced in **section 5.2**. As previously we assume that the onsite energies for the d-orbitals are degenerate, i.e., $\xi^d_\mu = \xi_d$ for all μ. Similarly, for the p-orbitals $\xi^p_\nu = \xi_p$ for all ν.

In the Slater Koster decomposition the hopping matrices simplifies to

$$
\begin{aligned}
t^t &= \begin{bmatrix} 0 & t^t_{12} & 0 \\ 0 & t^t_{22} & 0 \\ t^t_{31} & 0 & t^t_{33} \\ t^t_{41} & 0 & t^t_{43} \\ t^t_{51} & 0 & t^t_{53} \end{bmatrix} \quad , \quad t^b = \begin{bmatrix} 0 & t^t_{12} & 0 \\ 0 & -t^t_{22} & 0 \\ -t^t_{31} & 0 & t^t_{33} \\ t^t_{41} & 0 & -t^t_{43} \\ t^t_{51} & 0 & -t^t_{53} \end{bmatrix}, \\
t^{l,t} &= \begin{bmatrix} t^{l,t}_{11} & t^{l,t}_{12} & t^{l,t}_{13} \\ t^{l,t}_{21} & t^{l,t}_{22} & t^{l,t}_{23} \\ t^{l,t}_{31} & t^{l,t}_{32} & t^{l,t}_{33} \\ t^{l,t}_{41} & t^{l,t}_{42} & t^{l,t}_{43} \\ t^{l,t}_{51} & t^{l,t}_{52} & t^{l,t}_{53} \end{bmatrix} \quad , \quad t^{l,b} = \begin{bmatrix} t^{l,t}_{11} & t^{l,t}_{12} & -t^{l,t}_{13} \\ -t^{l,t}_{21} & -t^{l,t}_{22} & t^{l,t}_{23} \\ -t^{l,t}_{31} & -t^{l,t}_{32} & t^{l,t}_{33} \\ t^{l,t}_{41} & t^{l,t}_{42} & -t^{l,t}_{43} \\ t^{l,t}_{51} & t^{l,t}_{52} & -t^{l,t}_{53} \end{bmatrix}, \\
t^{r,t} &= \begin{bmatrix} -t^{l,t}_{11} & t^{l,t}_{12} & -t^{l,t}_{13} \\ -t^{l,t}_{21} & t^{l,t}_{22} & -t^{l,t}_{23} \\ t^{l,t}_{31} & -t^{l,t}_{32} & t^{l,t}_{33} \\ t^{l,t}_{41} & -t^{l,t}_{42} & t^{l,t}_{43} \\ t^{l,t}_{51} & -t^{l,t}_{52} & t^{l,t}_{53} \end{bmatrix} \quad , \quad t^{r,b} = \begin{bmatrix} -t^{l,t}_{11} & t^{l,t}_{12} & t^{l,t}_{13} \\ t^{l,t}_{21} & -t^{l,t}_{22} & -t^{l,t}_{23} \\ -t^{l,t}_{31} & t^{l,t}_{32} & t^{l,t}_{33} \\ t^{l,t}_{41} & -t^{l,t}_{42} & -t^{l,t}_{43} \\ t^{l,t}_{51} & -t^{l,t}_{52} & -t^{l,t}_{53} \end{bmatrix}.
\end{aligned}
\tag{5.67}
$$

The Hamiltonian is Fourier transformed, using

$$
\hat{d}^\dagger_{i,\mu} = \frac{1}{\sqrt{N}} \sum_{\mathbf{k}} e^{-i\mathbf{k}\cdot\mathbf{r}} \hat{d}^\dagger_{\mathbf{k},\mu} \quad \text{and} \quad \hat{d}_{i,\mu} = \frac{1}{\sqrt{N}} \sum_{\mathbf{k}} e^{i\mathbf{k}\cdot\mathbf{r}} \hat{d}_{\mathbf{k},\mu},
\tag{5.68}
$$

which results in the expression

$$
\begin{aligned}
\hat{\mathcal{H}} = \sum_{\mathbf{k}} \Bigg[& \xi_d \sum_{\mu} \hat{d}^\dagger_{\mathbf{k},\mu} \hat{d}_{\mathbf{k},\mu} + \xi_p \sum_{\nu} \left[(\hat{p}^t_{\mathbf{k},\nu})^\dagger \hat{p}^t_{\mathbf{k},\nu} + (\hat{p}^b_{\mathbf{k},\nu})^\dagger \hat{p}^b_{\mathbf{k},\nu} \right] \\
& + \sum_{\mu\nu} \Bigg\{ e^{i\mathbf{k}\cdot\boldsymbol{\delta}_+} t^t_{\mu\nu} \hat{d}^\dagger_{\mathbf{k},\mu} \hat{p}^t_{\mathbf{k},\nu} + e^{i\mathbf{k}\cdot\boldsymbol{\delta}_-} t^b_{\mu\nu} \hat{d}^\dagger_{\mathbf{k},\mu} \hat{p}^b_{\mathbf{k},\nu} + h.c. \\
& + e^{i\mathbf{k}\cdot(\boldsymbol{\delta}_+ + \mathbf{a1} - \mathbf{a2})} \left(t^{r,t}_{\mu\nu} \hat{d}^\dagger_{\mathbf{k},\mu} \hat{p}^t_{\mathbf{k},\nu} + t^{r,b}_{\mu\nu} \hat{d}^\dagger_{\mathbf{k},\mu} \hat{p}^b_{\mathbf{k},\nu} + h.c. \right) \\
& + e^{i\mathbf{k}\cdot(\boldsymbol{\delta} - \mathbf{a}_2)} \left(t^{l,t}_{\mu\nu} \hat{d}^\dagger_{\mathbf{k},\mu} \hat{p}^t_{\mathbf{k},\nu} + t^{l,b}_{\mu\nu} \hat{d}^\dagger_{\mathbf{k},\mu} \hat{p}^b_{\mathbf{k},\nu} + h.c. \right) \Bigg\} \Bigg].
\end{aligned}
\tag{5.69}
$$

Defining

$$
T^t = \delta_1 (t^t_{\mu\nu} + z_1 z_2^* t^{r,t}_{\mu\nu} + z_2^* t^{l,t}_{\mu\nu}),
\tag{5.70}
$$

$$
T^b = \delta_2 (t^b_{\mu\nu} + z_1 z_2^* t^{r,b}_{\mu\nu} + z_2^* t^{l,b}_{\mu\nu}),
\tag{5.71}
$$

with

$$
\begin{aligned}
\delta_1 = e^{i\mathbf{k}\cdot\delta_+}, \quad \delta_2 = e^{i\mathbf{k}\cdot\delta_-}, \\
z_1 = e^{i\mathbf{k}\cdot\mathbf{a}_1} = e^{-ik_y a}, \quad z_2 = e^{i\mathbf{k}\cdot\mathbf{a}_2} = e^{-ik_y a/2} e^{i\sqrt{3}k_x a/2},
\end{aligned}
\tag{5.72}
$$

the Hamiltonian can be written in the simple form

$$\begin{aligned}\hat{\mathcal{H}} = \sum_{\mathbf{k}} \Bigg[&\xi_d \sum_{\mu} \hat{d}^{\dagger}_{\mathbf{k},\mu} \hat{d}_{\mathbf{k},\mu} + \xi_p \sum_{\nu} \left[(\hat{p}^t_{\mathbf{k},\nu})^{\dagger} \hat{p}^t_{\mathbf{k},\nu} + (\hat{p}^b_{\mathbf{k},\nu})^{\dagger} \hat{p}^b_{\mathbf{k},\nu} \right] \\ &+ \sum_{\mu\nu} \left\{ T^t \hat{d}^{\dagger}_{\mathbf{k},\mu} \hat{p}^t_{\mathbf{k},\nu} + (T^t)^{\dagger} (\hat{p}^t_{\mathbf{k},\nu})^{\dagger} \hat{d}_{\mathbf{k},\mu} + T^b \hat{d}^{\dagger}_{\mathbf{k},\mu} \hat{p}^b_{\mathbf{k},\nu} + (T^b)^{\dagger} (\hat{p}^b_{\mathbf{k},\nu})^{\dagger} \hat{d}_{\mathbf{k},\mu} \right\} \Bigg].\end{aligned} \tag{5.73}$$

Both $\delta_1 \simeq 1$ and $\delta_2 \simeq 1$, so these are set to one. Projecting the vector $\hat{\mathcal{H}}|\mathbf{k}\rangle$ onto the three-atom basis, we can write

$$\begin{bmatrix} \mathcal{H}^d & T^t & T^b \\ (T^t)^{\dagger} & \mathcal{H}^p & 0 \\ (T^b)^{\dagger} & 0 & \mathcal{H}^p \end{bmatrix} \begin{bmatrix} \alpha \\ \tau \\ \beta \end{bmatrix} = E \begin{bmatrix} \alpha \\ \tau \\ \beta \end{bmatrix}. \tag{5.74}$$

Here $\mathcal{H}^d$ is a 5x5 diagonal matrix with ξ_d on the diagonal, and $\mathcal{H}^p$ is a 3x3 diagonal matrix with ξ_p on the diagonal. α represents the d-orbitals on the vanadium site and τ and β represent the top and bottom p-orbitals, respectively, on the sulfur sites in the unit cell. This expression is sufficiently simple to diagonalize the Hamiltonian numerically. As in **section 5.2.1** the five energy bands of the d-orbitals can be obtained. This can either be done by diagonalizing the full Hamiltonian or from the matrix $(T^t, T^b)(T^t, T^b)^{\dagger}$. The Hamiltonian is solved as a function of $\mathbf{k}$, where we investigate the path $\mathbf{k} = \mathbf{\Gamma} \to \mathbf{M} \to \mathbf{K} \to \mathbf{\Gamma}$. In the previous sections we have set the onsite energy of the p-orbitals to be greater than the onsite energy of the d-orbitals. From DFT calculations of the energy bands [3], it is determined that $\xi_p < \xi_d$. This does not affect any of the results and conclusions from previous sections, though we will set $\xi_p < \xi_d$ in the following.

To be able to investigate the full problem analytically, further simplifications must be introduced. The basis, written in terms of the amplitudes of the eigenvector, can be written as

$$\psi^T = (\alpha_1, \alpha_2, \alpha_3, \alpha_4, \alpha_5, \tau_1, \tau_2, \tau_3, \beta_1, \beta_2, \beta_3). \tag{5.75}$$

The α's are thus the amplitudes corresponding to the d-orbitals in the order given in Eq. (5.56), the τ's and the β's correspond to p-orbitals in the top and bottom sublayer, respecitvely, in the order presented in Eq. (5.57). To be able to diagonalize the Hamiltonian, we introduce the symmetric and antisymmetric components

$$\boldsymbol{\theta}_{\mathbf{k}\nu} = \frac{1}{\sqrt{2}}(\boldsymbol{\tau}_{\mathbf{k}\nu} + \boldsymbol{\beta}_{\mathbf{k}\nu}) \quad \text{and} \quad \boldsymbol{\phi}_{\mathbf{k}\nu} = \frac{1}{\sqrt{2}}(\boldsymbol{\tau}_{\mathbf{k}\nu} - \boldsymbol{\beta}_{\mathbf{k}\nu}). \tag{5.76}$$

Further, the new hopping matrices

$$T^E = \frac{1}{\sqrt{2}}(T^t + T^b) \quad \text{and} \quad T^O = \frac{1}{\sqrt{2}}(T^t - T^b), \tag{5.77}$$

are defined, such that the eigenproblem can be written as

$$\begin{bmatrix} \mathcal{H}^d & T^E & T^O \\ (T^E)^\dagger & \mathcal{H}^p & 0 \\ (T^O)^\dagger & 0 & \mathcal{H}^p \end{bmatrix} \begin{bmatrix} \alpha \\ \theta \\ \phi \end{bmatrix} = E \begin{bmatrix} \alpha \\ \tau \\ \beta \end{bmatrix}. \tag{5.78}$$

We can now rearrange the amplitudes of the eigenvector collecting all even components and all odd components, leading to the basis

$$\tilde{\psi}^T = (\alpha_5, \alpha_4, \alpha_1, \theta_1, \theta_2, \phi_3, \alpha_3, \alpha_2, \phi_1, \phi_2, \theta_3). \tag{5.79}$$

The eigenproblem can now be written in the decoupled form

$$\begin{bmatrix} \mathcal{H}^E & 0 \\ 0 & \mathcal{H}^O \end{bmatrix} \tilde{\psi} = E\tilde{\psi}, \tag{5.80}$$

where we have defined the even Hamiltonian

$$\mathcal{H}^E = \begin{bmatrix} \mathcal{H}^{d,E} & T^{E,O} \\ (T^{E,O})^\dagger & \mathcal{H}^{p,E} \end{bmatrix} \quad \text{with} \quad T^{E,O} = \begin{bmatrix} T^E_{51} & T^E_{52} & T^O_{53} \\ T^E_{41} & T^E_{42} & T^O_{43} \\ T^E_{11} & T^E_{12} & T^O_{13} \end{bmatrix}, \tag{5.81}$$

and the odd Hamiltonian given by

$$\mathcal{H}^O = \begin{bmatrix} \mathcal{H}^{d,O} & T^{O,E} \\ (T^{O,E})^\dagger & \mathcal{H}^{p,O} \end{bmatrix} \quad \text{with} \quad T^{O,E} = \begin{bmatrix} T^O_{31} & T^O_{32} & T^E_{33} \\ T^O_{21} & T^O_{22} & T^E_{23} \end{bmatrix}. \tag{5.82}$$

$\mathcal{H}^{d,E}$, $\mathcal{H}^{d,O}$ and $\mathcal{H}^{p,E}$ are 3x3 diagonal matrices with the diagonal elements ξ_d and ξ_p, respectively, whereas $\mathcal{H}^{d,O}$ is a 2x2 diagonal matrix with diagnoal elements ξ_d.

Expansion around the Γ-point

At the **Γ**-point in reciprocal space, $k_x = k_y = 0$ and thus $z_1 = z_2 = 1$. This results in the simplified expressions of the off-diagonal blocks of the Hamiltonian

$$T^{EO}_\Gamma = \sqrt{2} \begin{bmatrix} t^t_{51} + 2t^{l,t}_{51} & 0 & t^t_{53} + 2t^{l,t}_{53} \\ t^t_{41} + 2t^{l,t}_{41} & 0 & t^t_{43} + 2t^{l,t}_{43} \\ 0 & t^t_{12} + 2t^{l,t}_{12} & 0 \end{bmatrix}, \tag{5.83}$$

$$T^{OE}_\Gamma = \sqrt{2} \begin{bmatrix} t^t_{31} + 2t^{l,t}_{31} & 0 & t^t_{33} + 2t^{l,t}_{33} \\ 0 & t^t_{22} + 2t^{l,t}_{22} & 0 \end{bmatrix}. \tag{5.84}$$

In the Slater Koster decomposition some matrix elements are zero, i.e.,

$$t^t_{51} + 2t^{l,t}_{51} = 0, \quad t^t_{43} + 2t^{l,t}_{43} = 0, \quad t^t_{33} + 2t^{l,t}_{33} = 0, \tag{5.85}$$

which leads to further simplification. Only five non-zero off-diagonal elements remain and the Hamiltonian can be decoupled to five 2x2 matrices and one 1x1 matrix:

$$\{\alpha_5, \theta_3\}: \quad \begin{bmatrix} \xi_d & \sqrt{2}(t^t_{53} + 2t^{l,t}_{53}) \\ \sqrt{2}(t^t_{53} + 2t^{l,t}_{53}) & \xi_p \end{bmatrix}, \tag{5.86}$$

$$\{\alpha_4, \theta_1\}: \quad \begin{bmatrix} \xi_d & \sqrt{2}(t^t_{41} + 2t^{l,t}_{41}) \\ \sqrt{2}(t^t_{41} + 2t^{l,t}_{41}) & \xi_p \end{bmatrix}, \tag{5.87}$$

$$\{\alpha_1, \theta_2\}: \quad \begin{bmatrix} \xi_d & \sqrt{2}(t^t_{12} + 2t^{l,t}_{12}) \\ \sqrt{2}(t^t_{12} + 2t^{l,t}_{12}) & \xi_p \end{bmatrix}, \tag{5.88}$$

$$\{\alpha_3, \phi_1\}: \quad \begin{bmatrix} \xi_d & \sqrt{2}(t^t_{31} + 2t^{l,t}_{31}) \\ \sqrt{2}(t^t_{31} + 2t^{l,t}_{31}) & \xi_p \end{bmatrix}, \tag{5.89}$$

$$\{\alpha_2, \phi_2\}: \quad \begin{bmatrix} \xi_d & \sqrt{2}(t^t_{22} + 2t^{l,t}_{22}) \\ \sqrt{2}(t^t_{22} + 2t^{l,t}_{22}) & \xi_p \end{bmatrix}, \tag{5.90}$$

$$\{\phi_3\}: \quad \begin{bmatrix} \xi_p \end{bmatrix}. \tag{5.91}$$

These are trivial to diagonalize. For a given value of ξ_p, ξ_d, $V_{pd\pi}$ and $V_{pd\sigma}$, the numerical values of these analytical expressions can be obtained and compared with the numerical results from the d-subspace, previously obtained. These analytical expressions do indeed agree with the numerical results in the $\mathbf{\Gamma}$-point.

The lowest band of the d-bands is found to be

$$E(\alpha_5, \theta_3) = \frac{\xi_d + \xi_p}{2} - \sqrt{\left(\frac{\xi_d - \xi_p}{2}\right)^2 + 2\left(E^{1t}_{z,z^2} + 2E^{2t}_{z,z^2}\right)^2}. \tag{5.92}$$

Investigating the numerically obtained eigenvector of the lowest band when diagonalizing the full Hamiltonian in the $\mathbf{\Gamma}$-point, it shows that it is purely made up of the z^2 d-orbital. This agrees with the fact that the analytical expression for the lowest band is expressed in terms of the Slater Koster matrix elements E^{1t}_{z,z^2} and E^{2t}_{z,z^2}.

That $\xi_p < \xi_d$ means that the z^2 d-orbital is the d-orbital that couples to the p-orbitals the least. This could be explained by the fact that the d_{z^2} orbital is more spatially confined compared to the other d-orbitals, which results in a smaller overlap with the p-orbitals. For $\mathbf{k} \neq \mathbf{\Gamma}$ the eigenvector of the lowest d-band is a superposition of the five d-orbitals but still with a greatest contribution from the z^2 d-orbital.

Further, an expansion around the $\mathbf{K}$-point has been performed, see **Appendix B**. These calculations also show an agreement between the analytical and numerical results.

Including nearest neighbour coupling between the p-orbitals

The nearest neighbour coupling between the p-orbitals will now be included. As with the coupling between p- and d-orbitals, this will be expressed in terms of Slater Koster

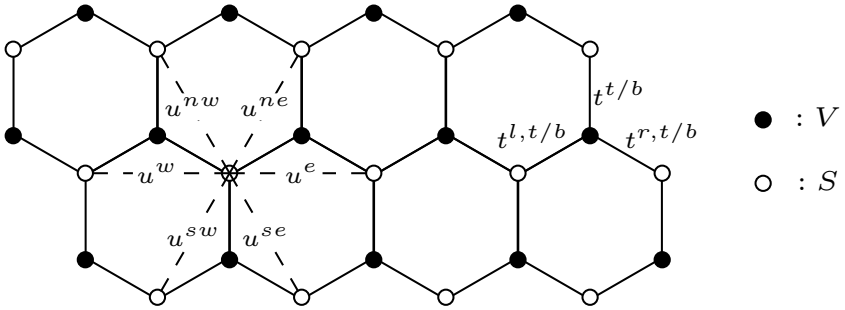

Fig. 5.10: Top view of the real space lattice of monolayer 2H-VS_2. All nearest neighbour couplings between p-orbitals and between p- and d-orbitals are indicated.

matrix elements, which for couplings between two p-orbitals are given by [29],

$$E_{x,x} = l^2 V_{pp\sigma} + (1-l^2)V_{pp\pi}, \tag{5.93}$$
$$E_{y,y} = m^2 V_{pp\sigma} + (1-m^2)V_{pp\pi}, \tag{5.94}$$
$$E_{z,z} = n^2 V_{pp\sigma} + (1-n^2)V_{pp\pi}, \tag{5.95}$$
$$E_{x,y} = lmV_{pp\sigma} - lmV_{pp\pi}, \tag{5.96}$$
$$E_{y,z} = mnV_{pp\sigma} - mnV_{pp\pi}, \tag{5.97}$$
$$E_{x,z} = lnV_{pp\sigma} - lnV_{pp\pi}. \tag{5.98}$$

$V_{pp\sigma}$ and $V_{pp\pi}$ denotes the bond integrals for a σ bond and a π bond between two p-orbitals, respectively. To the Hamiltonian, see Eq. (5.73), we must add the terms

$$\begin{aligned}\hat{\mathcal{H}}^{p,p} = \sum_{\mathbf{k}}\sum_{\nu\nu'}\sum_{i}^{t,b}\Big[&u^e z_1(\hat{p}^i_{\mathbf{k}\nu})^\dagger \hat{p}^i_{\mathbf{k}\nu'} + u^e z_1^*(\hat{p}^i_{\mathbf{k}\nu'})^\dagger \hat{p}^i_{\mathbf{k}\nu} \\ &+ u^{ne} z_2(\hat{p}^i_{\mathbf{k}\nu})^\dagger \hat{p}^i_{\mathbf{k}\nu'} + u^{ne} z_2^*(\hat{p}^i_{\mathbf{k}\nu'})^\dagger \hat{p}^i_{\mathbf{k}\nu} \\ &+ u^{nw} z_1^* z_2(\hat{p}^i_{\mathbf{k}\nu})^\dagger \hat{p}^i_{\mathbf{k}\nu'} + u^{nw} z_1 z_2^*(\hat{p}^i_{\mathbf{k}\nu'})^\dagger \hat{p}^i_{\mathbf{k}\nu}\Big].\end{aligned} \tag{5.99}$$

Defining

$$U = 2(c_1 u^e + c_2 u^{ne} + c_{12} u^{nw}), \tag{5.100}$$

with

$$c_1 = \frac{z_1 + z_1^*}{2}, \quad c_2 = \frac{z_2 + z_2^*}{2}, \quad c_{12} = \frac{z_1 z_2^* + z_2 z_1^*}{2}, \tag{5.101}$$

Eq. (5.99) can be written as

$$\hat{\mathcal{H}}^{p,p} = \sum_{\mathbf{k}}\sum_{\nu\nu'} U\left[(\hat{p}^t_{\mathbf{k}\nu})^\dagger \hat{p}^t_{\mathbf{k}\nu'} + (\hat{p}^b_{\mathbf{k}\nu})^\dagger \hat{p}^b_{\mathbf{k}\nu'}\right]. \tag{5.102}$$

Thus, Eq. (5.78) becomes

$$\begin{bmatrix} \mathcal{H}^d & T^E & T^O \\ (T^E)^\dagger & \mathcal{H}^p + U & 0 \\ (T^O)^\dagger & 0 & \mathcal{H}^p + U \end{bmatrix} \begin{bmatrix} \alpha \\ \theta \\ \phi \end{bmatrix} = E \begin{bmatrix} \alpha \\ \tau \\ \beta \end{bmatrix}. \tag{5.103}$$

In the Slater Koster decomposition, the components of Eq. (5.100) are of the form

$$u^e = \begin{bmatrix} u^e_{11} & 0 & 0 \\ 0 & u^e_{22} & 0 \\ 0 & 0 & u^e_{22} \end{bmatrix},\ u^{ne} = \begin{bmatrix} u^{ne}_{11} & u^{ne}_{12} & 0 \\ u^{ne}_{12} & u^{ne}_{22} & 0 \\ 0 & 0 & u^e_{22} \end{bmatrix},\ u^{nw} = \begin{bmatrix} u^{ne}_{11} & -u^{ne}_{12} & 0 \\ -u^{ne}_{12} & u^{ne}_{22} & 0 \\ 0 & 0 & u^e_{22} \end{bmatrix}. \quad (5.104)$$

Remember that $z_1 = 1$ and $z_2 = 1$ in the $\mathbf{\Gamma}$-point and thus $c_1 = 1$, $c_2 = 1$ and $c_{12} = 1$. This leads to

$$U^{\mathbf{\Gamma}} = 2(u^e + u^{ne} + u^{nw}) = \begin{bmatrix} u^e_{11} + 2u^{ne}_{11} & 0 & 0 \\ 0 & u^e_{22} + 2u^{ne}_{22} & 0 \\ 0 & 0 & 3u^e_{22} \end{bmatrix}. \quad (5.105)$$

Following the same procedure as applied to Eq. (5.78) results in a slightly modified expression for the energy of the lowest d-band in the $\mathbf{\Gamma}$-point;

$$E(\alpha_5, \theta_3) = \frac{\xi_d + \xi_p + U^{\mathbf{\Gamma}}_{11}}{2} - \sqrt{\left(\frac{\xi_d - \xi_p - U^{\mathbf{\Gamma}}_{11}}{2}\right)^2 + 2\left(E^{1t}_{z,z^2} + 2E^{2t}_{z,z^2}\right)^2}. \quad (5.106)$$

Again, the analytical results are identical to the numerically obtained results.

Further, we want to add the Coulomb repulsion between the electrons in the d-orbitals. In the following section the generalized Hubbard model will be derived and thereafter a mean-field (MF) approximation is applied on the obtained expression. Lastly, this will be included in the numerical calculations of the energy bands.

5.3.2 The Hubbard model

Derivation of the generalized Hubbard model

We begin from the Coulomb interaction term written in second quantization as

$$\hat{\mathcal{H}} = \frac{1}{2}\sum_{\sigma\sigma'}\int d\mathbf{r}d\mathbf{r}'\hat{\Psi}^\dagger_\sigma(\mathbf{r})\hat{\Psi}^\dagger_{\sigma'}(\mathbf{r}')V_{ee}(\mathbf{r}-\mathbf{r}')\hat{\Psi}_{\sigma'}(\mathbf{r}')\hat{\Psi}_\sigma(\mathbf{r}), \quad (5.107)$$

where

$$V_{ee}(\mathbf{r}-\mathbf{r}') = \frac{e^2}{4\pi\xi_0}\frac{1}{|\mathbf{r}-\mathbf{r}'|}, \quad (5.108)$$

is the repulsive Coulomb potential. $\hat{\Psi}_\sigma(\mathbf{r})$ is a fermionic field operator with spin σ at location $\mathbf{r}$. These field operators can be written in terms of ordinary first quantization wavefunctions ψ_ν and fermionic creation, or annihilation operators $\hat{c}^\dagger_{\nu\sigma}$, $\hat{c}_{\nu\sigma}$ using

$$\hat{\Psi}^\dagger_\sigma(\mathbf{r}) = \sum_\nu \psi^*_\nu \hat{c}^\dagger_{\nu\sigma} \quad \text{and} \quad \hat{\Psi}_\sigma(\mathbf{r}) = \sum_\nu \psi_\nu \hat{c}_{\nu\sigma}. \quad (5.109)$$

Thus, the Hamiltonian can be rewritten as

$$\hat{\mathcal{H}} = \frac{1}{2}\sum_{\sigma\sigma'}\sum_{ijkl}\sum_{\alpha\beta\mu\nu} V_{ijkl}^{\alpha\beta\mu\nu}\hat{c}_{i\alpha\sigma}^{\dagger}\hat{c}_{j\beta\sigma'}^{\dagger}\hat{c}_{k\mu\sigma'}\hat{c}_{l\nu\sigma}, \tag{5.110}$$

where we have defined

$$\begin{aligned} V_{\alpha\beta\mu\nu}^{ijkl} &= \langle i\alpha, j\beta|V_{ee}(\mathbf{r}-\mathbf{r}')|k\mu, l\nu\rangle \\ &= \int d\mathbf{r}d\mathbf{r}'\psi_{i\alpha}^{*}(\mathbf{r})\psi_{j\beta}^{*}(\mathbf{r}')V_{ee}(\mathbf{r}-\mathbf{r}')\psi_{k\mu}(\mathbf{r}')\psi_{l\nu}(\mathbf{r}). \end{aligned} \tag{5.111}$$

Due to the fact that this matrix product does not depend on spin, the Hamiltonian only has two spin indices σ and σ' and not four distinct spin indices. $\hat{c}_{i\alpha\sigma}^{\dagger}$ creates an electron in orbital i with spin σ at site α of the lattice. We will focus on the Coulomb repulsion between electrons in the d-orbitals, since both the p-d and p-p Coulomb repulsion is smaller compared to this. This has to do with the larger spatial extend of the two latter cases. Due to the very confined size of the d-orbitals, the Coulomb repulsion between electrons in d-orbitals at neighbouring sites will be neglected. Thus, only Coulomb repulsion between electrons in the same or different d-orbitals at the same site will be included. Therefore, we omit the sum over sites in the lattice and focus on the calculations of a single unit cell, i.e., with $\mathbf{r} = 0$. Thus, the indices α, β, μ and ν are neglected. The spin indices can each take two values $\uparrow$ and $\downarrow$, and the i, j, k and l indices each sum over the five d-orbitals. Thus, the Hamiltonian consists of many different terms, specifically 10^4 terms. Fortunately, many of these can be neglected. Let us investigate the most prominent terms.
In the following we will simplify the expressions using the number operators $\hat{n}_{i\sigma}$, $\hat{n}_i$ and the spin operators $\hat{\mathbf{S}}_i$ defined as

$$\hat{n}_{i\sigma} = \hat{c}_{i\sigma}^{\dagger}\hat{c}_{i\sigma} \quad , \quad \hat{n}_i = \hat{n}_{i\uparrow} + \hat{n}_{i\downarrow} \quad , \quad \hat{\mathbf{S}}_i = \frac{1}{2}\sum_{\alpha\beta}\hat{c}_{i\alpha}^{\dagger}\boldsymbol{\tau}_{\alpha\beta}\hat{c}_{\beta i}, \tag{5.112}$$

where $\boldsymbol{\tau}_{\alpha\beta} = ((\tau^x)_{\alpha\beta}, (\tau^y)_{\alpha\beta}, (\tau^z)_{\alpha\beta})$ is a vector consisting of the Pauli matrices. Further, we will define the matrix elements

$$U = V_{iiii} \quad , \quad V = V_{ijji} \quad , \quad J = -2V_{ijij} \quad , \quad Y = V_{iijj} \quad , \quad X = V_{iiij}. \tag{5.113}$$

Writing out the sum over spins for $i = j = k = l$ results in four terms, of which two terms cancel due to the Pauli principle

$$\begin{aligned} &\frac{1}{2}\sum_i U\left[\hat{c}_{i\uparrow}^{\dagger}\hat{c}_{i\downarrow}^{\dagger}\hat{c}_{i\downarrow}\hat{c}_{i\uparrow} + \hat{c}_{i\downarrow}^{\dagger}\hat{c}_{i\uparrow}^{\dagger}\hat{c}_{i\uparrow}\hat{c}_{i\downarrow} + \cancel{\hat{c}_{i\uparrow}^{\dagger}\hat{c}_{i\uparrow}^{\dagger}\hat{c}_{i\uparrow}\hat{c}_{i\uparrow}} + \cancel{\hat{c}_{i\downarrow}^{\dagger}\hat{c}_{i\downarrow}^{\dagger}\hat{c}_{i\downarrow}\hat{c}_{i\downarrow}}\right] \\ &= \sum_i U\hat{n}_{i\uparrow}\hat{n}_{i\downarrow}. \end{aligned} \tag{5.114}$$

The rewriting is done using the anti-commutator relations that fermionic creation and annihilation operators must obey, i.e.,

$$\{\hat{c}_i^{\dagger}, \hat{c}_j^{\dagger}\} = 0 \quad , \quad \{\hat{c}_i, \hat{c}_j\} = 0 \quad , \quad \{\hat{c}_i^{\dagger}, \hat{c}_j\} = \delta_{ij}. \tag{5.115}$$

When $i = l, j = k$ and $i \neq j$ the terms

$$\begin{aligned}
&\frac{1}{2}\sum_{ij} V \Big[\hat{c}^\dagger_{i\uparrow}\hat{c}^\dagger_{j\downarrow}\hat{c}_{j\downarrow}\hat{c}_{i\uparrow} + \hat{c}^\dagger_{i\downarrow}\hat{c}^\dagger_{j\uparrow}\hat{c}_{j\uparrow}\hat{c}_{i\downarrow} + \hat{c}^\dagger_{i\uparrow}\hat{c}^\dagger_{j\uparrow}\hat{c}_{j\uparrow}\hat{c}_{i\uparrow} + \hat{c}^\dagger_{i\downarrow}\hat{c}^\dagger_{j\downarrow}\hat{c}_{j\downarrow}\hat{c}_{i\downarrow} \\
&+ \hat{c}^\dagger_{j\uparrow}\hat{c}^\dagger_{i\downarrow}\hat{c}_{i\downarrow}\hat{c}_{j\uparrow} + \hat{c}^\dagger_{j\downarrow}\hat{c}^\dagger_{i\uparrow}\hat{c}_{i\uparrow}\hat{c}_{j\downarrow} + \hat{c}^\dagger_{j\uparrow}\hat{c}^\dagger_{i\uparrow}\hat{c}_{i\uparrow}\hat{c}_{j\uparrow} + \hat{c}^\dagger_{j\downarrow}\hat{c}^\dagger_{i\downarrow}\hat{c}_{i\downarrow}\hat{c}_{j\downarrow} \Big] \\
&= \sum_{ij} V \hat{n}_i \hat{n}_j,
\end{aligned} \tag{5.116}$$

arise. Eq. (5.114) and (5.116) describe the classical Coulomb repulsion. In the latter case the electrons are not occupying the same orbital.
If $i = k$ and $j = l$ and $i \neq j$, we get the terms

$$\begin{aligned}
&\frac{1}{2}\sum_{ij} V_{ijij} \Big[\hat{c}^\dagger_{i\uparrow}\hat{c}^\dagger_{j\uparrow}\hat{c}_{i\uparrow}\hat{c}_{j\uparrow} + \hat{c}^\dagger_{i\downarrow}\hat{c}^\dagger_{j\downarrow}\hat{c}_{i\downarrow}\hat{c}_{j\downarrow} + \hat{c}^\dagger_{i\uparrow}\hat{c}^\dagger_{j\downarrow}\hat{c}_{i\downarrow}\hat{c}_{j\uparrow} + \hat{c}^\dagger_{i\downarrow}\hat{c}^\dagger_{j\uparrow}\hat{c}_{i\uparrow}\hat{c}_{j\downarrow} \\
&+ \hat{c}^\dagger_{j\uparrow}\hat{c}^\dagger_{i\uparrow}\hat{c}_{j\uparrow}\hat{c}_{i\uparrow} + \hat{c}^\dagger_{j\downarrow}\hat{c}^\dagger_{i\downarrow}\hat{c}_{j\downarrow}\hat{c}_{i\downarrow} + \hat{c}^\dagger_{j\uparrow}\hat{c}^\dagger_{i\downarrow}\hat{c}_{j\downarrow}\hat{c}_{i\uparrow} + \hat{c}^\dagger_{j\downarrow}\hat{c}^\dagger_{i\uparrow}\hat{c}_{j\uparrow}\hat{c}_{i\downarrow} \Big] \\
&= -\sum_{ij} V_{ijij} \left[\hat{n}_{i\uparrow}\hat{n}_{j\uparrow} + \hat{n}_{i\downarrow}\hat{n}_{j\downarrow} + \hat{c}^\dagger_{i\uparrow}\hat{c}_{i\downarrow}\hat{c}^\dagger_{j\downarrow}\hat{c}_{j\uparrow} + \hat{c}^\dagger_{i\downarrow}\hat{c}_{i\uparrow}\hat{c}^\dagger_{j\uparrow}\hat{c}_{j\downarrow} \right].
\end{aligned} \tag{5.117}$$

The first two terms can be rewritten using

$$\hat{n}_{i\uparrow} = \frac{1}{2}\left(\hat{n}_{i\uparrow} + \hat{n}_{j\downarrow}\right) + \frac{1}{2}\left(\hat{n}_{i\uparrow} - \hat{n}_{j\downarrow}\right) = \frac{1}{2}\hat{n}_i + \hat{S}_{iz}, \tag{5.118}$$

and

$$\hat{n}_{i\downarrow} = \frac{1}{2}\left(\hat{n}_{i\uparrow} + \hat{n}_{j\downarrow}\right) - \frac{1}{2}\left(\hat{n}_{i\uparrow} - \hat{n}_{i\downarrow}\right) = \frac{1}{2}\hat{n}_i - \hat{S}_{iz}. \tag{5.119}$$

This leads to the expression

$$\begin{aligned}
&-\sum_{ij} V_{ijij} \left[\frac{1}{2}\hat{n}_i\hat{n}_j + 2\hat{S}_{iz}\hat{S}_{jz} + \hat{c}^\dagger_{i\uparrow}\hat{c}_{i\downarrow}\hat{c}^\dagger_{j\downarrow}\hat{c}_{j\uparrow} + \hat{c}^\dagger_{i\downarrow}\hat{c}_{i\uparrow}\hat{c}^\dagger_{j\uparrow}\hat{c}_{j\downarrow} \right] \\
&= \sum_{ij} J\hat{\mathbf{S}}_i \cdot \hat{\mathbf{S}}_j + \frac{1}{4}\sum_{ij} J\hat{n}_i\hat{n}_j.
\end{aligned} \tag{5.120}$$

The first term is the exchange coupling, and the second term is an extra Coulomb term. Since $J < 0$, see Eq. (5.113), the exchange coupling term is minimized for parallel spin. This is where Hund's first rule stems from. This rule states that the energy of a multi-electron atom is minimized for parallel spin.

If $i = j = k \neq l$, we obtain the following

$$\begin{aligned}
&\frac{1}{2}\sum_{ij}\sum_{\sigma} X \Big[\hat{c}^{\dagger}_{i\sigma}\hat{c}^{\dagger}_{i\bar{\sigma}}\hat{c}_{i\bar{\sigma}}\hat{c}_{j\sigma} + \hat{c}^{\dagger}_{j\sigma}\hat{c}^{\dagger}_{j\bar{\sigma}}\hat{c}_{j\bar{\sigma}}\hat{c}_{i\sigma} + \hat{c}^{\dagger}_{i\sigma}\hat{c}^{\dagger}_{j\bar{\sigma}}\hat{c}_{j\bar{\sigma}}\hat{c}_{j\sigma} + \hat{c}^{\dagger}_{j\sigma}\hat{c}^{\dagger}_{i\bar{\sigma}}\hat{c}_{i\bar{\sigma}}\hat{c}_{i\sigma} \\
&+ \hat{c}^{\dagger}_{i\sigma}\hat{c}^{\dagger}_{j\bar{\sigma}}\hat{c}_{i\bar{\sigma}}\hat{c}_{i\sigma} + \hat{c}^{\dagger}_{j\sigma}\hat{c}^{\dagger}_{i\bar{\sigma}}\hat{c}_{j\bar{\sigma}}\hat{c}_{j\sigma} + \hat{c}^{\dagger}_{i\sigma}\hat{c}^{\dagger}_{i\bar{\sigma}}\hat{c}_{j\bar{\sigma}}\hat{c}_{i\sigma} + \hat{c}^{\dagger}_{j\sigma}\hat{c}^{\dagger}_{j\bar{\sigma}}\hat{c}_{i\bar{\sigma}}\hat{c}_{j\sigma}\Big] \\
&= \sum_{ij}\sum_{\sigma} X\left(\hat{c}^{\dagger}_{i\sigma}\hat{c}_{j\sigma} + \hat{c}^{\dagger}_{j\sigma}\hat{c}_{i\sigma}\right)\left(\hat{n}_{i\bar{\sigma}} + \hat{n}_{j\bar{\sigma}}\right).
\end{aligned} \tag{5.121}$$

If i and j referred to different sites in the lattice, this term would be called the *bond-charge* interaction. As is evident from the expression, this term describe an electron hopping from one orbital to another, where the hopping amplitude depends on the occupation of that orbital of an electron with opposite spin.

Lastly, $i = j$, $k = l$ and $i \neq k$ results in

$$\begin{aligned}
&\frac{1}{2}\sum_{ij} Y\left[\hat{c}^{\dagger}_{i\uparrow}\hat{c}^{\dagger}_{i\downarrow}\hat{c}_{j\downarrow}\hat{c}_{j\uparrow} + \hat{c}^{\dagger}_{i\downarrow}\hat{c}^{\dagger}_{i\uparrow}\hat{c}_{j\uparrow}\hat{c}_{j\downarrow} + \cancel{\hat{c}^{\dagger}_{i\uparrow}\hat{c}^{\dagger}_{i\uparrow}\hat{c}_{j\uparrow}\hat{c}_{j\uparrow}} + \cancel{\hat{c}^{\dagger}_{i\downarrow}\hat{c}^{\dagger}_{i\downarrow}\hat{c}_{j\downarrow}\hat{c}_{j\downarrow}}\right] \\
&= \sum_{ij} Y\hat{c}^{\dagger}_{i\uparrow}\hat{c}^{\dagger}_{i\downarrow}\hat{c}_{j\downarrow}\hat{c}_{j\uparrow},
\end{aligned} \tag{5.122}$$

Two terms have been canceled due to the Pauli Principle. This term describes hopping of two electrons with opposite spin from one orbital to another. The terms with three different orbitals and four different orbitals are of even smaller magnitude than the terms already presented since the overlap in Eq. (5.111) decreases. These will thus be neglected. The Hamiltonian now reads

$$\begin{aligned}
\hat{\mathcal{H}} = &\sum_{i} U\hat{n}_{i\uparrow}\hat{n}_{i\downarrow} + \sum_{ij}\left(V + \frac{1}{4}J\right)\hat{n}_i\hat{n}_j + \sum_{ij} J\hat{\mathbf{S}}_i\cdot\hat{\mathbf{S}}_j \\
&+ \sum_{ij} Y\hat{c}^{\dagger}_{i\uparrow}\hat{c}^{\dagger}_{i\downarrow}\hat{c}_{j\downarrow}\hat{c}_{j\uparrow} + \sum_{ij}\sum_{\sigma} X\left(\hat{c}^{\dagger}_{i\sigma}\hat{c}_{j\sigma} + \hat{c}^{\dagger}_{j\sigma}\hat{c}_{i\sigma}\right)\left(\hat{n}_{i\bar{\sigma}} + \hat{n}_{j\bar{\sigma}}\right),
\end{aligned} \tag{5.123}$$

which is sometimes referred to as the *generalized Hubbard model*.

Mean-field approximation

The MF approximation can be used to decrease the number of degrees of freedom to make the Hamiltonian solvable. In practice the Hamiltonian is expanded around the mean of the field in terms of the magnitude and the fluctuations of the field. A number-operator can be written in terms of the mean field and the fluctuations as

$$\hat{n}_{i\sigma} = \langle\hat{n}_{i\sigma}\rangle + \Delta\hat{n}_{i\sigma}. \tag{5.124}$$

Using this, the product of two number-operators can be written as

$$\hat{n}_{i\sigma}\hat{n}_{j\sigma'} = \Delta\hat{n}_{i\sigma}\langle\hat{n}_{j\sigma'}\rangle + \Delta\hat{n}_{j\sigma'}\langle\hat{n}_{i\sigma}\rangle + \langle\hat{n}_{i\sigma}\rangle\langle\hat{n}_{j\sigma'}\rangle + \cancel{\Delta\hat{n}_{i\sigma}\Delta\hat{n}_{j\sigma'}}. \tag{5.125}$$

The fluctuations are assumed to be small and the second order term can be neglected. Rewriting $\Delta\hat{n}_{i\sigma} = \hat{n}_{i\sigma} - \langle\hat{n}_{i\sigma}\rangle$ and similarly for $\Delta\hat{n}_{j\sigma'}$, the expression becomes

$$\hat{n}_{i\sigma}\hat{n}_{j\sigma'} \simeq \langle\hat{n}_{i\sigma}\rangle\hat{n}_{j\sigma'} + \hat{n}_{i\sigma}\langle\hat{n}_{j\sigma'}\rangle - \langle\hat{n}_{i\sigma}\rangle\langle\hat{n}_{j\sigma'}\rangle. \tag{5.126}$$

The MF approximation will now be applied to the Hamiltonian in Eq. (5.123). This yields

$$\begin{aligned}
\hat{\mathcal{H}}^{MF} &= \sum_i U\left[\langle\hat{n}_{i\uparrow}\rangle\hat{n}_{i\downarrow} + \hat{n}_{i\uparrow}\langle\hat{n}_{i\downarrow}\rangle - \langle\hat{n}_{i\uparrow}\rangle\langle\hat{n}_{i\downarrow}\rangle\right] \\
&+ \sum_{ij}\left(V + \frac{1}{4}J\right)\left[\langle\hat{n}_i\rangle\hat{n}_j + \hat{n}_i\langle\hat{n}_j\rangle - \langle\hat{n}_i\rangle\langle\hat{n}_j\rangle\right] \\
&+ \sum_{ij} J\left[\langle\hat{\mathbf{S}}_i\rangle\cdot\hat{\mathbf{S}}_j + \hat{\mathbf{S}}_i\cdot\langle\hat{\mathbf{S}}_j\rangle - \langle\hat{\mathbf{S}}_i\rangle\cdot\langle\hat{\mathbf{S}}_j\rangle\right] \\
&+ \sum_{ij} Y\left[\langle\hat{c}^\dagger_{i\uparrow}\hat{c}_{j\uparrow}\rangle\hat{c}^\dagger_{i\downarrow}\hat{c}_{j\downarrow} + \hat{c}^\dagger_{i\uparrow}\hat{c}_{j\uparrow}\langle\hat{c}^\dagger_{i\downarrow}\hat{c}_{j\downarrow}\rangle - \langle\hat{c}^\dagger_{i\uparrow}\hat{c}_{j\uparrow}\rangle\langle\hat{c}^\dagger_{i\downarrow}\hat{c}_{j\downarrow}\rangle\right] \\
&+ \sum_{ij}\sum_{l\neq l'=i,j}\sum_\sigma X\Big[\langle\hat{c}_{l\sigma}\hat{c}_{l'\sigma}\rangle\hat{n}_{l\bar{\sigma}} + \hat{c}_{l\sigma}\hat{c}_{l'\sigma}\langle\hat{n}_{l\bar{\sigma}}\rangle - \langle\hat{c}_{l\sigma}\hat{c}_{l'\sigma}\rangle\langle\hat{n}_{l\bar{\sigma}}\rangle \\
&+ \langle\hat{c}_{l\sigma}\hat{c}_{l'\sigma}\rangle\hat{n}_{l'\bar{\sigma}} + \hat{c}_{l\sigma}\hat{c}_{l'\sigma}\langle\hat{n}_{l'\bar{\sigma}}\rangle - \langle\hat{c}_{l\sigma}\hat{c}_{l'\sigma}\rangle\langle\hat{n}_{l'\bar{\sigma}}\rangle\Big].
\end{aligned} \tag{5.127}$$

Hubbard estimated the magnitudes of these terms to be $U \simeq 20\,\text{eV}$, $V \simeq 2-3\,\text{eV}$, $X \simeq 1\,\text{eV}$ and $J \simeq Y \simeq 0.025\,\text{eV}$ [34]. In the following only the Hubbard terms will be included, i.e., the two first lines of Eq. (5.127). A sum over unit cells is introduced, indicated as a sum over $\mathbf{r}$. Note that the mean-fields does not depend on the position. Thus, we obtain

$$\begin{aligned}
\hat{\mathcal{H}}^{MF} &= U_0\sum_{\mathbf{r}}\sum_i\left[\langle\hat{n}_{i\uparrow}\rangle\hat{n}_{\mathbf{r}i\downarrow} + \hat{n}_{\mathbf{r}i\uparrow}\langle\hat{n}_{i\downarrow}\rangle - \langle\hat{n}_{i\uparrow}\rangle\langle\hat{n}_{i\downarrow}\rangle\right] \\
&+ U_1\sum_{\mathbf{r}}\sum_{ij}\left[\langle\hat{n}_i\rangle\hat{n}_{\mathbf{r}j} + \hat{n}_{\mathbf{r}i}\langle\hat{n}_j\rangle - \langle\hat{n}_i\rangle\langle\hat{n}_j\rangle\right],
\end{aligned} \tag{5.128}$$

where we have defined $U_1 = \left(V + \frac{1}{4}J\right)$. Further, we assume that both U_0 and U_1 have a constant value independent of the orbital. This expression can be Fourier transformed using Eq. (5.68). Thus, the MF Hubbard model for the full structure in the reciprocal space is described by

$$\begin{aligned}
\hat{\mathcal{H}}^{MF} &= \frac{U_0}{N}\sum_{\mathbf{k}\mathbf{k}'\in BZ}\sum_{\mathbf{r}}\sum_i e^{-i(\mathbf{k}-\mathbf{k}')\cdot\mathbf{r}}\left[\langle\hat{n}_{i\uparrow}\rangle\hat{n}_{\mathbf{k}i\downarrow} + \hat{n}_{\mathbf{k}'i\uparrow}\langle\hat{n}_{i\downarrow}\rangle - \langle\hat{n}_{i\uparrow}\rangle\langle\hat{n}_{i\downarrow}\rangle\right] \\
&\quad + \frac{U_1}{N}\sum_{\mathbf{k}\mathbf{k}'\in BZ}\sum_{\mathbf{r}}\sum_{ij} e^{-i(\mathbf{k}-\mathbf{k}')\cdot\mathbf{r}}\left[\langle\hat{n}_i\rangle\hat{n}_{\mathbf{k}j} + \hat{n}_{\mathbf{k}'i}\langle\hat{n}_j\rangle - \langle\hat{n}_i\rangle\langle\hat{n}_j\rangle\right] \\
&= \frac{U_0}{N}\sum_{\mathbf{k}\in BZ}\sum_i\left[\sum_\sigma\langle\hat{n}_{i\sigma}\rangle\hat{n}_{\mathbf{k}i\bar{\sigma}} - \langle\hat{n}_{i\uparrow}\rangle\langle\hat{n}_{i\downarrow}\rangle\right] \\
&\quad + \frac{U_1}{N}\sum_{\mathbf{k}\in BZ}\sum_{ij}\left[\langle\hat{n}_i\rangle\hat{n}_{\mathbf{k}j} + \hat{n}_{\mathbf{k}i}\langle\hat{n}_j\rangle - \langle\hat{n}_i\rangle\langle\hat{n}_j\rangle\right].
\end{aligned} \tag{5.129}$$

Implementing the Hubbard model in the band structure

The number operators can be written in the basis of the eigenvectors of the Hamiltonian, obtained numerically, using

$$\hat{c}^{\dagger}_{\mathbf{k}i\sigma} = \sum_{n=1}^{11} \alpha_{ni} \hat{c}^{\dagger}_{\mathbf{k}n\sigma}, \tag{5.130}$$

where n refer to the energy bands, and α is the amplitude of orbital i in the given band. Remember that there are eleven bands, since there are five d-bands and two times three p-bands. The expectation value of $\hat{n}_{i\sigma}(\mathbf{r})$ then becomes

$$\langle \hat{n}_{i\sigma}(\mathbf{r}) \rangle = \frac{1}{N} \sum_{n,m} \sum_{\mathbf{k} \in BZ} \alpha_{ni} \alpha^{*}_{mi} \langle \hat{c}^{\dagger}_{\mathbf{k}n\sigma} \hat{c}_{\mathbf{k}m\sigma} \rangle, \tag{5.131}$$

where we set $n = m$ since this is an excitation otherwise. Thus, we end with the expression

$$\langle \hat{n}_{i\sigma}(\mathbf{r}) \rangle = \frac{1}{N} \sum_{n \leq n_F} \sum_{\mathbf{k} \in BZ} |\alpha_{ni}|^2 \langle \hat{c}^{\dagger}_{\mathbf{k}n\sigma} \hat{c}_{\mathbf{k}n\sigma} \rangle. \tag{5.132}$$

The bands are filled with electrons up to the Fermi Surface, where n_F refer to the last band below the Fermi Energy. In the previous calculations of the energy bands, there were five d-bands and six p-bands, where each of these bands could contain two electrons, one of each spin. Since the Hubbard model affects electrons with spin $\uparrow$ and spin $\downarrow$ differently, the bands will be spin-resolved when including the Hubbard terms. Each spin band can contain one electron. Remember that after the vanadium atom has given two electrons to each sulfur atom in the unit cell, each sulfur atom contain six valence electrons whereas the vanadium atom only contains a single valence electron. Since the unit cell contains two sulfur atoms and a single vanadium atom, there are thirteen valence electrons in total. Since the twelve p-bands are lowest in energy, these are all filled and a single d-band is filled. Thus, we set $\langle \hat{c}^{\dagger}_{\mathbf{k}n\sigma} \hat{c}_{\mathbf{k}n\sigma} \rangle = 1$ for $n \leq n_F$ and zero otherwise. Finding the energy bands, without the Hubbard interaction included, it is evident from the eigenvector of the lowest d-band that this is mainly made up of the $d_{z^2\uparrow}$ orbital. Thus, for the first iteration including the Hubbard model, we approximate $\langle \hat{n}_{z^2\uparrow} \rangle = 1$ and all other mean-fields are set to zero. In this case the MF-Hamiltonian simplifies to

$$\hat{\mathcal{H}}^{MF} \simeq \sum_{\mathbf{k}} \left[\frac{U_0}{N} \hat{n}_{\mathbf{k}z^2\downarrow} + \frac{U_1}{N} \sum_{j \neq z^2} (\hat{n}_{\mathbf{k}j\uparrow} + \hat{n}_{\mathbf{k}j\downarrow}) \right], \tag{5.133}$$

where a factor of two has been absorbed into U_1. All constant terms drop out. From this a new value for $\langle \hat{n}_{z^2\uparrow} \rangle$ from the eigenvectors of the numerically solved Hamiltonian is found. This is repeated iteratively until self-consistency is reached. In these iterations the occupation of the other d-orbitals are also included in the Hamiltonian. In each iteration numerical integration over the first Brillouin zone is performed using a grid of

evenly spaced points of the Brillouin zone. The resulting $\langle \hat{n}_{z^2\uparrow} \rangle$ depends on the different parameters in the Hamiltonian. With $V_{pd\sigma} = 2.2$ eV, $V_{pd\pi} = -0.9$ eV, $V_{pp\sigma} = 0.974$ eV, $V_{pp\pi} = -0.19$ eV, $\xi_d = -0.774$ eV, $\xi_p = -1$ eV, $U_0 = 1.426$ eV and $U_1 = 2.17$ eV self-consistency is reached at $\langle \hat{n}_{z^2\uparrow} \rangle = 0.9769$. Thus, we can conclude that it is a good approximation that there is a single electron in the z^2 d-orbital with spin $\uparrow$. This is in agreement with the results from DFT. The projected density of states (PDOS) is the relative contribution of a particular orbital to the total density of states. The PDOS for the five d-orbitals on the vanadium atom in monolayer 2H-VS_2 is shown in **Fig. 5.11**. Positive PDOS corresponds to $\uparrow$ states and negative PDOS corresponds to spin $\downarrow$ states. The zero-point on the x-axis corresponds to the Fermi Energy. It is clear that just below the Fermi Energy, i.e., where the lowest d-band is located, the PDOS is only non-zero for the $z^2 \uparrow$ band.

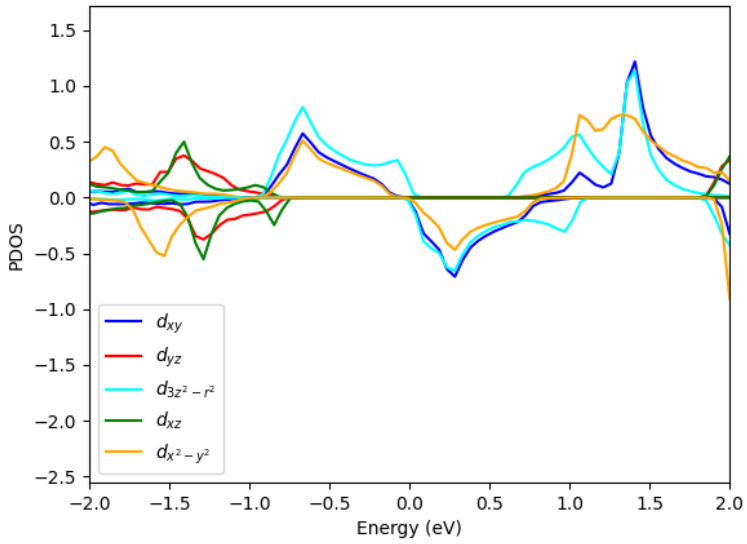

Fig. 5.11: The PDOS for the five d-orbitals on the vanadium atom in the 2H phase of monolayer VS_2. The Fermi level is located at zero energy. Positive PDOS corresponds to the PDOS for the spin $\uparrow$ d-orbitals and negative PDOS corresponds to spin $\downarrow$, (I. E. Castelli, personal communication, March 2020).

The fact that we obtain self-consistency at $\langle \hat{n}_{z^2\uparrow} \rangle = 0.9769$ allow us to approximate this to one and all other mean-fields to zero. Thus, we can use the simple expression for the Hubbard model in Eq. (5.133) when producing the band structures. Using the stated parameters the band structure viewed in **Fig. 5.12** is obtained. This is plotted alongside with the energy bands obtained from DFT for the same structure [3]. The energy bands obtained with the tight binding model and Hubbard model have been shifted in energy to be comparable to the DFT-calculated band structures.

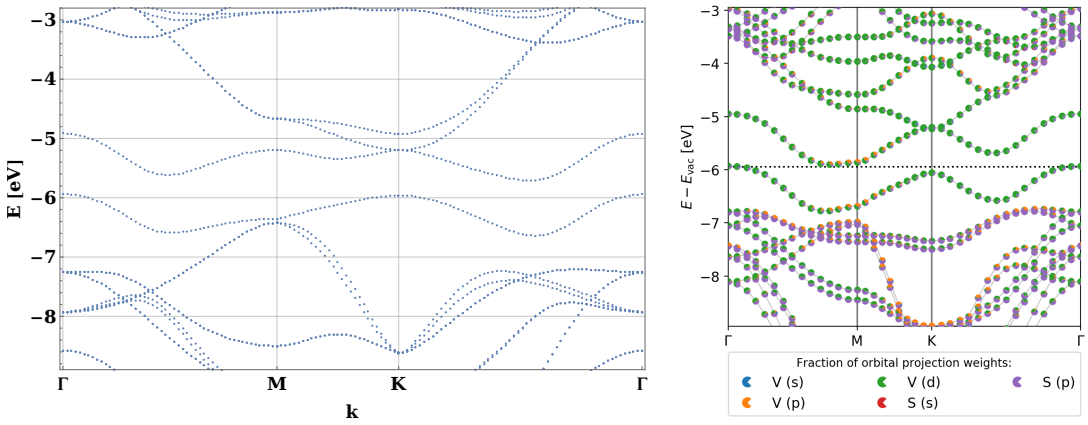

(a) (b)

Fig. 5.12: (a) The band structure for the 2H phase of monolayer VS_2 obtained from tight binding theory combined with the Hubbard model along the path $\mathbf{\Gamma} \to \mathbf{M} \to \mathbf{K} \to \mathbf{\Gamma}$. (b) Band structure of the same structure from DFT calculations from C2DB [3].

It is evident that the energy bands obtained from tight binding and the Hubbard model deviates from the energy bands obtained with DFT, though they definitely contain similar features. Most importantly, in both cases there is a gap between the lowest and the second lowest d-band. The Fermi Energy is located just below the highest energy of the lowest d-band. Thus, the density of states (DOS) is just above zero at the Fermi Level. This can also be viewed from the PDOS in **Fig. 5.11**. The band structures obtained from tight binding and the Hubbard model results in a metallic groundstate for the 2H phase of VS_2. The results from DFT [3] from which the relaxed structures are collected, are contradicting. The PBE[2] method results in a zero band gap though HSE[3] results in a band gap of 0.83 eV. Other DFT calculations [2] concludes a metallic groundstate for monolayer 2H VS_2.

Regardless of which is true, this means that the d-bands are fully (or almost fully) spin-polarized. The self-consistency calculations of $\langle \hat{n}_{z^2\uparrow} \rangle$ yields a similar conclusion as from the PDOS calculations from DFT, namely that the lowest d-band consists of a single electron located in the $d_{z^2\uparrow}$ orbital. Thus, the structure must be ferromagnetic. This agrees with the magnetic investigation of VS_2 by DFT [3] which find the 2H phase to be ferromagnetic. It is evident from the band structures that the spin-splitting is dependent on $\mathbf{k}$. The spin-splitting in the bands, that are not $d_{z^2\uparrow}$ and $d_{z^2\downarrow}$, obtained from DFT is more spin-split compared to the band structures obtained from tight binding and the Hubbard model. This could be explained by the fact that the exchange term, see Eq. (5.120), in the latter method is neglected. Within the MF-approximation, see Eq. (5.127), $\langle \hat{\mathbf{S}}_{z^2\uparrow} \rangle$ can be viewed as an external magnetic field that affects the bands differently depending on spin.

[2]Perdew–Burke-Ernzerhof
[3]Heyd–Scuseria–Ernzerhof

5.3.3 1T Structure

Following the same procedure as in the previous section, the 1T phase of monolayer VS_2 will be studied. As for the 2H phase of the VS_2 structure, there are three atoms in a unit cell, see **Fig. 5.13**. Contrary to the 2H phase, the x- and y-coordinates of the two sulfur sublayers do not coincide.

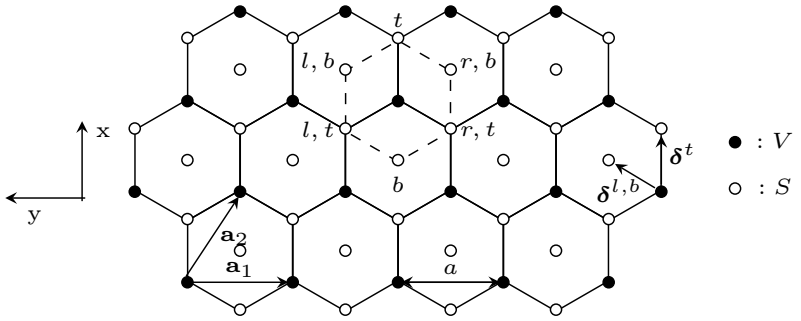

Fig. 5.13: Top view of the 1T phase of monolayer VS_2 in real space. The black (white) dots illustrates the vanadium (sulfur) atoms. The unit cell is shown with the dashed hexagon and the lattice vectors $\mathbf{a}_1$ and $\mathbf{a}_2$ are indicated. Further, the naming of the sulfur atoms partly present in the unit cell is indicated. The vectors $\boldsymbol{\delta}^{l,b}$ and $\boldsymbol{\delta}^t$ between the V and S atoms of the unit cell is shown. Lastly, the used coordinate system is illustrated.

In this case the Hamiltonian, only including the onsite energies and hopping between nearest neighbouring d- and p-sites, is

$$\begin{aligned}\hat{\mathcal{H}} = &\sum_{\mathbf{r}_i}\sum_{\mu=1}^{5}\xi_d\hat{d}^\dagger_{i,\mu}\hat{d}_{i,\mu} + \sum_{\mathbf{r}_i}\sum_{\nu=1}^{3}\xi_p\left[(\hat{p}^t_{i,\nu})^\dagger\hat{p}^t_{i,\nu} + (\hat{p}^{l,b}_{i,\nu})^\dagger\hat{p}^{l,b}_{i,\nu}\right] \\ &+ \sum_{\mathbf{r}_i}\sum_{\mu\nu}\left[t^t_{\mu\nu}\hat{d}^\dagger_{i,\mu}\hat{p}^t_{j,\nu} + t^{l,b}_{\mu\nu}\hat{d}^\dagger_{i,\mu}\hat{p}^{l,b}_{j,\nu} + h.c.\right] \\ &+ \sum_{\mathbf{r}_i}\sum_{\mathbf{r}_j=\mathbf{r}_i+\mathbf{a}_1-\mathbf{a}_2}\sum_{\mu\nu}\left[t^{r,t}_{\mu\nu}\hat{d}^\dagger_{i,\mu}\hat{p}^t_{j,\nu} + t^b_{\mu\nu}\hat{d}^\dagger_{i,\mu}\hat{p}^{l,b}_{j,\nu} + h.c.\right] \\ &+ \sum_{\mathbf{r}_i}\sum_{\mathbf{r}_j=\mathbf{r}_i+\mathbf{a}_1}\sum_{\mu\nu}\left[t^{r,b}_{\mu\nu}\hat{d}^\dagger_{i,\mu}\hat{p}^{r,b}_{j,\nu} + h.c.\right] \\ &+ \sum_{\mathbf{r}_i}\sum_{\mathbf{r}_j=\mathbf{r}_i-\mathbf{a}_2}\sum_{\mu\nu}\left[t^{l,t}_{\mu\nu}\hat{d}^\dagger_{i,\mu}\hat{p}^t_{j,\nu} + h.c.\right].\end{aligned} \tag{5.134}$$

We have defined the following matrix-elements

$$t^t_{\mu\nu} = \langle\mathbf{r}_i; d_\mu|\hat{\mathcal{H}}_t|\mathbf{r}_i + \boldsymbol{\delta}^t; p_\nu\rangle, \tag{5.135}$$
$$t^{l,b}_{\mu\nu} = \langle\mathbf{r}_i; d_\mu|\hat{\mathcal{H}}_t|\mathbf{r}_i + \boldsymbol{\delta}^{l,b}; p_\nu\rangle, \tag{5.136}$$
$$t^{r,t}_{\mu\nu} = \langle\mathbf{r}_i; d_\mu|\hat{\mathcal{H}}_t|\mathbf{r}_i + \boldsymbol{\delta}^t + \mathbf{a}_1 - \mathbf{a}_2; p_\nu\rangle, \tag{5.137}$$
$$t^b_{\mu\nu} = \langle\mathbf{r}_i; d_\mu|\hat{\mathcal{H}}_t|\mathbf{r}_i + \boldsymbol{\delta}^{l,b} + \mathbf{a}_1 - \mathbf{a}_2; p_\nu\rangle, \tag{5.138}$$
$$t^{r,b}_{\mu\nu} = \langle\mathbf{r}_i; d_\mu|\hat{\mathcal{H}}_t|\mathbf{r}_i + \boldsymbol{\delta}^{l,b} + \mathbf{a}_1; p_\nu\rangle, \tag{5.139}$$
$$t^{l,t}_{\mu\nu} = \langle\mathbf{r}_i; d_\mu|\hat{\mathcal{H}}_t|\mathbf{r}_i + \boldsymbol{\delta}^t - \mathbf{a}_2; p_\nu\rangle, \tag{5.140}$$

where $\hat{\mathcal{H}}_t$ is the tight binding Hamiltonian, see Eq. (5.1). The coupling lines are viewed in **Fig. 5.14**. In the Slater Koster decomposition, these are of the form

$$\begin{aligned} t^t &= \begin{bmatrix} 0 & t^t_{12} & t^t_{13} \\ 0 & t^t_{22} & t^t_{23} \\ t^t_{31} & 0 & 0 \\ t^t_{41} & 0 & 0 \\ 0 & t^t_{52} & t^t_{53} \end{bmatrix} = -t^b \quad , \quad t^{l,b} = \begin{bmatrix} t^{l,b}_{11} & t^{l,b}_{12} & t^{l,b}_{13} \\ t^{l,b}_{21} & t^{l,b}_{22} & t^{l,b}_{23} \\ t^{l,b}_{31} & t^{l,b}_{32} & t^{l,b}_{33} \\ t^{l,b}_{41} & t^{l,b}_{42} & t^{l,b}_{43} \\ t^{l,b}_{51} & t^{l,b}_{52} & t^{l,b}_{53} \end{bmatrix} = -t^{r,t}, \\ t^{r,b} &= \begin{bmatrix} t^{r,b}_{11} & t^{r,b}_{12} & t^{r,b}_{13} \\ t^{r,b}_{21} & t^{r,b}_{22} & t^{r,b}_{23} \\ t^{r,b}_{31} & t^{r,b}_{32} & t^{r,b}_{33} \\ t^{r,b}_{41} & t^{r,b}_{42} & t^{r,b}_{43} \\ t^{r,b}_{51} & t^{r,b}_{52} & t^{r,b}_{53} \end{bmatrix} = -t^{l,t}. \end{aligned} \tag{5.141}$$

The Hamiltonian can now be Fourier transformed and simplified following a similar procedure as in **section 5.3.1**. This leads to the Hamiltonian

$$\begin{aligned} \hat{\mathcal{H}} = \sum_{\mathbf{k}} \Bigg[& \xi_d \sum_{\mu} \hat{d}^\dagger_{\mathbf{k},\mu} \hat{d}_{\mathbf{k},\mu} + \xi_p \sum_{\nu} \left[(p^t_{\mathbf{k},\nu})^\dagger p^t_{\mathbf{k},\nu} + (p^{l,b}_{\mathbf{k},\nu})^\dagger p^{l,b}_{\mathbf{k},\nu} \right] \\ & + \sum_{\mu\nu} \left(T^t_{\mu\nu} \hat{d}^\dagger_{\mathbf{k},\mu} \hat{p}^t_{\mathbf{k},\nu} + T^{l,b} \hat{d}^\dagger_{\mathbf{k},\mu} \hat{p}^{l,b}_{\mathbf{k},\nu} + h.c. \right) \Bigg], \end{aligned} \tag{5.142}$$

where we have defined

$$T^t = c_t \left(t^t + z_2^* t^{l,t} + z_1 z_2^* t^{r,t} \right), \quad T^{l,b} = c_b \left(t^{l,b} + z_1 t^{r,b} + z_1 z_2^* t^b \right) \tag{5.143}$$

with

$$c_t = e^{i\mathbf{k}\cdot\boldsymbol{\delta}^t}, \quad c_b = e^{i\mathbf{k}\cdot\boldsymbol{\delta}^{l,b}}. \tag{5.144}$$

z_1 and z_2 are given in Eq. (5.72). We approximate $c_t \simeq 1$ and $c_b \simeq 1$ as in the last section. The shape of the Brillouin zone of the 1T phase is identical to that of the 2H phase. Thus, the expressions for the high symmetry-points used for the 2H phase, expressed in terms of the lattice constant, see Eq. (5.55), are the same here. The distances between the atoms in the two structures are not completely identical. From the DFT calculated relaxed structure, the lattice constant is found to be $a = 3.195$ Å for the 1T phase compared to $a = 3.186$ Å for the 2H phase [3]. Due to the proximity of these the lattice parameters of the 1T structure will be approximated to be the same as for the 2H phase.

The coupling between neighbouring p-orbitals can now be added. Remember that only couplings between p-orbitals at nearest neighbouring sulfur atoms in the same layer are included. This is thus straightforward to include using the results from **section 5.3.1**. These coupling lines are also illustrated in **Fig. 5.14**.

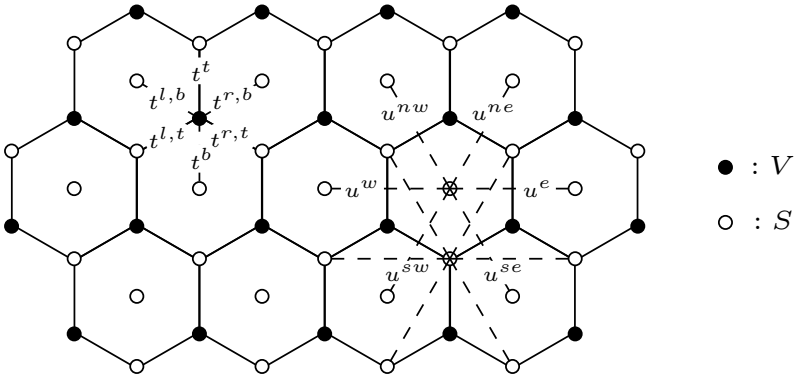

Fig. 5.14: Top view of the 1T phase of monolayer VS_2. All nearest neighbour couplings between p-orbitals are indicated with dashed lines. Only the nomenclature for one sulfur atom is indicated, since the nomenclature of the other is the same. Similarly, all nearest neighbour couplings between p- and d-orbitals are indicated.

As in **section 5.3.1** we can now find the five energy bands of the d-orbitals in the d-subspace to obtain a preliminary view of the band structure before adding the Hubbard model. From the numerically obtained eigenvectors, it is observed that the lowest d-band is mainly occupied by an electron in the d_{z^2}-orbital, though this is not as pronounced as in the 2H phase. The self-consistent calculation for $\langle \hat{n}_{z^2\uparrow} \rangle$ cannot be performed here, at least not in the same simple way as in the previous section. This is due to the fact that the calculation would not only include a single d-band as previously. In the 1T phase there are two bands, namely the $d_{z^2\uparrow}$ and the $d_{z^2\downarrow}$, that are partially occupied. For this reason the Hubbard model will be implemented in a slightly different way compared to the previous section, where both of these two bands will be included as

$$\begin{aligned}\mathcal{H}^{MF} \simeq \sum_{\mathbf{k}} \Bigg[& \frac{U_0 x}{N} \hat{n}_{\mathbf{k}z^2\downarrow} + \frac{U_1 x}{N} \sum_{j \neq z^2} (\hat{n}_{\mathbf{k}j\uparrow} + \hat{n}_{\mathbf{k}j\downarrow}) + \frac{U_0(1-x)}{N} \hat{n}_{\mathbf{k}z^2\uparrow} \\ & + \frac{U_1(1-x)}{N} \sum_{j \neq z^2} (\hat{n}_{\mathbf{k}j\downarrow} + \hat{n}_{\mathbf{k}j\uparrow}) \Bigg] \\ = \sum_{\mathbf{k}} \Bigg[& \frac{U_0 x}{N} \hat{n}_{\mathbf{k}z^2\downarrow} + \frac{U_0(1-x)}{N} \hat{n}_{\mathbf{k}z^2\uparrow} + \frac{U_1}{N} \sum_{j \neq z^2} (\hat{n}_{\mathbf{k}j\downarrow} + \hat{n}_{\mathbf{k}j\uparrow}) \Bigg] . \end{aligned} \tag{5.145}$$

x is a unitless number between zero and one, that quantifies the occupation of the $d_{z^2\uparrow}$ band and the $d_{z^2\downarrow}$ band. Contrary to the case of the 2H phase, the constants do not cancel, since both $\langle \hat{n}_{z^2\uparrow} \rangle \neq 0$ and $\langle \hat{n}_{z^2\downarrow} \rangle \neq 0$. These terms will still be neglected since any constant shift does not affect the dynamics of the band structures. Just below the Fermi energy, the main contribution to the PDOS comes from the $d_{z^2\uparrow}$ orbital, see **Fig. 5.15**, though it is evident that both the xz and $x^2 - y^2$ d-orbitals are also present. These are neglected in the calculations performed here.

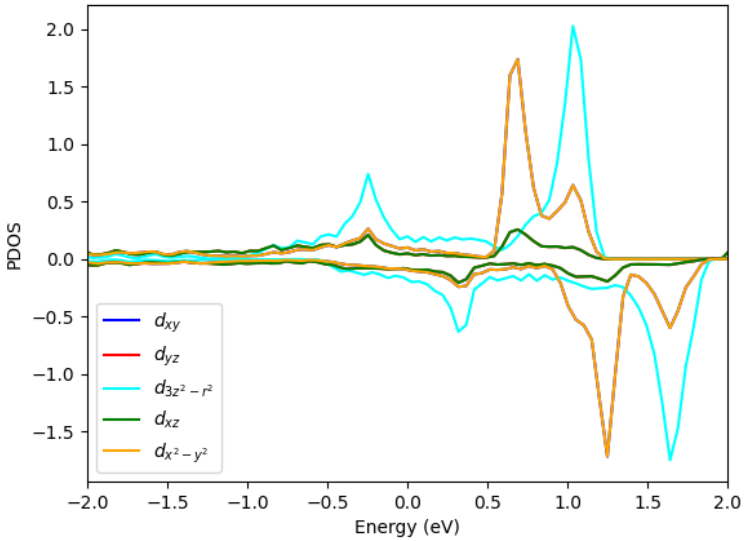

Fig. 5.15: The PDOS for the five d-orbitals in the 1T phase of monolayer VS_2. The Fermi Energy is located at zero energy. Positive PDOS corresponds to the PDOS for the spin ↑ d-orbitals and negative PDOS corresponds to spin ↓, (I. E. Castelli, personal communication, March 2020).

The final band structure is depicted in **Fig. 5.16** alongside with the band structure from DFT [3]. The parameters used to obtain the former are $V_{pd\sigma} = 2.2$ eV, $V_{pd\pi} = -0.9$ eV, $V_{pp\sigma} = 0.974$ eV, $V_{pp\pi} = -0.19$ eV, $\xi_d = -0.774$ eV, $\xi_p = -1$ eV, $U_0 = 1.426$ eV, $U_1 = 2.17$ eV and $x = 0.732$. Further, the bands have been shifted in energy to be comparable to the band structures obtained with DFT. Also here, there are some deviations in the two band structures, though the main points are evident from both plots. Both band structures suggests a metallic groundstate for monolayer 1T-VS_2. This is also clearly observed from the PDOS in **Fig. 5.15**. Here, the $d_{z^2\uparrow}$ and $d_{z^2\downarrow}$ bands are only partially spin-polarized. Thus, this structure is also ferromagnetic, though with a lower magnetization compared to the 2H phase. This agrees with the results from DFT calculations that find the magnetic moment to be 0.49 au for the 1T phase compared to a magnetic moment of 0.95 au for the 2H phase.

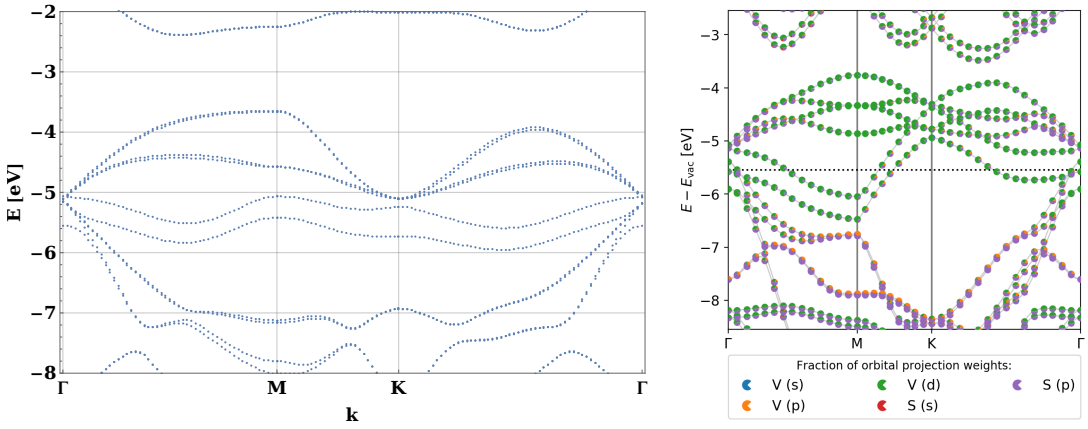

(a) (b)

Fig. 5.16: (a) The band structure for the 1T phase of monolayer VS_2 obtained from tight binding theory combined with the Hubbard model along the path $\mathbf{\Gamma} \to \mathbf{M} \to \mathbf{K} \to \mathbf{\Gamma}$. (b) Band structure obtained from DFT calculations [3].

5.4 Conclusion

First, the hypothetical model complex VS_6 was studied using the tight binding method in the Slater Koster decomposition. Degeneracies in the energy sepctrum was observed both for the 1T and 2H phase, see **Fig. 5.3** and **Fig. 5.7**. These degeneracies were explained by the different symmetries of the two molecules using a group theoretical approach. A specific high-symmetrical case of the 1T phase was explored, for which the degeneracy of the spectrum changed, see **Fig. 5.6**. Subsequently, monolayer VS_2 was investigated using the tight binding method together with the Hubbard model. For both phases the band structure was obtained, see **Fig. 5.16** and **Fig. 5.12**. The 2H structure was found to exhibit a metallic groundstate, though the highest non-empty band was almost filled. Thus, the groundstate was found to be highly spin-polarized and the compound exhibited a ferromagnetic ordering. This agrees with the DFT calculations from Wang et al. [2]. The DFT calculations from DTU [3] showed contradicting results, though one method also suggested a metallic, ferromagnetic groundstate. Both the PDOS of the d-orbitals and a self-consistent calculation of $\langle \hat{n}_{z^2\uparrow} \rangle$ also yielded a ferromagnetic ordering. Similarly, the 1T phase was found to be metallic in agreement with the DFT calculations. This was only partially spin polarized and thus had a smaller magnetic moment. This result agrees with DFT calculations [3].

Chapter 6

$CrCl_2(pyz)_2$

6.1 Introduction to $CrCl_2(pyz)_2$[1]

Chromium-chloride-pyrazine, $CrCl_2(pyz)_2$, was synthesized by an international group at the chemistry department at DTU, lead by assistant professor Kasper Steen Pedersen [4]. This is the first organic and inorganic hybrid 2D material ever produced. The fact that it is both organic and inorganic, in contrast to graphene and all other previously synthesized 2D materials, makes it highly tunable. This material is made in such a way that parts of the material can be replaced, which allow for a more accurate design of both the electrical and the magnetic properties of the material.

The structure of $CrCl_2(pyz)_2$ is viewed in **Fig. 6.1**. One layer of $CrCl_2(pyz)_2$ consists of chromium atoms crystallized in a lattice exhibiting orthorhombic symmetry that couple through pyrazine rings and are sandwiched in between two layers of chlorine atoms, see **Fig. 6.1 a** and **b**. This will be introduced in greater detail below. In **Fig. 6.1 b** it is evident that the 2D layers, when stacked, couples through the VdW interaction. The fact that the interaction between the layers are so weak makes it possible to tune the magnetic properties using a weak external magnetic field. Chromium-chloride-pyrazine exhibits both long-range magnetic order together with high 2D electronic conductivity, which not only makes the material of interest in regards to quantum computing but also in future superconductors, catalysts, batteries, fuel cells and in electronics in general.

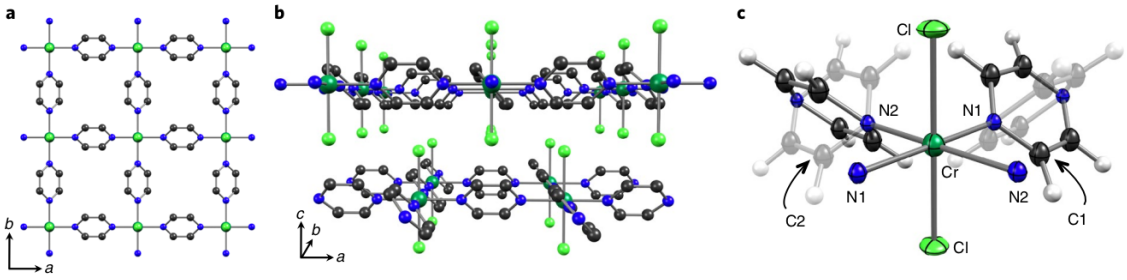

Fig. 6.1: A view of the structure of $CrCl_2(pyz)_2$. **a** The structure viewed along the Cl-Cr-Cl axis. **b** Side view of the layered material. **c** Thermal ellipsoid[2]plot at 80% probability level. The structure consists of carbon atoms (black), nitrogen atoms (blue), chromium atoms (dark green) and chlorine atoms (light green) as indicated in **c**. For clarity, the hydrogen atoms of the pyrazine rings has been omitted in **a** and **b**. This figure is taken from the paper by Pedersen et al. [4].

[1]This introduction is based on [35] and [4].

[2]Thermal ellipsoids illustrates the magnitude and direction of the thermal vibrations.

First, the experimental results obtained by Petersen et al. will be sketched, since this gives valuable information about the compund that can be used in the following calculations. Thereafter, the hypothetical model complex $CrCl_2(pyz)_4$ is studied and the energy spectrum of this is obtained using the Slater Koster decomposition of the tight binding model. Further, the symmetries of this molecule will be investigated using group theory. Subsequently, monolayer $CrCl_2(pyz)_2$ is explored. Using the tight binding model, the band structure will be obtained and compared to DFT calculations from Pedersen et al. [4]. Lastly, the magnetic properties of the compound will be considered. First, a simple model will be proposed to describe the behaviour of the relevant spins in the compound. The exchange interaction between electrons on neighbouring chromium and pyrazine sites is calculated, and an expression of the indirect exchange interaction between neighbouring chromium sites is found using the RKKY model. Lastly, an expression for this coupling constant in terms of the ordering temperature is obtained using MF theory.

6.2 Experimental Results of $CrCl_2(pyz)_2$

This section portrays the experimental and numerical results by Pedersen et al. [4]. In the following sections the electronic and magnetic properties of the compound is investigated analytically and compared to these results. First, they solve the crystal structure shown in **Fig. 6.1** using synchrotron X-ray powder diffraction data. To examine the oxidation of the Cr-ions in $CrCl_2(pyz)_2$, it is compared to two mononuclear model complexes, namely *trans*[3]-$[CrCl_2(NCNH_2)_4]$ (Cr(II)) and *trans*-$[CrCl_2(\text{pyridine})_4](ClO_4)\cdot 1/4\ H_2O$ (Cr(III)) with the established oxidations Cr^{+2} and Cr^{+3}, respectively. The bond lengths around the chromium atom in $CrCl_2(pyz)_2$ is comparable to the bond lengths in Cr(III) which could indicate that the chromium atom in $CrCl_2(pyz)_2$ possess a $+3$ oxidation. This is further investigated by X-ray absorption spectroscopy (XAS), collected at the Cr and Cl K-edge[4] of $CrCl_2(pyz)_2$, Cr(II) and Cr(III), see **Fig. 6.2**. Both the Cr and the Cl K-edge XAS spectra of $CrCl_2(pyz)_2$ show a great resemblance with the same spectra obtained for Cr(III). Thus, it is concluded that the Cr in $CrCl_2(pyz)_2$ possess $+3$ oxidation, which means that an extra electron has been collected by the two pyrazine rings. This is confirmed by DFT calculations.

In **Fig. 6.2 c** the conductivity as a function of temperature is depicted. The room-temperature is measured to be $\sigma_{RT} = 32 mScm^{-1}$, which makes $CrCl_2(pyz)_2$ one of the more conducting coordination solids reported so far [36], [37][5]. The fact that the conductivity increases for increasing temperature indicates an insulating groundstate. Contrary to this, DFT calculations of the ferrimagnetic case suggests a metalic groundstate. This will be elaborated below.

[3] *Cis* and *trans* refer to two different isomers of the same molecules. These prefixes stem from Latin where *Cis* means "this side of" and *trans* means "the other side of". This refer to the placement of the functional group with respect to the carbon chain.

[4] K-edge in XAS refer to a sudden increase in the absorption when the energy of the x-rays is just above the binding energy of the innermost electron shell of the atoms interacting with the photons.

[5] Siemens (S) is the derived unit of electric conductance. In SI-units this is $kg^{-1}m^{-2}s^3A^2$.

The measured conductivity clearly fits well with the 2D Mott law described by

$$\sigma(T) = \sigma_0 \exp\left(-\left(\frac{T_0}{T}\right)^{\frac{1}{d+1}}\right), \tag{6.1}$$

where d is the dimensionality of transport, in this case $d = 2$, and σ_0 and T_0 are empirical constants.

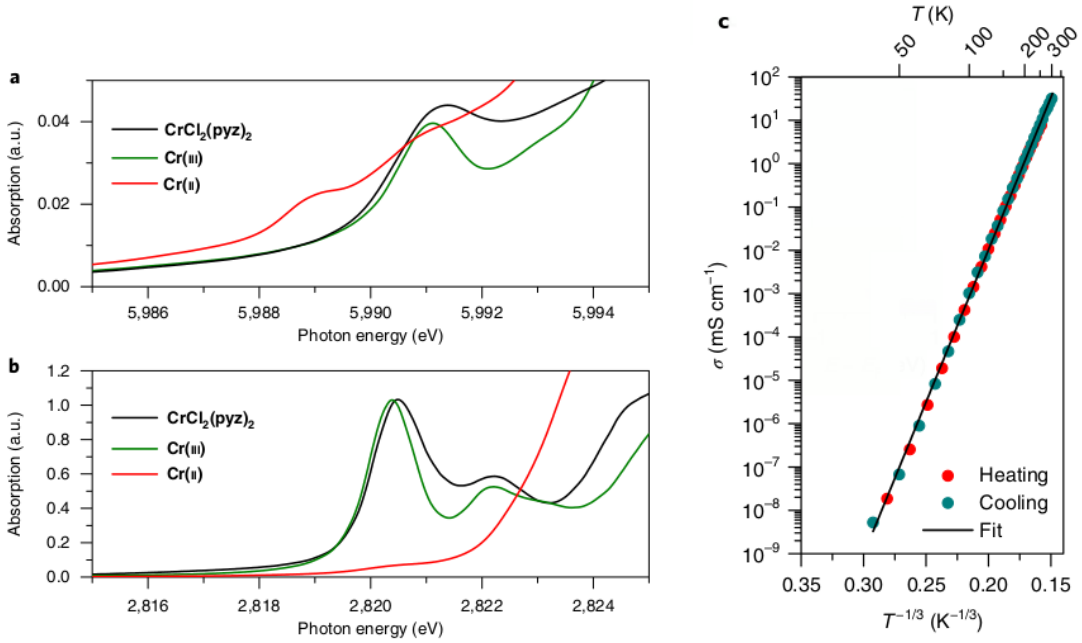

Fig. 6.2: XAS spectra of $CrCl_2(pyz)_2$, Cr(II) and Cr(III) at $T = 3$ K for Cr K-edge **a** and Cl K-edge **b**. **c** Temperature dependence of the conductivity of $CrCl_2(pyz)_2$. The solid line shows the best fit to the Mott law, see Eq. (6.1), with $\sigma_0 = 1.2 \cdot 10^{12} mScm^{-1}$ and $T_0 = 4.2 \cdot 10^6$ K. This figure is produced by Pedersen et al. [4].

Further, the magnetic properties of $CrCl_2(pyz)_2$ has been investigated. The magnetic susceptibility-temperature product, χT, is measured, see **Fig. 6.3 a**, to be 2.7 cm^3Kmol^{-1}, 3.3 cm^3Kmol^{-1} and 4.7 cm^3Kmol^{-1} at 400 K, 300 K and 200 K, respectively. This thermal behaviour indicates strong magnetic interactions, and the Curie-Weiss law does not describe this well. Though, for high temperatures it is a fine approximation, and from this the spin on the Cr-ions are estimated to be either 3/2 or 2, see **Appendix C**. A sudden increase in χT is observed at ~ 55 K, which indicates that a phase transition to an ordered phase has occured. A hysteric behaviour is observed in the magnetic field dependence of the magnetization, see **Fig. 6.3 b**, where the remnant magnetization as a function of temperature is shown in the inset. Clearly, only a remnant magnetization is present for temperatures below ~ 55 K, which supports the suggestion of a phase transition. This ordering temperature is much higher than previously reported ordering temperatures for pyrazine-networks. The saturation magnetization at 7 T and 1.85 K is measured to be 1.8 μ_B. If the spin on the

chromium atoms coupled ferromagnetically to the radical spins on the pyrazine rings this would be expected to be $\sim 4\mu_B$. For an antiferromagnetically coupling this should be around $2\mu_B$. Thus, this indicates an intralayer antiferromagnetic coupling with a parallel alignment of the layer magnetic moments, such that a resulting magnetization remains. DFT calculations show a significant spin density on the pyrazine rings and the

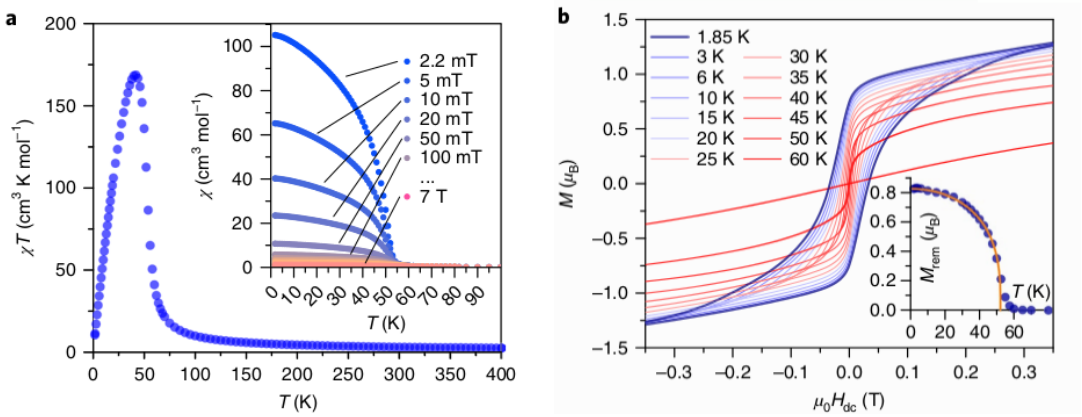

Fig. 6.3: **a** Susceptibility-temperature product as a function of temperature measured with a d.c. magnetic field at $\mu_0 H_{dc} = 0.1$ T applied. Inset: Temperature dependence of magnetic susceptibility for various d.c. field strengths. **b** Magnetic field dependence of the magnetization at selected temperatures measured with a sweep rate of 30 Oe min^{-1}. Inset: Remnant magnetization as a function of temperature. The solid line is a simulation of the temperature dependence of the remnant magnetization using $M_{rem} \propto \left(1 - \left(\frac{T}{T_c}\right)^{\alpha}\right)^{\beta}$ with $\alpha = 2.0$, $\beta = 0.33$ and $T_c = 52$ K. This figure is collected from Pedersen et al. [4].

antiferromagnetic exchange coupling between the Cr^{3+}-ions and the pyz radical spins is estimated to be $\sim -2,000\ \text{cm}^{-1} \simeq -0.25$ eV. The alignment of the magnetic moments has also been investigated with DFT calculations. Two states have been compared, the experimentally observed ferrimagnetic state and the antiferromagnetic state, i.e., where the layer magnetic moments couple antiferromagnetically. The DFT-optimized structures have similar lattice constants, which do not deviate significantly from the experimental results. In both cases the local magnetic moments on the pyz ligands are found to be antiparallel to the local magnetic moments on the Cr-ions, and the local magnetic moment on the Cr atoms is estimated from DFT calculations to be $\sim 2.54\mu_B$. This is significantly smaller than the expected $\sim 3\mu_B$ for $S = 3/2$. To be able to determine this experimentally, X-ray magnetic circular dichroism (XMCD) experiments have been performed from which the Cr local magnetic moment is estimated to be $2.3\mu_B$, see **Fig. D.1** in **Appendix D**. From DFT the total magnetization of a unit cell is found to be $1.98\mu_B$. This agrees with the measured value, $1.8\mu_B$. The band structures of both states and the PDOS are viewed and compared to the band structures produced in the following section. DFT calculations suggests a strong degree of $\pi - d$ conjugation which could explain both the high magnetic ordering temperature and the high electrical conductivity.

6.3 Model complex $CrCl_2(pyz)_4$

To begin with the energy levels and symmetries of the model complex $CrCl_2(pyz)_4$ is investigated. This molecule is viewed in **Fig. 6.4**. For the calculations in this section to be applicable, when investigating monolayer $CrCl_2(pyz)_2$, the stoichiometry used in this section will be that of $CrCl_2(pyz)_2$ and not $CrCl_2(pyz)_4$. One unit cell of $CrCl_2(pyz)_2$ consists of one Cr-ion, two Cl-ions and two pyrazine rings. The electron configuration for Cr and Cl is $[Ar]4s^13d^5$ and $[Ne]3s^23p^5$, respectively. Thus, each chlorine atom collects an electron from the chromium atom, which is then reduced by two electrons. As argued from DFT caulcations in the previous section, the two pyrazine rings reduces the Cr atom of an extra electron, such that three electrons remain in an unfilled d-shell on the Cr-ion. If these spins occupy three distinct energy levels and align parallely to each other, to obey Hund's first rule, the spin on the Cr-atoms is $S = 3/2$.

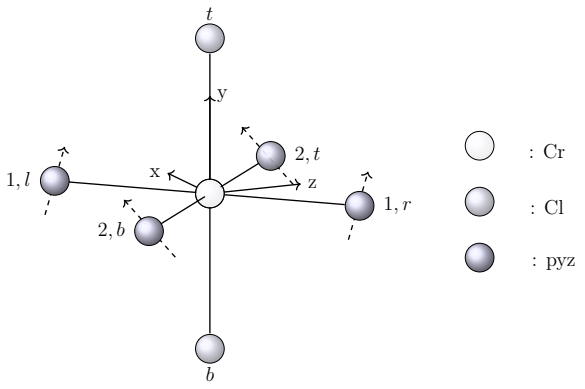

Fig. 6.4: Illustration of the model complex $CrCl_2(pyz)_4$. The nomenclature of the six relevant atoms, the coordinate system in use and the orientation of the pyrazine rings is illustrated.

As seen from **Fig. 6.1** two neighbouring chromium atoms couple through a pyrazine ring. A pyrazine ring is much like a benzene ring except for the fact that two of the carbon atoms have been replaced with nitrogen atoms. Nitrogen atoms possess one extra electron compared to carbon atoms, which results in two less hydrogen atoms on each ring. Instead there is a lone-pair electron on the nitrogen atoms. A benzene ring has four energy levels of which two are two-fold degenerate. Replacing two carbon atoms with nitrogen atoms lifts this degeneracy, due to the decrease in symmetry; a pyrazine ring thus has 6 non-degenerate energy levels. The d-orbitals on the chromium atoms mainly couple to the p_z orbitals of the atoms of the pyrazine ring. For simplicity only these orbitals will be included. The eigenstates of the six energy levels of the pyrazine ring are then approximated as either even or odd linear combinations of p_z-orbitals with different amplitudes on each one of the six sites in the pyrazine ring. Since the interaction between the chromium atom and the atoms in the pyrazine rings decreases with increasing distance, the ring is approximated to be a single site. Therefore, only the two linear combinations with the greatest amplitudes on the nitrogen atoms are included and the rest is neglected. Thus, the pyrazine rings are approximated as a single "atom" on which p_z-orbitals with two different amplitudes, α_2 and α_4, are located, where the latter is even and the former is odd. Lastly, the pyrazine rings are rotated compared to

the Cl-Cr-Cl axis, see **Fig. 6.1 c**. Pedersen et al. measure these rotation angles to be 42.5° and 43.9° with respect to the crystallographic c direction for the pyrazine ring 1 and 2, respectively. This will be approximated as 45° in both cases. This means that the $p_{z'}$-orbitals of the pyrazine "atoms" are instead linear combinations of both p_x, p_y and p_z orbitals with respect to the global coordinate system, see **Fig. 6.4**. Thus, z' refer to the local coordinate system of the pyrazine sites, i.e., the direction perpendicular to the rings.

As in previous sections the full Hamiltonian for a single molecule can be written in terms of the Slater Koster elements. The full Hamiltonian is written in the basis

$$\begin{aligned}|\Psi\rangle = \{&|d_{xy}\rangle, |d_{yz}\rangle, |d_{zx}\rangle, |d_{x^2-y^2}\rangle, |d_{z^2}\rangle, |p_x^t\rangle, |p_y^t\rangle, |p_z^t\rangle, |p_x^b\rangle, |p_y^b\rangle, |p_z^b\rangle,\\ &|p_{z'}^{1,r}(\alpha_2)\rangle, |p_{z'}^{1,r}(\alpha_4)\rangle, |p_{z'}^{2,t}(\alpha_2)\rangle, |p_{z'}^{2,t}(\alpha_4)\rangle,\\ &|p_{z'}^{1,l}(\alpha_2)\rangle, |p_{z'}^{1,l}(\alpha_4)\rangle, |p_{z'}^{2,b}(\alpha_2)\rangle, |p_{z'}^{2,b}(\alpha_4)\rangle\},\end{aligned} \tag{6.2}$$

where the first five elements refer to the d-orbitals of the chromium atom followed by the three p-orbitals of both chlorine atoms (top and bottom), and lastly the $p_{z'}$-orbitals for the four pyrazine-"atoms". As in **section 5.2.1** the full Hamiltonian can be projected into the subspace of the d-orbitals and an analytical expression for the 5x5 matrix $V_{pd}^{\dagger}V_{pd}$ can be obtained. To make the matrix block diagonal, this is written in the basis $\{d_{yz}, d_{zx}, d_{xy}, d_{x^2-y^2}, d_{z^2}\}$,

$$H_d = \begin{bmatrix} M_{11} & M_{12} & 0 & 0 & 0 \\ M_{12} & M_{22} & 0 & 0 & 0 \\ 0 & 0 & M_{11} & M_{34} & M_{35} \\ 0 & 0 & M_{34} & M_{44} & M_{45} \\ 0 & 0 & M_{35} & M_{45} & M_{55} \end{bmatrix}, \tag{6.3}$$

with

$$M_{11} = \frac{1}{2}|V_{pd\pi}|^2(4+\alpha), \tag{6.4}$$

$$M_{12} = -\frac{\sqrt{3}}{2}V_{pd\sigma}V_{pd\pi}^{\dagger}\alpha, \tag{6.5}$$

$$M_{22} = \frac{3}{2}|V_{pd\sigma}|^2\alpha, \tag{6.6}$$

$$M_{34} = \frac{1}{4}V_{pd\pi}^{\dagger}\alpha\left(\sqrt{2}V_{pd\pi} - \sqrt{3}V_{pd\sigma}\right), \tag{6.7}$$

$$M_{35} = -\frac{1}{4}V_{pd\pi}^{\dagger}\alpha\left(\sqrt{6}V_{pd\pi} + V_{pd\sigma}\right), \tag{6.8}$$

$$M_{45} = \frac{1}{8}\left[4\sqrt{3}|V_{pd\sigma}|^2 - \alpha\left(2\sqrt{3}V_{pd\pi} + \sqrt{2}V_{pd\sigma}\right)\left(V_{pd\pi}^{\dagger} - \sqrt{\frac{3}{2}}V_{pd\sigma}^{\dagger}\right)\right], \tag{6.9}$$

$$M_{44} = \frac{1}{8}\left[12\sqrt{3}|V_{pd\sigma}|^2 + \alpha\left(2V_{pd\pi} - \sqrt{6}V_{pd\sigma}\right)\left(V_{pd\pi}^{\dagger} - \sqrt{\frac{3}{2}}V_{pd\sigma}^{\dagger}\right)\right], \tag{6.10}$$

$$M_{55} = \frac{1}{8}\left[4|V_{pd\sigma}|^2 + \alpha\left(V_{pd\pi}^{\dagger}\left(6V_{pd\pi} + \sqrt{6}V_{pd\sigma}\right) + V_{pd\sigma}^{\dagger}(V_{pd\sigma} + \sqrt{6}V_{pd\pi})\right)\right], \tag{6.11}$$

where $\alpha = |\alpha_2|^2 + |\alpha_4|^2$ has been defined. The two blocks in Eq. (6.3) are trivial to diagonalize. It is evident from Eq. (6.3) that the d_{yz} orbital only couples to the d_{zx} orbital, and further that d_{xy}, $d_{x^2-y^2}$ and d_{z^2} only couple to each other. To understand this, the symmetries of the molecule are investigated.

The fact that the pyrazine rings are rotated decreases the symmetry of the molecule. As always the group describing the symmetry of $CrCl_2(pyz)_4$ includes identity. In addition to this only three more operations leave the molecule invariant, namely inversion (i), a rotation of π around the z-axis ($C_2(z)$), and a reflection in the plane spanned by the x- and y-axis (σ_h), see **Fig. 6.4**. These four symmetry-operations form the point group $\mathbf{C_{2h}}$. This group is abelian and thus both the order of the group and the number of irreducible representations are equal to four. The character table can now be constructed using the rules listed in the bottom of **section 2.0.2**, see **Table 6.1**.

$\mathbf{C_{2h}}$	E	$C_2(z)$	i	σ_h	Quadratic Functions
A_g	1	1	1	1	x^2, y^2, z^2, xy
B_g	1	-1	1	-1	yz, zx
A_u	1	1	-1	-1	–
B_u	1	-1	-1	1	–

Table 6.1: Character table of the C_{2h} group [38].

From this character table it is observed that yz and zx belong to the same representation and similarly for the rest of the d-orbitals. This explains the block diagonal form of Eq. (6.3). Further, we see from this equation that $\langle xy|\hat{\mathcal{H}}|xy\rangle = \langle yz|\hat{\mathcal{H}}|yz\rangle$, which has to do with the symmetry of the object and the chosen coordinate system.

6.4 Monolayer $CrCl_2(pyz)_2$

6.4.1 Tight Binding Model

Monolayer chromium-chloride-pyrazine, see **Fig. 6.5** (a), is now investigated. Using the Rietveld refinement technique[6], Pedersen et al. [4] have found the three lattice constants to be $a = 6.90351(4)$ Å, $b = 6.97713(4)$ Å, and $c = 10.82548(6)$ Å. The proximity of a and b motives the lattice to be approximated as a square lattice in the Cr-pyz plane. The relevant symmetry-points are thus approximated to be

$$\mathbf{\Gamma} = (0,0,0), \quad \mathbf{M} = \left(0, 0, \frac{1}{\sqrt{2}}\right), \quad \mathbf{X} = \left(-\frac{1}{2\sqrt{2}}, 0, \frac{1}{2\sqrt{2}}\right). \tag{6.12}$$

[6]Rietvild refinement is a technique used to characterize crystalline structures developed by Hugo Rietveld. Neutron and x-ray diffraction of powder yields a pattern characterized by reflections at specific positions. Using a non-linear least square method, the Rietveld method then fits theoretical predictions to the experimental data to determine various charactistics of the structure [39].

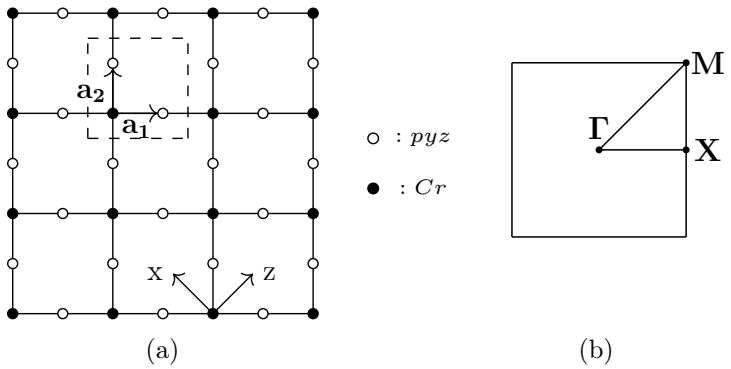

Fig. 6.5: (a) Monolayer $CrCl_2(pyz)_2$ viewed along the Cl-Cr-Cl axis. The chromium and pyrazine sites are illustrated with black and white cirles, respectively. Further, the unit cell is marked with a dashed square and the relevant lattice vectors and the used coordinate system is indicated. The last lattice vector, $\mathbf{a}_3$, not indicated, points from Cr to the top Cl. (b) The symmetry-points used in the calculations of the band structure marked on an illustration of the approximated square Brillouin zone.

These symmetry points are indicated on the Brillouin zone illustrated in **Fig. 6.5** (b).

A unit cell includes one chromium atom, two chlorine atoms and two pyrazine rings, which will be labeled 1 and 2. Assuming that the two pyrazine rings have the same onsite energy, and similarly for the chlorine and chromium atoms, a tight binding Hamiltonian for this system in real-space, including only nearest neighbour interactions between p- and d-orbitals, can be written as

$$\begin{aligned}\hat{\mathcal{H}} =&\xi^{Cr}\sum_{\mathbf{r}_i}\sum_{\mu=1}^{5}\hat{d}^{\dagger}_{i,\mu}\hat{d}_{i,\mu}+\xi^{Cl}\sum_{\mathbf{r}_i}\sum_{\nu=1}^{3}\left[(\hat{p}^{t}_{i,\nu})^{\dagger}\hat{p}^{t}_{i,\nu}+(\hat{p}^{b}_{i,\nu})^{\dagger}\hat{p}^{b}_{i,\nu}\right]\\
&+\xi^{pyz}\sum_{\mathbf{r}_i}\left[(\hat{p}^{1}_{i,z'})^{\dagger}\hat{p}^{1}_{i,z'}+(\hat{p}^{2}_{i,z'})^{\dagger}\hat{p}^{2}_{i,z'}\right]\\
&+\frac{1}{2}\sum_{\mathbf{r}_i}\sum_{\mathbf{r}_{j_\pm}=\mathbf{r}_i\pm\mathbf{a}_1}\sum_{\mu=1}^{5}\left[t^{1,r}_{\mu,z'}\hat{d}^{\dagger}_{i,\mu}\hat{p}^{1}_{j_+,z'}+t^{1,l}_{\mu,z'}\hat{d}^{\dagger}_{i,\mu}\hat{p}^{1}_{j_-,z'}+h.c.\right]\\
&+\frac{1}{2}\sum_{\mathbf{r}_i}\sum_{\mathbf{r}_{j_\pm}=\mathbf{r}_i\pm\mathbf{a}_2}\sum_{\mu=1}^{5}\left[t^{2,t}_{\mu,z'}\hat{d}^{\dagger}_{i,\mu}\hat{p}^{2}_{j_+,z'}+t^{2,b}_{\mu,z'}\hat{d}^{\dagger}_{i,\mu}\hat{p}^{2}_{j_-,z'}+h.c.\right]\\
&+\sum_{\mathbf{r}_i}\sum_{\mathbf{r}_{j_\pm}=\mathbf{r}_i\pm\mathbf{a}_3}\sum_{\mu=1}^{5}\sum_{\nu=1}^{3}\left[t^{t}_{\mu,\nu}\hat{d}^{\dagger}_{i,\mu}\hat{p}^{t}_{j_+,\nu}+t^{b}_{\mu,\nu}\hat{d}^{\dagger}_{i,\mu}\hat{p}^{b}_{j_-,\nu}+h.c.\right].\end{aligned}\tag{6.13}$$

Here $\hat{d}^{\dagger}_{i,\mu}$ ($\hat{d}_{i,\mu}$) creates (annihilates) an electron on the chromium site at $\mathbf{r}_i$ in unit cell i and orbital μ. Similarly, the operator $(\hat{p}^{t,b}_{j,\nu})^{\dagger}$ and $\hat{p}^{t,b}_{j,\nu}$ creates and annihilates an electron in the orbital ν at the chlorine atom at site $\mathbf{r}_i \pm \mathbf{a}_3$, respectively. Lastly, the operators $(\hat{p}^{1(2)}_{j,z'})^{\dagger}$ and $\hat{p}^{1(2)}_{j,z'}$ creates and annihilates an electron in a $p_{z'}$ orbital on the pyrazine site 1 (2) at $\mathbf{r}_i + \mathbf{a}_1$ ($\mathbf{r}_i + \mathbf{a}_2$), respectively.

The three first terms of the Hamiltonian states the onsite energies of the d- and p-orbitals of the five atoms in the unit cell. Further, the Hamiltonian consists of six terms where an electron can hop from a p-orbital to any nearest neighbor d-orbital. The Hermitian conjugate of these terms includes hopping from a d-orbital to any nearest neighbour p-orbital. The factor 1/2 is included on eight of these terms to prevent double counting. For simplicity the spin indices are omitted. The following onsite energies and hopping matrices have been defined

$$\xi^{Cr} = \langle \mathbf{r}_i; d_\mu | \hat{\mathcal{H}}_t | \mathbf{r}_i; d_\mu \rangle, \tag{6.14}$$
$$\xi^{Cl} = \langle \mathbf{r}_i \pm \mathbf{a}_3; p_\nu | \hat{\mathcal{H}}_t | \mathbf{r}_i \pm \mathbf{a}_3; p_\nu \rangle, \tag{6.15}$$
$$\xi^{pyz} = \langle \mathbf{r}_i \pm \mathbf{a}_1; p_{z'} | \hat{\mathcal{H}}_t | \mathbf{r}_i \pm \mathbf{a}_1; p_{z'} \rangle = \langle \mathbf{r}_i \pm \mathbf{a}_2; p_{z'} | \hat{\mathcal{H}}_t | \mathbf{r}_i \pm \mathbf{a}_2; p_{z'} \rangle, \tag{6.16}$$
$$t^t_{\mu\nu} = \langle \mathbf{r}_i; d_\mu | \hat{\mathcal{H}}_t | \mathbf{r}_i + \mathbf{a}_3; p_\nu \rangle, \tag{6.17}$$
$$t^b_{\mu\nu} = \langle \mathbf{r}_i; d_\mu | \hat{\mathcal{H}}_t | \mathbf{r}_i - \mathbf{a}_3; p_\nu \rangle, \tag{6.18}$$
$$t^{1,r}_{\mu z'} = \langle \mathbf{r}_i; d_\mu | \hat{\mathcal{H}}_t | \mathbf{r}_i + \mathbf{a}_1; p_{z'} \rangle, \tag{6.19}$$
$$t^{1,l}_{\mu z'} = \langle \mathbf{r}_i; d_\mu | \hat{\mathcal{H}}_t | \mathbf{r}_i - \mathbf{a}_1; p_{z'} \rangle, \tag{6.20}$$
$$t^{2,t}_{\mu z'} = \langle \mathbf{r}_i; d_\mu | \hat{\mathcal{H}}_t | \mathbf{r}_i + \mathbf{a}_2; p_{z'} \rangle, \tag{6.21}$$
$$t^{2,b}_{\mu z'} = \langle \mathbf{r}_i; d_\mu | \hat{\mathcal{H}}_t | \mathbf{r}_i - \mathbf{a}_2; p_{z'} \rangle. \tag{6.22}$$

$\hat{\mathcal{H}}_t$ includes hopping between the two relevant orbitals, see Eq. (5.1). The numerical values for these can be obtained using the Slater Koster decomposition. $t^t_{\mu\nu}$ and $t^b_{\mu\nu}$ are 3x5 matrices that consists of the Slater Koster matrix elements stated in **section 5.2**. The hopping matrices for the pyrazine rings are 2x5 matrices that include both the even and odd wavefunction for the pyrazine rings as described in the **section 6.3**. These matrices thus have the form

$$t^{1,r}_{\mu z'} = \begin{bmatrix} \alpha_2 E_{z',xy} & \alpha_2 E_{z',yz} & \alpha_2 E_{z',zx} & \alpha_2 E_{z',x^2-y^2} & \alpha_2 E_{z',z^2} \\ \alpha_4 E_{z',xy} & \alpha_4 E_{z',yz} & \alpha_4 E_{z',zx} & \alpha_4 E_{z',x^2-y^2} & \alpha_4 E_{z',z^2} \end{bmatrix}, \tag{6.23}$$
$$t^{1,l}_{\mu z'} = \begin{bmatrix} -\alpha_2 E_{z',xy} & -\alpha_2 E_{z',yz} & -\alpha_2 E_{z',zx} & -\alpha_2 E_{z',x^2-y^2} & -\alpha_2 E_{z',z^2} \\ \alpha_4 E_{z',xy} & \alpha_4 E_{z',yz} & \alpha_4 E_{z',zx} & \alpha_4 E_{z',x^2-y^2} & \alpha_4 E_{z',z^2}. \end{bmatrix} \tag{6.24}$$

These Slater Koster elements in the global coordinate system for d-orbital μ is given by

$$E_{z',\mu} = \left[\frac{1}{4} \left(\sqrt{2} - 2 \right) E_{x,\mu} + 2E_{y,\mu} + \left(2 + \sqrt{2} \right) E_{z,\mu} \right]. \tag{6.25}$$

The bonding matrices $t^{2,t}_{\mu z'}$ and $t^{2,b}_{\mu z'}$ are of similar form.

The Hamiltonian can now be Fourier transformed to give

$$\begin{aligned}\hat{\mathcal{H}} = \sum_{\mathbf{k}} \Bigg\{ & \xi^{Cr} \sum_{\mu=1}^{5} \hat{d}^{\dagger}_{\mathbf{k},\mu} \hat{d}_{\mathbf{k},\mu} + \xi^{Cl} \sum_{\nu=1}^{3} \left[(\hat{p}^{t}_{\mathbf{k},\nu})^{\dagger} \hat{p}^{t}_{\mathbf{k},\nu} + (\hat{p}^{b}_{\mathbf{k},\nu})^{\dagger} \hat{p}^{b}_{\mathbf{k},\nu} \right] \\ & + \xi^{pyz} \left[(\hat{p}^{1}_{\mathbf{k},z'})^{\dagger} \hat{p}^{1}_{\mathbf{k},z'} + (\hat{p}^{2}_{\mathbf{k},z'})^{\dagger} \hat{p}^{2}_{\mathbf{k},z'} \right] \\ & + \sum_{\mu=1}^{5} \left[\hat{d}^{\dagger}_{\mathbf{k},\mu} \hat{p}^{1}_{\mathbf{k},z'} \left(t^{1,r}_{\mu,z'} e^{i\mathbf{k}\cdot\mathbf{a}_1} + t^{1,l}_{\mu,z'} e^{-i\mathbf{k}\cdot\mathbf{a}_1} \right) + h.c. \right] \\ & + \sum_{\mu=1}^{5} \left[\hat{d}^{\dagger}_{\mathbf{k},\mu} \hat{p}^{2}_{\mathbf{k},z'} \left(t^{2,t}_{\mu,z'} e^{i\mathbf{k}\cdot\mathbf{a}_2} + t^{2,b}_{\mu,z'} e^{-i\mathbf{k}\cdot\mathbf{a}_2} \right) + h.c. \right] \\ & + \sum_{\mu=1}^{5} \sum_{\nu=1}^{3} \left[t^{t}_{\mu,\nu} \hat{d}^{\dagger}_{\mathbf{k},\mu} \hat{p}^{t}_{\mathbf{k},\nu} e^{i\mathbf{k}\cdot\mathbf{a}_3} + t^{b}_{\mu,\nu} \hat{d}^{\dagger}_{\mathbf{k},\mu} \hat{p}^{b}_{\mathbf{k},\nu} e^{-i\mathbf{k}\cdot\mathbf{a}_3} + h.c. \right] \Bigg\}. \end{aligned} \tag{6.26}$$

The eigenenergies of this Hamiltonian can be found numerically for the path $\mathbf{M} \rightarrow \mathbf{\Gamma} \rightarrow \mathbf{X}$ in reciprocal space to obtain the band structure in **Fig. 6.6**. The following values have been used to obtain these energy bands, $\xi^{Cl} = -7.048$ eV, $\xi^{Cr} = -0.856$ eV, $\xi^{pyz} = -2.944$ eV, $V_{pd\sigma} = 4.8$ eV, $V_{pd\pi} = -1.344$ eV, $\alpha_2 = 0.428$, $\alpha_4 = 0.932$. This is viewed alongside the band structure of $CrCl_2(pyz)_2$ both for a ferrimagnetic and antiferromagnetic state obtained from DFT calculations performed by Pedersen et al. [4]. The bands obtained here have been shifted in energy to be comparable with the band structures collected from Pedersen et al. [4]. The Fermi Level is located at 0 eV. Remember that these groundstates both exhibit antiferromagnetic interactions between the chromium ions and the pyrazine ligands within the layers, but the orientation of the $CrCl_2(pyz)_2$ layer magnetic moments are parallel or antiparallel, respectively. Note that the DFT calculated band structures are thus for bulk $CrCl_2(pyz)_2$ whereas the band structures obtained using tight binding are for monolayer $CrCl_2(pyz)_2$.

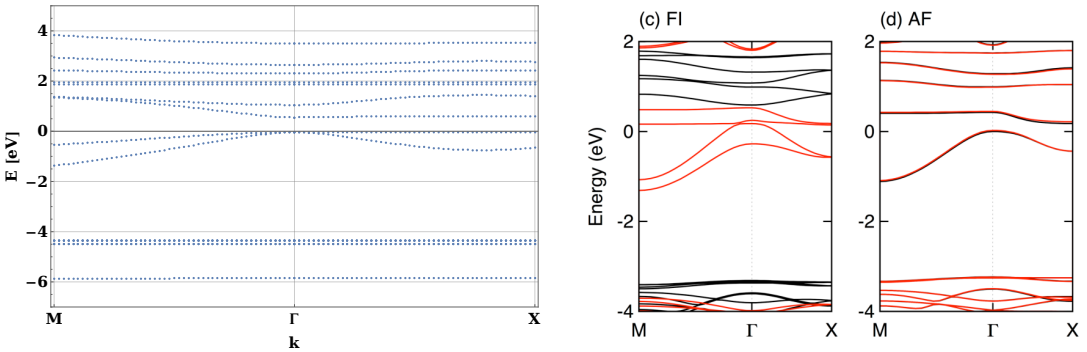

(a) (b)

Fig. 6.6: (a) Band structure of monolayer $CrCl_2(pyz)_2$ obtained from the tight binding Hamiltonian viewed in Eq. (6.26) along the path $\mathbf{M} \rightarrow \mathbf{\Gamma} \rightarrow \mathbf{X}$. (b) Band structure obtained from DFT calculations [4] both for a ferromagnetic (c) and an antiferromagnetic (d) spin configuration. Black (red) bands correspond to spin up (down).

The d-bands are mainly located above 1.5 eV, which is clearly seen from the PDOS plot obtained from DFT [4], see **Fig. 6.7**. This is consistent with the results from investigating the eigenvectors of the bands obtained in this section. These d-bands are quite flat, which means that the d-electrons are localized at their sites. Pedersen et al. suggests that this could indicate a strong π-d hybridization. Looking at the band structures obtained from DFT, clearly the ferrimagnetic state has a metallic band structure whereas the antiferromagnetic state is insulating. This can also be seen from the PDOS plots. This contradicts the experimental results, which show that the observed ferrimagnetic state exhibit an insulating behaviour, see **Fig. 6.2 c**. This discrepency is suggested by Pedersen et al. to be due to the fact that DFT does not include the structural disorder of the pyrazine ligands. The band structures obtained in this thesis agrees with the experimental results of an insulating, ferrimagnetic groundstate, described in **section 6.2**.

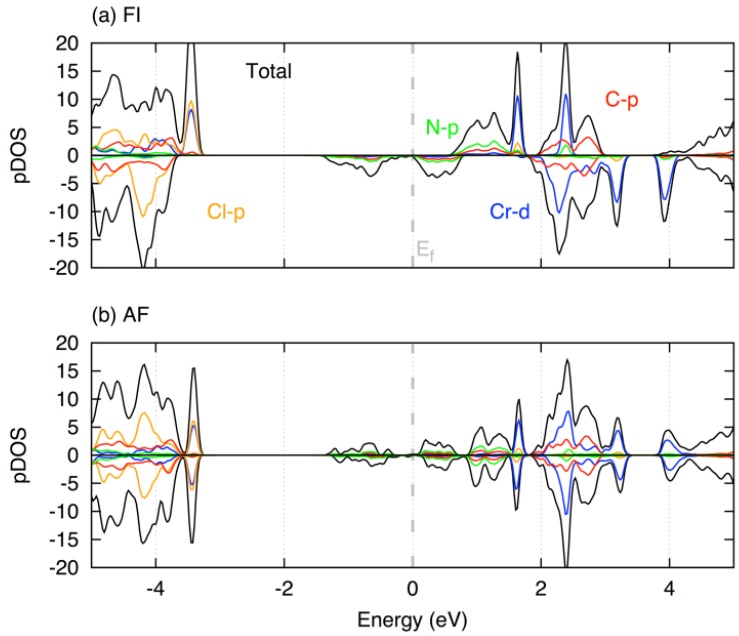

Fig. 6.7: The PDOS obtained from DFT calculations by Pedersen et al. [4] for a ferrimagnetic groundstate (a) and an antiferromagnetic groundstate (b).

6.4.2 Simple Model of Two Unit Cells of $CrCl_2(pyz)_2$

In the search of a better understanding of $CrCl_2(pyz)_2$ the simple model illustrated in **Fig. 6.8** is investigated. This is not identical to two unit cells of a single layer of $CrCl_2(pyz)_2$ since it contains fewer pyrazine sites. Further, they are moved with respect to the two chromium atoms. It does contain the battle between kinetic energy and exchange energy. This toy model is developed in the pursuit of a simple model to explain the behaviour of the relevant spins in $CrCl_2(pyz)_2$. In this model the two chromium atoms are viewed as localized spins with length $S = 3/2$. Further, it includes

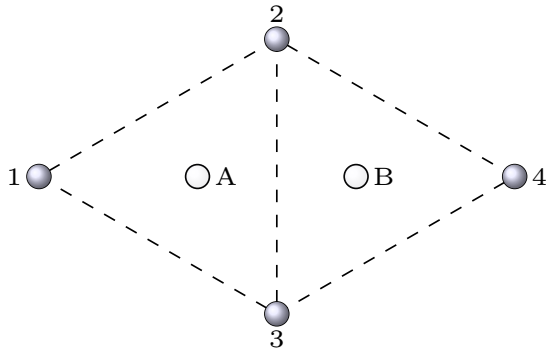

Fig. 6.8: Simple model containing two chromium sites (light circles) and four pyrazine sites (dark circles). Each Chroimium spin only couples to three out of the four pyrazine sites.

two electrons that can delocalize over the four pyrazine sites. The chlorine sites are neglected in this model, except for the fact that they have reduced the number of electrons on the chromium sites. In this model the exchange coupling between the chromium spins and the spin of the two electrons on the pyrazine sites is included. Further, the electrons on the pyrazine sites are able to hop between the pyrazine sites, indicated with dashed lines in **Fig. 6.8**. Lastly, a cost due to Coulomb repulsion, U, is included if these two electrons are located at the same site. The full Hamiltonian is thus written as

$$\begin{aligned}\hat{\mathcal{H}} =& -2J\hat{\mathbf{S}}_A \cdot \left(\hat{\mathbf{S}}_1 + \hat{\mathbf{S}}_2 + \hat{\mathbf{S}}_3\right) - 2J\hat{\mathbf{S}}_B \cdot \left(\hat{\mathbf{S}}_2 + \hat{\mathbf{S}}_3 + \hat{\mathbf{S}}_4\right) \\ & - t\sum_{\sigma=\uparrow,\downarrow}\left(\hat{c}^\dagger_{1\sigma}\hat{c}_{2\sigma} + \hat{c}^\dagger_{2\sigma}\hat{c}_{3\sigma} + \hat{c}^\dagger_{1\sigma}\hat{c}_{3\sigma} + \hat{c}^\dagger_{2\sigma}\hat{c}_{4\sigma} + \hat{c}^\dagger_{3\sigma}\hat{c}_{4\sigma} + h.c.\right) \\ & + U\sum_{i=1}^{4}\sum_{\sigma,\sigma'=\uparrow,\downarrow}\hat{c}^\dagger_{i\sigma'}\hat{c}^\dagger_{i\sigma}\hat{c}_{i\sigma}\hat{c}_{i\sigma'},\end{aligned} \tag{6.27}$$

where $\hat{\mathbf{S}}_A$ and $\hat{\mathbf{S}}_B$ represent the spin of the two chromium atoms, and $\hat{\mathbf{S}}_i$ with $i = 1, 2, 3, 4$ represent the spin of the four pyrazine sites. $\hat{c}^\dagger_i$ and $\hat{c}_i$ is the creation and annihilation operator of an electron on site i, respectively. J is the exchange integral, t the hopping constant, and U is the strength of the Coulomb repulsion of two electrons occupying the same site. The $-2J$ convention is adopted here to comply with the methods in [4].

The spins of each chromium ion can take four S_z values, i.e., $|-3/2\rangle$, $|-1/2\rangle$, $|1/2\rangle$ and $|3/2\rangle$. The basis for the two electrons on the pyrazine sites will be written in terms of the singlet and triplet states. For this purpose a new notation is introduced. A singlet state with $S_z = 0$ will be represented by a line as illustrated in the following examples:

$$|-00\rangle = \frac{1}{\sqrt{2}}\left(|\uparrow\downarrow 00\rangle - |\downarrow\uparrow 00\rangle\right), \tag{6.28}$$

$$|\overset{\frown}{0\,0}\rangle = \frac{1}{\sqrt{2}}\left(|\uparrow 0\downarrow 0\rangle - |\downarrow 0\uparrow 0\rangle\right), \tag{6.29}$$

$$|-000\rangle = \frac{1}{\sqrt{2}}\left(|\uparrow\downarrow 000\rangle - |\downarrow\uparrow 000\rangle\right). \tag{6.30}$$

The first state is a singlet state between an electron on site 1 and an electron on site 2, the second between an electron on site 1 and one on site 3, and the last is a singlet state of two electrons both occupying site 1. A triplet state with $S_z = 0$ is represented by an arrow as

$$|\rightarrow 00\rangle = \frac{1}{\sqrt{2}}\left(|\uparrow\downarrow 00\rangle + |\downarrow\uparrow 00\rangle\right), \tag{6.31}$$

$$|\overset{\frown}{0\searrow}0\rangle = \frac{1}{\sqrt{2}}\left(|\uparrow 0\downarrow 0\rangle + |\downarrow 0\uparrow 0\rangle\right). \tag{6.32}$$

Due to the Pauli principle, the state in Eq. (6.30) is not a possible triplet state. The triplet states are represented by an arrow since the positive sign in the superposition means that $\hat{c}^\dagger_{1\uparrow}\hat{c}^\dagger_{2\downarrow} + \hat{c}^\dagger_{1\downarrow}\hat{c}^\dagger_{2\uparrow} = -\left(\hat{c}^\dagger_{2\uparrow}\hat{c}^\dagger_{1\downarrow} + \hat{c}^\dagger_{2\downarrow}\hat{c}^\dagger_{1\uparrow}\right)$ contrary to the singlet states where these two states would be identical. All triplet states are defined such that the creation operator to the left creates an electron on a site denominated with a lower numerical value compared to the creation operator to the right. Similarly, for the triplet states with $S_z = 1$ and $S_z = -1$. The basis for the two electrons are thus

$$\begin{aligned}|\psi\rangle = \Big\{&|-00\rangle, |0-0\rangle, |00-\rangle, |\overset{\frown}{0\,0}\rangle, |0\overset{\frown}{0\,}\rangle, |\overset{\frown}{00}\rangle,\\ &|-000\rangle, |0-00\rangle, |00-0\rangle, |000-\rangle,\\ &|\downarrow\downarrow 00\rangle, |0\downarrow\downarrow 0\rangle, |00\downarrow\downarrow\rangle, |\downarrow 0\downarrow 0\rangle, |0\downarrow 0\downarrow\rangle, |\downarrow 00\downarrow\rangle,\\ &|\rightarrow 00\rangle, |0\rightarrow 0\rangle, |00\rightarrow\rangle, |\overset{\frown}{0\searrow}0\rangle, |0\overset{\frown}{0\searrow}\rangle, |\overset{\frown}{00\searrow}\rangle,\\ &|\uparrow\uparrow 00\rangle, |0\uparrow\uparrow 0\rangle, |00\uparrow\uparrow\rangle, |\uparrow 0\uparrow 0\rangle, |0\uparrow 0\uparrow\rangle, |\uparrow 00\uparrow\rangle\Big\}.\end{aligned} \tag{6.33}$$

The full state is then given by $|ms_A\rangle \otimes |ms_B\rangle \otimes |\psi\rangle$, where $|ms_A\rangle$ and $|ms_B\rangle$ is the z-component of the A and B chromium spins, respectively. The Hilbert space is thus 448 dimensional. For this reason the Hamiltonian is diagonalized numerically. To be able to accomplish this, the Hamiltonian is first rewritten, using that $\hat{\mathbf{S}}_1 \cdot \hat{\mathbf{S}}_2 = \hat{S}^z_1\hat{S}^z_2 + \frac{1}{2}\left(S^+_1 S^-_2 + S^-_1 S^+_2\right)$, such that

$$\begin{aligned}\hat{\mathcal{H}} =& -2J\hat{S}^z_A\left(\hat{S}^z_1 + \hat{S}^z_2 + \hat{S}^z_3\right) - J\hat{S}^+_A\left(\hat{S}^-_1 + \hat{S}^-_2 + \hat{S}^-_3\right) - J\hat{S}^-_A\left(\hat{S}^+_1 + \hat{S}^+_2 + \hat{S}^+_3\right)\\ &-2J\hat{S}^z_B\left(\hat{S}^z_2 + \hat{S}^z_3 + \hat{S}^z_4\right) - J\hat{S}^+_B\left(\hat{S}^-_2 + \hat{S}^-_3 + \hat{S}^-_4\right) - J\hat{S}^-_B\left(\hat{S}^+_2 + \hat{S}^+_3 + \hat{S}^+_4\right)\\ &-t\sum_{\sigma=\uparrow,\downarrow}\left(\hat{c}^\dagger_{1\sigma}\hat{c}_{2\sigma} + \hat{c}^\dagger_{2\sigma}\hat{c}_{3\sigma} + \hat{c}^\dagger_{1\sigma}\hat{c}_{3\sigma} + \hat{c}^\dagger_{2\sigma}\hat{c}_{4\sigma} + \hat{c}^\dagger_{3\sigma}\hat{c}_{4\sigma} + h.c.\right)\\ &+U\sum_{i=1}^{4}\sum_{\sigma,\sigma'=\uparrow,\downarrow}\hat{c}^\dagger_{i\sigma'}\hat{c}^\dagger_{i\sigma}\hat{c}_{i\sigma}\hat{c}_{i\sigma'}.\end{aligned} \tag{6.34}$$

To begin with, we focus on the first three exchange terms including $\hat{S}^z_A$. The chromium part of this is trivial to write in matrix form, in the basis $\{|-3/2\rangle, |-1/2\rangle, |1/2\rangle, |3/2\rangle\}$,

as

$$\mathbf{S}^z_{Cr} = \begin{bmatrix} -\frac{3}{2} & 0 & 0 & 0 \\ 0 & -\frac{1}{2} & 0 & 0 \\ 0 & 0 & \frac{1}{2} & 0 \\ 0 & 0 & 0 & \frac{3}{2} \end{bmatrix}. \tag{6.35}$$

Now, let us see how this affects the basis states for the electrons on the pyrazine sites. Applying this operator on basis states where neither of the two electrons are located on site 4 results in the expected $S_z = 0$ for a singlet state, e.g.,

$$\left(\hat{S}^z_1 + \hat{S}^z_2 + \hat{S}^z_3\right) |-00\rangle = \frac{1}{\sqrt{2}} \left(\frac{1}{2}|\uparrow\downarrow 00\rangle - \frac{1}{2}|\uparrow\downarrow 00\rangle - \frac{1}{2}|\downarrow\uparrow 00\rangle + \frac{1}{2}|\downarrow\uparrow 00\rangle\right) = 0. \tag{6.36}$$

Similarly, for triplet states with $S_z = 0$ with no electrons occupying site 4 and for singlet states where both electrons occupy the same site. On the other hand, when one of the electrons is occupying site 4, singlet and triplet states are coupling, as in the following example

$$\left(\hat{S}^z_1 + \hat{S}^z_2 + \hat{S}^z_3\right) |00-\rangle = \frac{1}{\sqrt{2}} \left[\frac{1}{2}|00\uparrow\downarrow\rangle - \left(-\frac{1}{2}|00\downarrow\uparrow\rangle\right)\right] = \frac{1}{2}|00\rightarrow\rangle. \tag{6.37}$$

The triplet states with $S_z = 1$ or $S_z = -1$ are eigenstates to this operator, though the eigenvalue depends on whether one of the electrons is occupying site 4 or not, as seen in the following examples:

$$\left(\hat{S}^z_1 + \hat{S}^z_2 + \hat{S}^z_3\right) |0\downarrow\downarrow 0\rangle = -|0\downarrow\downarrow 0\rangle, \tag{6.38}$$

$$\left(\hat{S}^z_1 + \hat{S}^z_2 + \hat{S}^z_3\right) |00\downarrow\downarrow\rangle = -\frac{1}{2}|00\downarrow\downarrow\rangle, \tag{6.39}$$

$$\left(\hat{S}^z_1 + \hat{S}^z_2 + \hat{S}^z_3\right) |0\uparrow\uparrow 0\rangle = |0\uparrow\uparrow 0\rangle, \tag{6.40}$$

$$\left(\hat{S}^z_1 + \hat{S}^z_2 + \hat{S}^z_3\right) |00\uparrow\uparrow\rangle = \frac{1}{2}|00\uparrow\uparrow\rangle. \tag{6.41}$$

This procedure is similar for the S^z_B part of the Hamiltonian, though in this case, singlet and triplet states with $S_z = 0$ are coupled when one of the electrons occupy site 1.

Now, let us look at the last two parts of the first line of Eq. (6.34). The raising and lowering operators for the chromium spins can be written as

$$\mathbf{S}^+_{Cr} = \begin{bmatrix} 0 & 0 & 0 & 0 \\ \sqrt{3} & 0 & 0 & 0 \\ 0 & 2 & 0 & 0 \\ 0 & 0 & \sqrt{3} & 0 \end{bmatrix} \quad \text{and} \quad \mathbf{S}^-_{Cr} = \begin{bmatrix} 0 & \sqrt{3} & 0 & 0 \\ 0 & 0 & 2 & 0 \\ 0 & 0 & 0 & \sqrt{3} \\ 0 & 0 & 0 & 0 \end{bmatrix}. \tag{6.42}$$

For the electrons on the pyrazine sites it is not as simple. As before, the outcome depends on whether one of the electrons is occupying site 4 or not.

Focusing on the electron part including raising operators for the pyrazine electrons, a few cases will be shown to illustrate how the basis states are affected by these operators,

$$\left(\hat{S}_1^+ + \hat{S}_2^+ + \hat{S}_3^+\right)|-00\rangle = 0, \tag{6.43}$$

$$\left(\hat{S}_1^+ + \hat{S}_2^+ + \hat{S}_3^+\right)|00-\rangle = -\frac{1}{\sqrt{2}}|00\uparrow\uparrow\rangle, \tag{6.44}$$

$$\left(\hat{S}_1^+ + \hat{S}_2^+ + \hat{S}_3^+\right)|\rightarrow 00\rangle = \sqrt{2}|\uparrow\uparrow 00\rangle, \tag{6.45}$$

$$\left(\hat{S}_1^+ + \hat{S}_2^+ + \hat{S}_3^+\right)|00\rightarrow\rangle = \frac{1}{\sqrt{2}}|00\uparrow\uparrow\rangle, \tag{6.46}$$

$$\begin{aligned}\left(\hat{S}_1^+ + \hat{S}_2^+ + \hat{S}_3^+\right)|00\downarrow\downarrow\rangle &= |00\uparrow\downarrow\rangle \\ &= \frac{1}{2}\left(|00\uparrow\downarrow\rangle + |00\downarrow\uparrow\rangle\right) + \frac{1}{2}\left(|00\uparrow\downarrow\rangle - |00\downarrow\uparrow\rangle\right) \\ &= \frac{1}{\sqrt{2}}|00\rightarrow\rangle + \frac{1}{\sqrt{2}}|00-\rangle.\end{aligned} \tag{6.47}$$

The final example is quite interesting since this results in a superposition between a triplet state and a singlet state. A similar pattern can be observed when applying the operator $\left(\hat{S}_1^- + \hat{S}_2^- + \hat{S}_3^-\right)$. These results can be generalized to the B-part of the Hamiltonian though in this case, the occupation of site 1 determines the outcome. The full matrices used in the numerical calculations are shown in **Appendix E**.

The tight binding part of the Hamiltonian will now be investigated. Since the spin is unchanged here, the singlet and the triplet states will not be coupled. One example is sufficient to illustrate what happens to all ten singlet states,

$$\hat{\mathcal{H}}_t|-00\rangle = -t\left(\sqrt{2}|-000\rangle + \sqrt{2}|0-00\rangle + |\overset{\frown}{0}\,0\rangle + |0-0\rangle + |\overset{\frown}{00}\,\rangle\right). \tag{6.48}$$

Note that a factor of $\sqrt{2}$ arises when two single occupied state becomes a double occupied state, since

$$\begin{aligned}\sum_\sigma \hat{c}_{1\sigma}^\dagger \hat{c}_{2\sigma}|-00\rangle &= \sum_\sigma \hat{c}_{1\sigma}^\dagger \hat{c}_{2\sigma}\frac{1}{\sqrt{2}}\left(\hat{c}_{1\uparrow}^\dagger \hat{c}_{2\downarrow}^\dagger - \hat{c}_{1\downarrow}^\dagger \hat{c}_{2\uparrow}^\dagger\right)|0\rangle \\ &= \frac{1}{\sqrt{2}}\left(\hat{c}_{1\uparrow}^\dagger \hat{c}_{1\downarrow}^\dagger - \hat{c}_{1\downarrow}^\dagger \hat{c}_{1\uparrow}^\dagger\right)|0\rangle = \sqrt{2}|-000\rangle.\end{aligned} \tag{6.49}$$

$|0\rangle$ represents the vacuum state. Due to the antisymmetry of a singlet state, the order of the fermionic operators is irrelevant. To see how the triplet states are affected by this, one example is again suffecient:

$$\begin{aligned}\hat{\mathcal{H}}_t|\uparrow\uparrow 00\rangle &= \sum_\sigma\left(\hat{c}_{3\sigma}^\dagger \hat{c}_{1\sigma} + \hat{c}_{3\sigma}^\dagger \hat{c}_{2\sigma} + \hat{c}_{4\sigma}^\dagger \hat{c}_{2\sigma}\right)|\uparrow\uparrow 00\rangle \\ &= \left(\hat{c}_{3\uparrow}^\dagger \hat{c}_{1\uparrow}\hat{c}_{1\uparrow}^\dagger \hat{c}_{2\uparrow}^\dagger + \hat{c}_{3\uparrow}^\dagger \hat{c}_{2\uparrow}\hat{c}_{1\uparrow}^\dagger \hat{c}_{2\uparrow}^\dagger + \hat{c}_{4\uparrow}^\dagger \hat{c}_{2\uparrow}\hat{c}_{1\uparrow}^\dagger \hat{c}_{2\uparrow}^\dagger\right)|0\rangle \\ &= \left(-\hat{c}_{2\uparrow}^\dagger \hat{c}_{3\uparrow}^\dagger + \hat{c}_{1\uparrow}^\dagger \hat{c}_{3\uparrow}^\dagger + \hat{c}_{1\uparrow}^\dagger \hat{c}_{4\uparrow}^\dagger\right)|0\rangle \\ &= -|0\uparrow\uparrow 0\rangle + |\uparrow 0\uparrow 0\rangle + |\uparrow 00\uparrow\rangle.\end{aligned} \tag{6.50}$$

The last term in Eq. (6.34) that includes the Coulomb repulsion between electrons occupying the same site is trivial to include for the four relevant double-occupied singlet states.

Now, the 448x448 Hamiltonian can be diagonalized numerically. To invoke an anitiferromagnetic coupling between the spin of the pyrazine electrons and the chromium spins, J must be negative. When all three variables, J, t and U, are comparable in size, the groundstate energy is two-fold degenerate. The eigenstates of these consists of superpositions, including many different states, though one basis state in each are highly dominant, i.e.,

$$|-3/2,-3/2\rangle \otimes |0 \uparrow\uparrow 0\rangle \quad \text{and} \quad |3/2,3/2\rangle \otimes |0 \downarrow\downarrow 0\rangle. \tag{6.51}$$

The contribution from the exchange interaction in the Hamiltonian is minimized for maximal spin of both the pyrazine electrons and the chromium spins. The Cr spins are antiparallel to the pyz spins due to the sign of J. Electrons located at site 2 and 3 couple to both chromium spins, in contrast to electrons located at site 1 and 4. Thus, the exchange interaction is further minimized by the electrons being located at site 2 and 3. For $t = 0$ this effect is even more dominant, and the amplitudes of the states shown in Eq. (6.51) increases. Though, when $t \neq 0$ the electrons can gain energy by delocalizing, and the amplitudes on the triplet states with $S_z = 0$ and the singlet states increases.

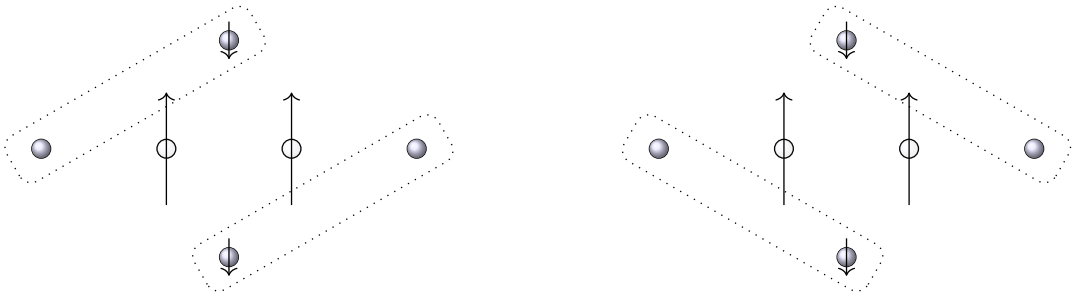

Fig. 6.9: The two different configurations of the spins on the pyrazine sites. The electron can delocalize over two sites with different exchange energy, in this way both minimizing the exchange coupling term and the tight binding term in Eq. (6.27).

Focusing on the dominant part of the eigenstates, i.e., going to the limit where $J \gg t$, a simple model is suggested to understand how the groundstate energy changes when increasing the hopping parameter t. For $t = 0$ the two electrons will be on site 2 and 3 with their spins antiparallel to the chromium spins. When t increases the two electrons can delocalize over two sites each and still avoid each other. This they can do in two different configurations. One electron can hop between site 1 and 2 while the other hops between 3 and 4, see **Fig. 6.9** (a), or one electron can hop between site 1 and 3 while the other hops between 2 and 4, see **Fig. 6.9** (b).

The two sites, over which a single electron delocalizes, do not exhibit the same energy, due to the fact that the electron can couple to both Cr spins at one site and not the other. The gap between these two levels is $\Delta = \frac{3J}{4}$. This yields the Hamiltonian

$$\hat{\mathcal{H}} = \begin{bmatrix} \frac{3J}{4} & t \\ t & \frac{-3J}{4} \end{bmatrix}, \tag{6.52}$$

with eigenvalues

$$E = \pm\sqrt{\left(\frac{3J}{4}\right)^2 + t^2}. \tag{6.53}$$

It is trivial to conclude that the negative solution is the groundstate. Now, this function can be plotted together with the exact eigenvalues as a function of t with $J = -0.2529$ eV and $U = 0.2529$ eV, see **Fig. 6.10**. The value chosen for J is taken from Pedersen et al. [4] as described in **section 6.2**. U is chosen to be of the same size as J. Note that Eq. (6.53) has been shifted to fit with the exact eigenvalues. Clearly, the exact groundstate energies follow this simple model quite closely. The exact solution is a bit lower in energy compared to Eq. (6.53). This can be explained by the fact that it can make the other configuration depicted in **Fig. 6.9** (b). This only lowers the energy slightly since the change must be coordinated such that the electrons still avoid each other. The solutions do not change when setting $U = 0$ since the states where the two electrons occupy the same site is not favourable in this model, even without U present in the model.

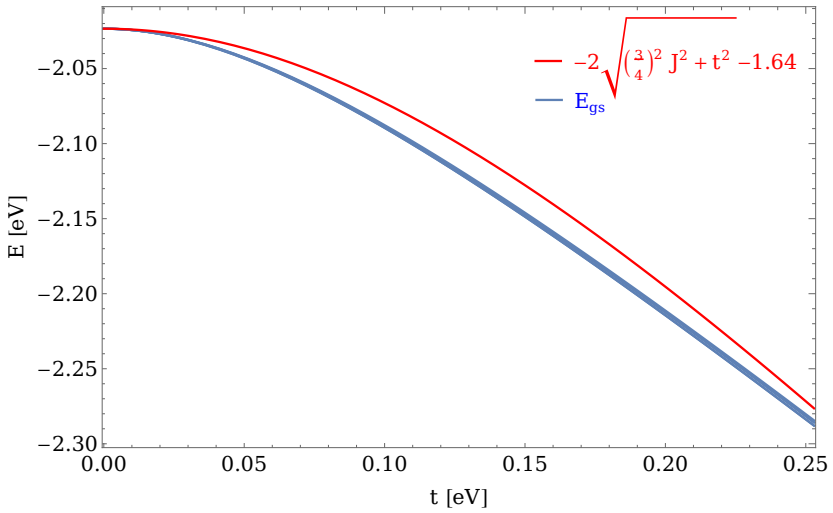

Fig. 6.10: The five lowest, degenerate eigenenergies plotted as a function of t with $J = -0.2529$ eV and $U = 0.2529$ eV alongside with the function in Eq. (6.53), though it has been shifted.

When $t = 0$ the groundstate energy becomes five-fold degenerate. Setting $t \neq 0$ this energy split in three, of which two is two-fold degenerate. That it is five-fold degenerate in the limit $J \gg t$ indicates that the system behaves as a spin 2 particle.

This can be understood from

$$\begin{aligned}\hat{S}^z_{tot}|3/2\rangle \otimes |3/2\rangle \otimes |0 \downarrow\downarrow 0\rangle &= \left(\hat{S}^z_A + \hat{S}^z_B + \hat{S}^z_2 + \hat{S}^z_3\right)|3/2\rangle \otimes |3/2\rangle \otimes |0 \downarrow\downarrow 0\rangle \\ &= \left(\frac{3}{2} + \frac{3}{2} - \frac{1}{2} - \frac{1}{2}\right)|3/2\rangle \otimes |3/2\rangle \otimes |0 \downarrow\downarrow 0\rangle \\ &= 2|3/2\rangle \otimes |3/2\rangle \otimes |0 \downarrow\downarrow 0\rangle.\end{aligned} \tag{6.54}$$

Clearly, this yield a ferrimagnetic ordering. All these five lowest states are plotted in **Fig. 6.10** both for $t = 0$ and $t \neq 0$. To see how these states are affected by an external magnetic field, the following term is added,

$$\hat{\mathcal{H}}_B = g\mu_B \mathbf{B} \cdot \hat{\mathbf{S}}_{tot} = g\mu_B B^z \hat{S}^z_{tot}. \tag{6.55}$$

The magnetic field is chosen to point in the z-direction. As seen in **Fig. 6.11** (a) the five-fold degeneracy of the groundstate for $t = 0$ is lifted when a magnetic field is applied. Furthermore, we see that for $t \neq 0$, see **Fig. 6.11** (b), the energy split in three, of which two is two-fold degenerate. The two double degenerate states act as a doublet, and the non-degenerate states behaves as a singlet for increasing magnetic fields.

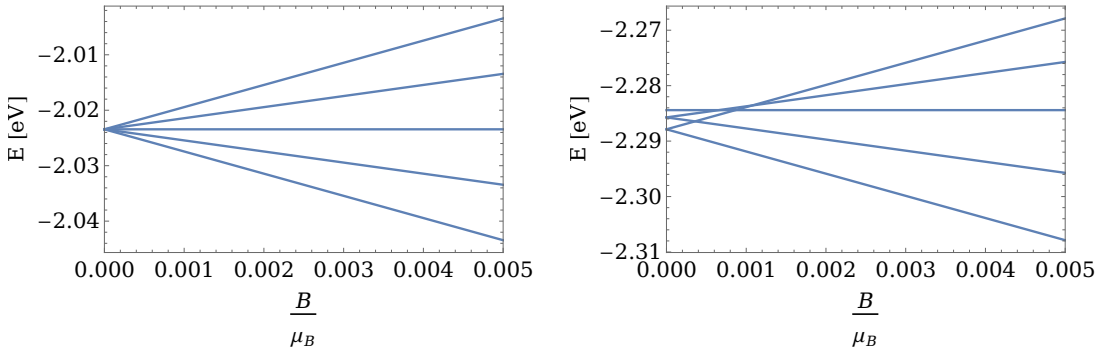

(a) (b)

Fig. 6.11: The five lowest eigenenergies of Eq. (6.27) + Eq. (6.55) depicted as a function of B/μ_b with $J = -0.2529$ eV, $U = 0.2529$ eV and $t = 0$ eV (a) or $t = 0.2529$ eV (b). Clearly, the degeneracy is lifted for $B \neq 0$.

From the introduced magnetic field, the expectation value of the total spin can be obtained using

$$\langle S_{tot} \rangle = \frac{\partial E}{\partial B}. \tag{6.56}$$

Both for $t = 0$ and $t \neq 0$, this is found numerically to yield $S = 2$, which agrees with previous conclusions.

We will now follow the same procedure as above, this time on a model that have a closer resemblance to the structure of $CrCl_2(pyz)_2$. In this case all four pyrazine sites exhibit the same exchange coupling to both chromium spins, see **Fig. 6.12**.

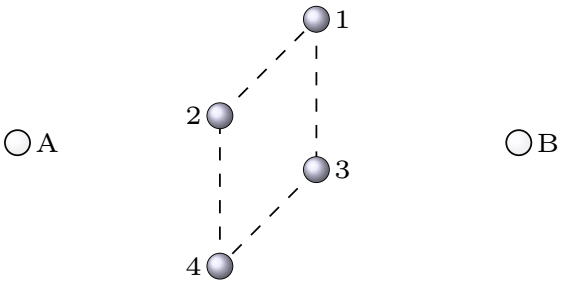

Fig. 6.12: Illustration of the model investigated in this section. It includes two Cr-ions (light grey) and four pyrazine sites (dark grey), on which two electrons in total can be located.

The same three interactions as in the previous section are included here. Due to the different shape of the model, the Hamiltonian is not completely identical to the previous. In this case the Hamiltonian reads

$$\begin{aligned}\hat{\mathcal{H}} = &-2J\left(\hat{\mathbf{S}}_A + \hat{\mathbf{S}}_B\right)\cdot\left(\hat{\mathbf{S}}_1 + \hat{\mathbf{S}}_2 + \hat{\mathbf{S}}_3 + \hat{\mathbf{S}}_4\right)\\ &- t\sum_{\sigma=\uparrow\downarrow}\left(\hat{c}^\dagger_{1\sigma}\hat{c}_{2\sigma} + \hat{c}^\dagger_{2\sigma}\hat{c}_{4\sigma} + \hat{c}^\dagger_{1\sigma}\hat{c}_{3\sigma} + \hat{c}^\dagger_{3\sigma}\hat{c}_{4\sigma} + h.c.\right)\\ &+ U\sum_{i=1}^{4}\sum_{\sigma\sigma'=\uparrow\downarrow}\hat{c}^\dagger_{i\sigma'}\hat{c}^\dagger_{i\sigma}\hat{c}_{i\sigma}\hat{c}_{i\sigma'}.\end{aligned} \tag{6.57}$$

To diagonalize this Hamiltonian numerically, the basis used above is employed. Since all sites now couple to both chromium spins, singlet and triplet states do no longer couple. Thus, the exchange part of the Hamiltonian simply consists of operators acting on the total spin of the state. For the tight binding part of the Hamiltonian, a factor of $\sqrt{2}$ is still introduced when two single occupied states become a double occupied state and vice versa. Further, the ordering of the creation and annihilation operators still results in sign changes for the triplet states.
Solving Eq. (6.57) numerically, we find that for $t = 0$ eV the groundstate energy is thirty-fold degenerate whereas when $t \neq 0$ the groundstate energy is ten times degenerate. This higher degeneracy is due to the increased symmetry of this model compared to the former. Two of these groundstates are dominated by the following basis states

$$|-3/2\rangle \otimes |-3/2\rangle \otimes |00\uparrow\uparrow\rangle \quad \text{and} \quad |-3/2\rangle \otimes |-3/2\rangle \otimes |\uparrow\uparrow 00\rangle. \tag{6.58}$$

The other eigenstates include many more states where none dominates as clearly as these two states. Now we can simplify this model to only include the two states in Eq. (6.58) where the hopping allows them to delocalize in two different configurations as shown in **Fig. 6.13**. In this case the site over which the electron delocalizes exhibit the same energy, so the eigenenergies is expected to decrease with a slope of $-2t$. This is exactly what is observed from the eigenvalues, see **Fig. 6.14**.

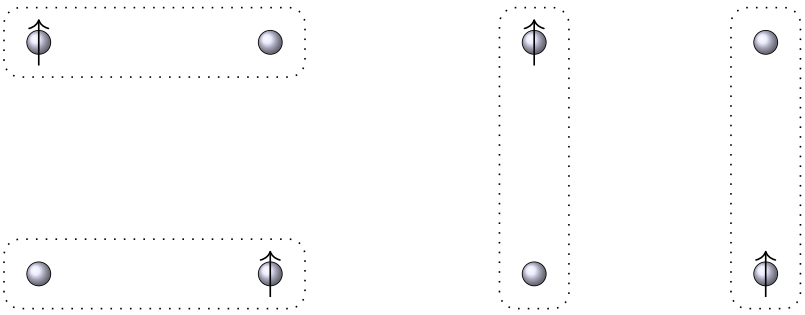

Fig. 6.13: The two configurations of the spins on the pyrazine sites in this model. The electrons can delocalize over two sites, in this way both minimizing the tight binding part and exchange part of the Hamiltonian. For simplicity the chromium atoms have been omitted.

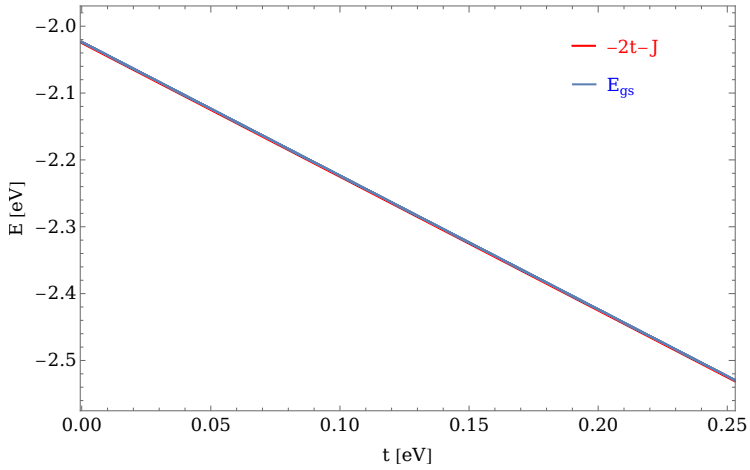

Fig. 6.14: The ten lowest, degenerate eigenenergies plotted as a function of t with $J = -0.2529$ eV and $U = 0.2529$ eV together with the function $-2t - J$.

Adding a magnetic field using Eq. (6.55), the expectation value of the total spin of this toy model is also found to be $S = 2$. Since this model contains the same number of pyrazine rings and chromium atoms as two unit cells of $CrCl_2(pyz)_2$, this would correspond to one unit cell having $S = 1$. This yields a magnetic moment of $2\mu_B$, which agrees with previous results obtained above. Further, it agrees with both the experimental and numerical results from Pedersen et al. [4]. Generalizing these results to monolayer $CrCl_2(pyz)_2$, a possible configuration is depicted in **Fig. 6.15**. The spin of the electrons on the pyrazine sites couple ferromagnetically, and each delocalize over two neighbouring pyrazine sites. Further, the electrons on the pyrazine sites couple antiferromagnetically with the spins of the chromium sites. Due to the uneven length of the spins on the chromium sites and the spins on the pyrazine sites, this results in a ferrimagnetic coupling. Obviously, the delocalization of the electrons can be configured in several ways, but one configuration is chosen since it will be very energetically costly to change configuration. The electrons on the pyrazine sites are drawn randomly on either of the two sites it can occupy.

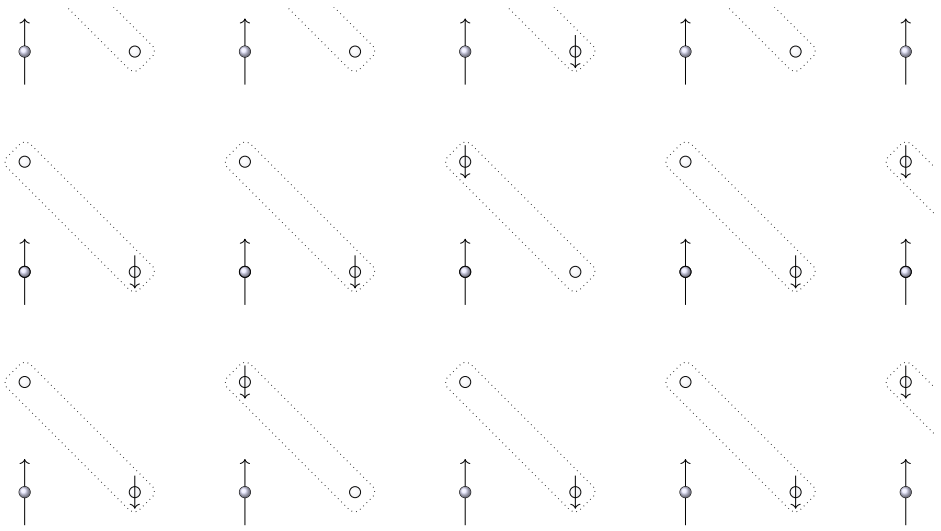

Fig. 6.15: A sketch of one of the configurations the spins on the pyrazine ligands can choose.

This model provides an approximate and intuitive description of $CrCl_2(pyz)_2$, though it is most likely too simple to grasp the physical aspects of the material. Due to the big size of the pyrazine rings, the Coulomb repulsion on these sites are quite low. Thus, the electrons on the pyrazine sites can most likely gain a lot of energy by delocalizing in a greater extend than this model allow for. Instead, the valence electrons on the chromium sites can be viewed as localized ions, and the electrons on the pyrazine ligands as a free electron gas. Thus, this interaction can be investigated using the RKKY (Ruderman-Kittel-Kasuya-Yosida) model to describe the indirect exchange coupling between neighbouring chromium spins. First, the direct exchange interaction between the chromium spins and the pyrazine spins is investigated.

6.4.3 Exchange Interaction between Cr and Pyz

To understand why $CrCl_2(pyz)_2$ exhibit ferrimagnetic properties, the direct exchange interaction between the spins on the chromium sites and the neighbouring pyrazine sites can be investigated. Here, two electrons exchange location with one intermediate step. In this proces the spin of the included electrons remain unchanged. In the crystallized environment five relevant energy levels are present on the chromium site of which three of these are singly occupied. Let $|\psi\rangle$ represent the relevant eigenstate of the highest occupied energy level on the chromium site. This is a superpostion of d-orbitals, and the explicit expression is obtained from the numerical calculations of the band structures obtained in **section 6.4.1**. Both pyrazine sites in the unit cell will be included. Let $|\phi\rangle$ represent the relevant eigenstate of the highest occupied state on the pyrazine sites. This can be written as

$$|\phi\rangle = \frac{1}{\sqrt{2}} \left(|\phi_1\rangle + |\phi_2\rangle \right), \tag{6.59}$$

where $|\phi_1\rangle$ and $|\phi_2\rangle$ denotes the eigenstates of the highest occupied energy level on the two pyrazine sites in the unit cell, also obtained from the band structure.

Seven electrons are present in this collective pyrazine site. The electron on the highest occupied state on the chromium site should now exchange location with the electron on the highest occupied state on the collective pyrazine site. This exchange can be achieved in many ways, though two are by far the most dominant. Both are illustrated in **Fig. 6.16**.

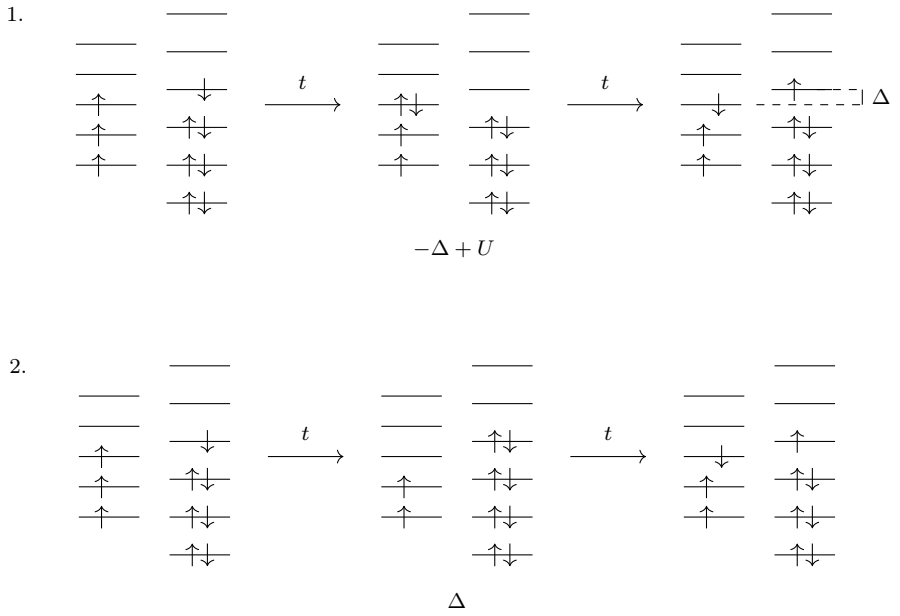

Fig. 6.16: Schematic view of the two ways that an electron on the pyrazine sites can exchange location with an electron on the chromium site of one unit cell. Left column illustrates the energy levels of the five d-orbitals. Right column illustrates the six energy levels of two included pyrazine sites.

An expression for the change in energy, that arises from the interaction, is obtained through second order perturbation theory,

$$\Delta E^{(2)} = -\frac{|\langle\psi|\hat{\mathcal{H}}_t|\phi\rangle|^2}{-\Delta + U} - \frac{|\langle\psi|\hat{\mathcal{H}}_t|\phi\rangle|^2}{\Delta} = -|\langle\psi|\hat{\mathcal{H}}_t|\phi\rangle|^2 \left(\frac{1}{(1-\Delta/U)\Delta}\right) = J. \quad (6.60)$$

$\hat{\mathcal{H}}_t$ denotes the tight binding Hamiltonian given in Eq. (5.1). Δ denotes the difference in energy of the two relevant energy levels, and U is the strength of the Coulomb repulsion of two electrons occupying the same energy level on the chromium site, see **Fig. 6.16**. The Coulomb repulsion for two electrons occupying the same energy level on the two pyrazine sites is neglected due to the much larger spatial extend compared to the chromium site. For the coupling between the Cr sites and the pyrazine sites to be antiferromagnetic, it requires that $\Delta > U$.

6.4.4 RKKY Interaction

In this section the chromium spins are viewed as localized spins whereas the electrons occupying the pyrazine sites are viewed as a free electron gas. The indirect exchange interaction between neighbouring chromium spins is then mediated by these free pyrazine electrons. We will focus on two specific neighbouring Cr-ions, i.e., $\mathbf{S}_1$ and $\mathbf{S}_2$. The exchange interaction in real space between the spin of the Cr-ions and the spin of the electron, $\hat{\mathbf{s}}$, on the two pyrazine sites, can be written as

$$\hat{\mathcal{H}}_1 = -2J \sum_{\boldsymbol{\delta}} \hat{\mathbf{S}}_1 \cdot \hat{\mathbf{s}}_{\boldsymbol{\delta}}, \tag{6.61}$$

$$\hat{\mathcal{H}}_2 = -2J \sum_{\boldsymbol{\delta}'} \hat{\mathbf{S}}_2 \cdot \hat{\mathbf{s}}_{\boldsymbol{\delta}'}. \tag{6.62}$$

$\boldsymbol{\delta}$ and $\boldsymbol{\delta}'$ sums over the vectors pointing to the four neighbouring pyrazine sites of $\mathbf{S}_1$ and $\mathbf{S}_2$, respectively. The spin of the valence electrons can be written as

$$\hat{\mathbf{s}}_\delta = \frac{1}{2} \sum_{\sigma\sigma'} \hat{c}^\dagger_{\delta\sigma} \boldsymbol{\tau}_{\sigma\sigma'} \hat{c}_{\delta\sigma'} = \frac{1}{2N} \sum_{\sigma\sigma'} \sum_{\mathbf{k}\mathbf{k}'} \hat{c}^\dagger_{\mathbf{k}\sigma} \boldsymbol{\tau}_{\sigma\sigma'} \hat{c}_{\mathbf{k}'\sigma'}. \tag{6.63}$$

In the last step the term is Fourier transformed using Eq. (5.68). $\boldsymbol{\tau} = (\boldsymbol{\tau}^x, \boldsymbol{\tau}^y, \boldsymbol{\tau}^z)$ is a vector consisting of the Pauli matrices. Thus, the two interaction Hamiltonians can be written in reciprocal space as

$$\hat{\mathcal{H}}_1 = -\frac{J}{N} \sum_{\boldsymbol{\delta}} \sum_{\sigma\sigma'} \sum_{\mathbf{k}\mathbf{k}'} \hat{c}^\dagger_{\mathbf{k}\sigma} \hat{c}_{\mathbf{k}'\sigma'} \sum_{l=x,y,z} \tau^l_{\sigma\sigma'} S^l_1, \tag{6.64}$$

$$\hat{\mathcal{H}}_2 = -\frac{J}{N} \sum_{\boldsymbol{\delta}} \sum_{\sigma''\sigma'''} \sum_{\mathbf{k}''\mathbf{k}'''} \hat{c}^\dagger_{\mathbf{k}''\sigma''} \hat{c}_{\mathbf{k}'''\sigma'''} \sum_{m=x,y,z} \tau^m_{\sigma''\sigma'''} S^m_2. \tag{6.65}$$

Perturbation theory can now be applied to these interactions. The lowest order term that include both interactions [40] is

$$\frac{\mathcal{Z}^{(2)}}{\mathcal{Z}_0} = \int_0^\beta d\tau_1 \int_0^\beta d\tau_2 \left\langle \hat{T}_\tau \left(\hat{\mathcal{H}}^I_1(\tau_1) \hat{\mathcal{H}}^I_2(\tau_2) \right) \right\rangle_0. \tag{6.66}$$

$\mathcal{Z}$ denotes the partition function, β is inverse temperature and $\langle \cdot \rangle_0$ means that the expectation value should be taken with respect to the unperturbed groundstate. $\hat{T}_\tau$ denotes the time ordering operator, where τ_1 and τ_2 are imaginary time parameters. The superscript I states that the Hamiltonians should be given in the interaction picture[7].

In the most commen version of the RKKY model, the itinerant electrons are viewed as a completely free electron gas. In this case these electrons are viewed as delocalized electrons though they are anchored at the four neighbouring sites of the given chromium sites. For the spin-operators in each correlation function, we must sum over all bonds to the relevant chromium spin. The dominant term will thus be the term where the neighbouring chromium atoms couple through an electron anchored to the site in between them.

[7] This is described in chapter 11 of [40].

Thus, we end with

$$J_{Cr-Cr} = \frac{2J^2}{N^2}\mathbf{S}_1 \cdot \mathbf{S}_2\, \chi, \tag{6.67}$$

where χ is the Lindhard function given by

$$\chi = \quad = \sum_{\mathbf{k}\mathbf{k}'} \frac{n_F(\xi_{\mathbf{k}}) - n_F(\xi_{\mathbf{k}})}{\xi_{\mathbf{k}} - \xi_{\mathbf{k}'}}. \tag{6.68}$$

The factor of two in Eq. (6.67) stems from the fact that

$$\langle \psi_{\mathbf{k}\sigma} | \boldsymbol{\tau}^{\alpha} \boldsymbol{\tau}^{\beta} | \psi_{\mathbf{k}\sigma} \rangle = Tr[\boldsymbol{\tau}^{\alpha} \boldsymbol{\tau}^{\beta}] = 2\delta_{\alpha\beta}. \tag{6.69}$$

Here, $|\psi_{\mathbf{k}\sigma}\rangle$ are Bloch waves describing the free pyz electrons. At $T = 0$ the fermi functions in Eq. (6.68) is either equal to one or zero. The Lindhard function can then be written as

$$\chi = 2 \sum_{\mathbf{k}>\mathbf{k}_F} \sum_{\mathbf{k}'<\mathbf{k}_F} \frac{1}{\xi_{\mathbf{k}} - \xi_{\mathbf{k}'}} = 2 \int_{\xi_F} d\xi \int^{\xi_F} d\xi' \frac{D(\xi) D(\xi')}{\xi - \xi'}, \tag{6.70}$$

where $D(\xi)$ is the DOS. The DOS for a square lattice with spectrum $\xi = 2t(\cos k_x + cosk_y)$ is given by

$$D(\xi) = \frac{N^2}{2(\pi t)^2} K\left(1 - \left(\frac{\xi}{4t}\right)^2\right). \tag{6.71}$$

Here K gives the complete elliptic integral of the first kind which can be defined as the power series

$$K(k) = \frac{\pi}{2} \sum_{n=0}^{\infty} \left(\frac{(2n)!}{2^{2n}(n!)^2}\right)^2 k^{2n}. \tag{6.72}$$

The DOS is plotted as a function of energy in **Fig. 6.17**. In the subspace of the pyrazine sites, there is 1/2 electron in each unit cell, and thus the DOS will be a 1/4 filled due to spin. The DOS is normalized such that

$$\int_{-4t}^{4t} d\xi D(\xi) = 1. \tag{6.73}$$

Thus, the Fermi energy can be found by requiring that

$$\int_{-4t}^{\xi_F} d\xi D(\xi) = \frac{1}{4}. \tag{6.74}$$

The Fermi energy is obtained numerically, and the Lindhard function is found to have a numerical value of 0.15 for $t = 1$, such that

$$J_{Cr-Cr} = 0.3\frac{J^2}{t}. \tag{6.75}$$

This gives an idea of the order of magnitude of J_{Cr-Cr} in terms of J and t.

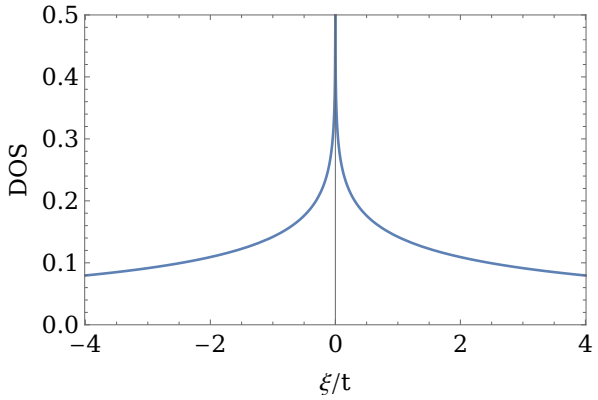

Fig. 6.17: The DOS for a square lattice with spectrum $\xi = 2t(\cos k_x + cosk_y)$.

6.4.5 Estimate of Curie temperature from mean-field theory

From mean-field theory an expression of the exchange coupling constant between neighbouring chromium spins $\mathbf{S}_i$ can be obtained. The Hamiltonian of this exchange interaction can be written as

$$\hat{\mathcal{H}} = -2J_{Cr-Cr} \sum_{\langle i,j \rangle} \mathbf{S}_i \cdot \mathbf{S}_j. \tag{6.76}$$

Using mean-field theory and neglecting the constant shift, see Eq. (5.126), the interaction of the ith spin is

$$\hat{\mathcal{H}}_i = -2J_{Cr-Cr} z \langle \mathbf{S} \rangle \cdot \mathbf{S}_i, \tag{6.77}$$

where z denotes the number of neighbouring spins, i.e., $z = 4$ for a square lattice. Defining

$$\mathbf{H} = -\frac{2zJ_{Cr-Cr}}{g\mu_B} \langle \mathbf{S} \rangle, \tag{6.78}$$

the Hamiltonian for the ith spin can be written as

$$\hat{\mathcal{H}}_i = g\mu_B \mathbf{S}_i \cdot \mathbf{H}. \tag{6.79}$$

Thus, $\mathbf{H}$ can be viewed as an exchange field affecting the ith spin, that arise from the polarization of the spins on the neighbouring chromium sites. The magnetization from this exchange field is given by

$$\mathbf{M} = -g\mu_B N \langle \mathbf{S} \rangle, \tag{6.80}$$

where N is the number of magnetic chromium atoms in the sample. The exchange field can be written as

$$\mathbf{H} = A\mathbf{M}, \quad \text{with} \quad A = \frac{2zJ_{Cr-Cr}}{g^2\mu_B^2 N}. \tag{6.81}$$

Including an external magnetic field **B** the total magnetization can be written as

$$M = \frac{C}{T}(B + AM), \tag{6.82}$$

where C is the Curie constant which, for $L = 0$, is given by

$$C = \frac{\mu_0 \mu_B^2}{3k_B} N g^2 S(S+1). \tag{6.83}$$

The magnetization can now be isolated

$$M = \frac{C}{T - AC} B. \tag{6.84}$$

Knowing the Curie-Weiss law given by

$$\chi = \frac{C}{T - T_c}, \tag{6.85}$$

we can conclude that $AC = T_C$, where T_C is the Curie temperature, from which we obtain the expression

$$J_{Cr-Cr} = \frac{3k_B T_C}{2\mu_0 z S(S+1)}. \tag{6.86}$$

Remember that $S = 3/2$, $T_C \simeq 55$ K and $z = 4$. This gives an idea of the order of magnitude of J_{Cr-Cr}. Combining this equation with Eq. (6.75), an estimate of the order of magnetude of J can be obtained.

6.5 Conclusion

To begin with, an analytical expression of the energy spectrum of $CrCl_2(pyz)_4$ was obtained, see Eq. (6.3), and the symmetry of this was explored using group theory. Thereafter, monolayer $CrCl_2(pyz)_2$ was studied. From the band structure, see **Fig. 6.6**, the compound was found to exhibit an insulating groundstate in agreement with the experimental results. Furthermore, the d-bands were observed to be quite flat, which suggested that these are localized. To investigate the magnetic properties of monolayer $CrCl_2(pyz)_2$ a simple model was proposed. Here, the electrons on the chromium sites were viewed as localized spins, whereas the electrons on the pyrazine sites could delocalize over a few sites. This suggested a specific configuration of the spin, see **Fig. 6.15**, which resulted in a magnetic moment of one unit cell to be $2\mu_B$. This corresponds to an antiferromagnetic interaction between the chromium spins and the pyrazine spins. Considering the exchange interaction between these two using second order perturbation theory, this was exactly what was observed, see Eq. (6.60). An antiferromagnetic coupling between the pyrazine spins and the chromium spins resulted in a ferromagnetic coupling between neighbouring chromium spins. Due to the uneven lengths of the chromium spin and the pyrazine spin, this yielded in a ferrimagnetic ordering. The

itinerant electrons on the pyrazine sites could be viewed as an electron gas such that the indirect exchange between neighbouring chromium sites is mediated by the RKKY interaction. From this an expression for the Cr-Cr indirect exchange coupling constant, J_{Cr-Cr}, expressed in terms of the Cr-pyz direct exchange constant was obtained, see Eq. (6.75). Furthermore, from mean-field theory an expression of J_{Cr-Cr} in terms of the ordering temperature was found, see Eq. (6.86).

Chapter 7

Conclusion and Further Research

In this thesis three distinct two-dimensional compounds have been investigated theoretically. To begin with, monolayer YbOCl was studied using the classical Heisenberg model. Focusing on the single hole occupying each ytterbium site in a triangular lattice, these spin 1/2 particles was studied. The groundstate of monolayer YbOCl was found to be dependent on the relative size of the exchange coupling constant between spins in the same sublayer J, and the exchange interaction coupling strength between spins located in two different sublayers J_{tb}. Further, this depended on the sign of both J and J_{tb}. A non-magnetic region with $S = 0$ was obtained. Outside this region the Hamiltonian, see Eq. (4.10), was minimized when the total spin was maximal, though the size of ϕ depended on the sign and sizes of J_{tb} and J. Both regions exhibited ferromagnetic intralayer couplings. One region exhibited antiferromagnetic interlayer coupling whereas the other exhibited ferromagnetic interlayer coupling between the spins. All phases are depicted in **Fig. 4.5**. Thereafter, an external magnetic field was introduced. Again, the groundstate configuration was dependent on the relative size and signs of J_{tb} and J. For $J_{tb} < 0$ and $J < 0$, both a ferromagnetic inter- and intralayer magnetic coupling minimized the Hamiltonian, see Eq. (4.20). These spins were oriented antiparallel to the magnetic field. For $J_{tb} > 0$ and $J > 0$, $J_{tb} > 0$ and $J < 0$ and $J_{tb} < 0$ and $J > 0$ various phases were observed. The phase digram between B/μ_B and J_{tb}/J for these three cases are depicted in **Fig. 4.6** and **Fig. 4.7**. Except for a small region with $S = 0$, the spins are oriented antiparallely to the external magnetic field. The non-magnetic region with $S = 0$ was much smaller in the presence of the external magnetic field. Thus, in a specific part of the phase diagram between J_{tb} and J, the compound is paramagnetic in agreement with the experimental measurements [25]. For further research the spin waves could be investigated using the Holstein Primakoff transformation.

Further, the TMD VS_2 has been considered. First, the energy spectrum of the hypothetical model complex VS_6 was obtained using the tight binding model and the degeneracies observed, see **Fig. 5.3** and **Fig. 5.7**, was explained using group theory. The band structure of both the 1T and the 2H phase of monolayer VS_2 was obtained using the tight binding method combined with the Hubbard model, see **Fig. 5.16** and **Fig. 5.12**. The 2H structure was found to exhibit a metallic groundstate, even though the highest non-empty band was almost filled. Thus, the groundstate was highly spin-polarized and the compound was ferromagnetic. This agrees with the DFT calculations from Wang et al. [2]. The DFT calculations from DTU [3] showed contradicting results, though one method also agreed with a metallic ferromagnetic groundstate. 1T-VS_2 was also found to exhibit metallic behaviour, though the highest occupied energy band was only partially spin polarized and thus exhibited a smaller magnetic moment compared to 2H-VS_2. This result agrees with DFT calculations. Due to the stagnation

of the experimental investigation of VS_2 in Beijing, this project was concluded here. An experimental study of the magnetic and electronic properties of VS_2 should motivate further theoretical investigation of this.

Lastly, the 2D material $CrCl_2(pyz)_2$ has been studied using a similar approach as for VS_2. First, an analytical expression of the energy spectrum of $CrCl_2(pyz)_4$ was obtained, see Eq. (6.3), and the symmetry of this was explored using group theory. Thereafter, the band structure was obtained using the tight binding model, see **Fig. 6.6**, from which the compound was found to exhibit an insulating groundstate. This agrees with the experimental results of the electronic conductivity [4]. From the band structure, the spins on the chromium sites are found to be localized in contrary to the electrons on the pyraine ligands. To investigate the magnetic properties of monolayer $CrCl_2(pyz)_2$ a simple model was proposed. This suggested a specific configuration of the spin, see **Fig. 6.15**, which resulted in a magnetic moment of one unit cell to be $2\mu_B$. This corresponded to an antiferromagnetic coupling between the chromium spins and the pyrazine spins. Considering the exchange interaction between the Cr spins and the neighbouring pyz spins using second order perturbation theory, this is exactly what was observed, see Eq. (6.60). An antiferromagnetic coupling between the pyrazine electrons and the chromium electrons invokes a ferromagnetic coupling between neighbouring chromium spins. Due to the uneven lengths of the spins on the chromium sites and the spins on the pyrazine sites, this results in a ferrimagnetic ordering in agreement with Pedersen et al. [4]. The itinerant electrons on the pyrazine sites could be viewed as a free electron gas such that the indirect exchange coupling between neighbouring chromium sites is mediated by the RKKY interaction. From this an expression for the indirect Cr-Cr exchange coupling constant, J_{Cr-Cr}, expressed in terms of the Cr-pyz exchange constant, J, was obtained, see Eq. (6.75). Furthermore, from mean-field theory an expression of J_{Cr-Cr} in terms of the ordering temperature was found, see Eq. (6.86). Neutron scattering data of the compound has been realized recently (N. B. Christensen and X. Chen, personal communication, December 2020). This measures both the ordering temperature and the spin waves. Motivated by this, further research could adress this theoretically. Ferromagnetic spin waves for a square lattice including nearest neighbour coupling J_{Cr-Cr} could be calculated. In this thesis only monolayer $CrCl_2(pyz)_2$ has been studied, though the compound on which the neutron scattering mesaurements are performed is bulk $CrCl_2(pyz)_2$. The interlayer exchange coupling constant J'_{Cr-Cr} has a smaller magnitude compared to J_{Cr-Cr}. Thus, a mean-field ordering temperature could be obtained in terms of J_{Cr-Cr} and J'_{Cr-Cr}. Lastly, a collaboration with experts on DFT calculations could be established in the pursuit of more accurate parameters entering the tight binding calculations.

Bibliography

[1] N. Mounet, M. Gibertini, P. Schwaller, D. Campi, A. Merkys, A. Marrazzo, T. Sohier, I. E. Castelli, A. Cepellotti, G. Pizzi, and N. Marzari, "Two-dimensional materials from high-throughput computational exfoliation of experimentally known compounds," *Nature Nanotechnology*, vol. 13, pp. 246–252, Mar. 2018.

[2] W. Wang, "First-principles investigations of vanadium disulfide for lithium and sodium ion battery applications," *RSC Advances*, p. 6, 2016.

[3] S. Haastrup, M. Strange, M. Pandey, T. Deilmann, P. S. Schmidt, N. F. Hinsche, M. N. Gjerding, D. Torelli, P. M. Larsen, A. C. Riis-Jensen, J. Gath, K. W. Jacobsen, J. J. Mortensen, T. Olsen, and K. S. Thygesen, "The Computational 2D Materials Database: High-throughput modeling and discovery of atomically thin crystals," *2D Materials*, vol. 5, p. 042002, Sept. 2018.

[4] K. S. Pedersen, P. Perlepe, M. L. Aubrey, D. N. Woodruff, S. E. Reyes-Lillo, A. Reinholdt, L. Voigt, Z. Li, K. Borup, M. Rouzières, D. Samohvalov, F. Wilhelm, A. Rogalev, J. B. Neaton, J. R. Long, and R. Clérac, "Formation of the layered conductive magnet $CrCl_2(pyrazine)_2$ through redox-active coordination chemistry," *Nature Chemistry*, vol. 10, pp. 1056–1061, Oct. 2018.

[5] K. S. Novoselov, A. K. Geim, S. V. Morozov, D. Jiang, Y. Zhang, S. V. Dubonos, I. V. Grigorieva, and A. A. Firsov, "Electric Field Effect in Atomically Thin Carbon Films," *Science*, vol. 306, pp. 666–669, Oct. 2004.

[6] "What is graphene? Graphene characteristics and applications." `https://www.atriainnovation.com/en/graphene-characteristics-and-applications/`, Mar. 2020. (accessed 2020-12-16).

[7] W. Choi, N. Choudhary, G. H. Han, J. Park, D. Akinwande, and Y. H. Lee, "Recent development of two-dimensional transition metal dichalcogenides and their applications," *Materials Today*, vol. 20, pp. 116–130, Apr. 2017.

[8] N. E. Staley, J. Wu, P. Eklund, Y. Liu, L. Li, and Z. Xu, "Electric field effect on superconductivity in atomically thin flakes of $NbSe_2$," *Physical Review B*, vol. 80, p. 184505, Nov. 2009.

[9] Q. Yue, J. Kang, Z. Shao, X. Zhang, S. Chang, G. Wang, Q. Shiqiao, and J. Li, "Mechanical and electronic properties of monolayer MoS_2 under elastic strain," *Physics Letters A*, vol. 376, pp. 1166–1170, Feb. 2012.

[10] J. Shi, R. Tong, X. Zhou, Y. Gong, Z. Zhang, Q. Ji, Y. Zhang, Q. Fang, L. Gu, X. Wang, Z. Liu, and Y. Zhang, "Temperature-Mediated Selective Growth of MoS_2/ WS_2 and WS_2/ MoS_2 Vertical Stacks on Au Foils for Direct Photocatalytic Applications," *Advanced Materials (Deerfield Beach, Fla.)*, vol. 28, pp. 10664–10672, Dec. 2016.

[11] N. Miao, B. Xu, L. Zhu, J. Zhou, and Z. Sun, "2D Intrinsic Ferromagnets from van der Waals Antiferromagnets," *Journal of the American Chemical Society*, vol. 140, pp. 2417–2420, Feb. 2018.

[12] W. Li, H. M. K. Sari, and X. Li, "Emerging Layered Metallic Vanadium Disulfide for Rechargeable Metal-Ion Batteries: Progress and Opportunities," *ChemSusChem*, vol. 13, no. 6, pp. 1172–1202, 2020.

[13] A. Hirohata, K. Yamada, Y. Nakatani, I.-L. Prejbeanu, B. Diény, P. Pirro, and B. Hillebrands, "Review on spintronics: Principles and device applications," *Journal of Magnetism and Magnetic Materials*, vol. 509, p. 166711, Sept. 2020.

[14] M. Tinkham, *Group Theory and Quantum Mechanics*. McGraw-Hill, 1964.

[15] K. S. Novoselov, D. Jiang, F. Schedin, T. J. Booth, V. V. Khotkevich, S. V. Morozov, and A. K. Geim, "Two-dimensional atomic crystals," p. 3.

[16] H. Tributsch, "Layer-Type Transition Metal Dichalcogenides — a New Class of Electrodes for Electrochemical Solar Cells," *Berichte der Bunsengesellschaft für physikalische Chemie*, vol. 81, no. 4, pp. 361–369, 1977.

[17] R. Lv, H. Terrones, A. L. Elías, N. Perea-López, H. R. Gutiérrez, E. Cruz-Silva, L. P. Rajukumar, M. S. Dresselhaus, and M. Terrones, "Two-dimensional transition metal dichalcogenides: Clusters, ribbons, sheets and more," *Nano Today*, vol. 10, pp. 559–592, Oct. 2015.

[18] J. Xia, J. Yan, and Z. X. Shen, "Transition metal dichalcogenides: Structural, optical and electronic property tuning via thickness and stacking," *FlatChem*, vol. 4, pp. 1–19, Aug. 2017.

[19] S. Manzeli, D. Ovchinnikov, D. Pasquier, O. V. Yazyev, and A. Kis, "2D transition metal dichalcogenides," *Nature Reviews Materials*, vol. 2, pp. 1–15, June 2017.

[20] A. R. Botello-Méndez, F. López-Urías, M. Terrones, and H. Terrones, "Metallic and ferromagnetic edges in molybdenum disulfide nanoribbons," *Nanotechnology*, vol. 20, p. 325703, July 2009.

[21] J. Zhang, J. M. Soon, K. P. Loh, J. Yin, J. Ding, M. B. Sullivian, and P. Wu, "Magnetic Molybdenum Disulfide Nanosheet Films," *Nano Letters*, vol. 7, pp. 2370–2376, Aug. 2007.

[22] R. Jones, H. Shanks, D. Finnemore, and B. Morosin, "Pressure effect on superconducting $NbSe_2$ and NbS_2," *Physical Review B*, vol. 6, no. 3, pp. 835–838, 1972.

[23] I. Guillamón, H. Suderow, S. Vieira, L. Cario, P. Diener, and P. Rodière, "Superconducting Density of States and Vortex Cores of 2H-NbS_2," *Physical Review Letters*, vol. 101, p. 166407, Oct. 2008.

[24] Y. B. Pottathara, S. Thomas, N. Kalarikkal, Y. Grohens, and V. Kokol, *Nanomaterials Synthesis*. Elsevier, 2019.

[25] K. Song and S. M. Kauzlarich, "New Intercalation Compounds of Layered Lanthanide Oxychlorides LnOCl (Ln = Ho, Er, Tm, and Yb) with Pyridine and Substituted Pyridines," p. 9.

[26] Y. Yao, Y. Zhang, W. Xiong, Z. Wang, M. G. Sendeku, N. Li, J. Wang, W. Huang, F. Wang, X. Zhan, S. Yuan, C. Jiang, C. Xia, and J. He, "Growth and Raman Scattering Investigation of a New 2D MOX Material: YbOCl," *Advanced Functional Materials*, vol. 29, p. 1903017, Oct. 2019.

[27] L. Li, Z. Li, A. Yoshimura, C. Sun, T. Wang, Y. Chen, Z. Chen, A. Littlejohn, Y. Xiang, P. Hundekar, S. F. Bartolucci, J. Shi, S.-F. Shi, V. Meunier, G.-C. Wang, and N. Koratkar, "Vanadium disulfide flakes with nanolayered titanium disulfide coating as cathode materials in lithium-ion batteries," *Nature Communications*, vol. 10, p. 1764, Dec. 2019.

[28] Y. Guo, H. Deng, X. Sun, X. Li, J. Zhao, J. Wu, W. Chu, S. Zhang, H. Pan, X. Zheng, X. Wu, C. Jin, C. Wu, and Y. Xie, "Modulation of Metal and Insulator States in 2D Ferromagnetic VS_2 by van der Waals Interaction Engineering," *Advanced Materials*, vol. 29, p. 1700715, Aug. 2017.

[29] J. C. Slater and G. F. Koster, "Simplified LCAO Method for the Periodic Potential Problem," *Physical Review*, vol. 94, pp. 1498–1524, June 1954.

[30] A. Gelessus, "Character table for point group D3d." `http://symmetry.jacobs-university.de/cgi-bin/group.cgi?group=703&option=4`, Feb. 2020. (accessed 2020-02-10).

[31] A. Gelessus, "Character table for point group Oh." `http://symmetry.jacobs-university.de/cgi-bin/group.cgi?group=904&option=4`. (accessed 2020-02-10).

[32] A. Gelessus, "Character table for point group D3h." `http://symmetry.jacobs-university.de/cgi-bin/group.cgi?group=603&option=4`. (accessed 2020-02-17).

[33] E. Ridolfi, D. Le, T. S. Rahman, E. R. Mucciolo, and C. H. Lewenkopf, "A tight-binding model for MoS_2 monolayers," *Journal of Physics: Condensed Matter*, vol. 27, p. 365501, Sept. 2015.

[34] J. Hubbard, "Electron Correlations in Narrow Energy Bands," *Proceedings of the Royal Society of London. Series A, Mathematical and Physical Sciences*, vol. 276, no. 1365, pp. 238–257, 1963.

[35] Departement of Chemistry, "Annual Report 2018," tech. rep., DTU.

[36] G. Givaja, P. Amo-Ochoa, C. J. Gómez-García, and F. Zamora, "Electrical conductive coordination polymers," *Chem. Soc. Rev.*, vol. 41, no. 1, pp. 115–147, 2012.

[37] L. Sun, M. G. Campbell, and M. Dincă, "Electrically Conductive Porous Metal-Organic Frameworks," *Angewandte Chemie International Edition*, vol. 55, pp. 3566–3579, Mar. 2016.

[38] A. Gelessus, "Character table for point group C2h." `http://symmetry.jacobs-university.de/cgi-bin/group.cgi?group=502&option=4`. (accessed 2020-12-19).

[39] V. K. Pecharsky and P. Y. Zavalij, *Fundamentals of Powder Diffraction and Structural Characterization of Materials*. Boston, MA: Springer US, 2009.

[40] H. Bruus and K. Flensberg, *Many-Body Quantum Theory in Condensed Matter Physics: An Introduction*. Oxford university press, 2004.

Appendices

Appendix A

Estimate of Bond Integrals

The bond integrals between two neighbouring orbitals can be estimated following the example given below. We will focus on a p_x orbital located at $x = -d/2$ and a $d_{x^2-y^2}$ orbital located at $x = d/2$. Thus, the distance between the center of the two orbitals is denoted d, see **Fig. A.1**. In this example only the σ-bond will be calculated. The wavefunctions for the relevant orbitals, if they were located at the origin, are given by

$$\psi_{3d_{x^2-y^2}} = R_{3d}\sqrt{\frac{15}{4}}\frac{(x^2-y^2)}{r^2}\frac{1}{\sqrt{4\pi}}, \tag{A.1}$$

$$\psi_{3p_x} = R_{3p}\frac{\sqrt{3}x}{r}\frac{1}{4\pi}, \tag{A.2}$$

with

$$R_{3d} = \frac{1}{9\sqrt{30}}\rho^2 Z^{3/2} e^{-\rho/2}, \tag{A.3}$$

$$R_{3p} = \frac{1}{9\sqrt{16}}\rho(4-\rho) Z^{3/2} e^{-\rho/2}. \tag{A.4}$$

Here, we have defined $\rho = \frac{2Zr}{n}$, where Z is the effective nuclear charge for the orbital in interest located in the atom, r is the radius, and n is the principal quantum number. To simplify the following calculations, the coordinate transformation, that let $x \to z$, $x \to -z$ and let y remain unchanged, is performed. Further, the wavefunctions are shifted to place the d- and p-orbitals at x equal to $d/2$ and $-d/2$, respectively. Thus,

Fig. A.1: Spin densities of the p_x orbital (left) and the $d_{x^2-y^2}$ orbital (right).

the wavefunctions become

$$\psi_{3d_{x^2-y^2}} = \frac{R_{3d}}{4}\sqrt{\frac{15}{\pi}}\frac{\left(z-\frac{d}{2}\right)^2 - y^2}{r_d^2}, \tag{A.5}$$

$$\psi_{3p_x} = R_{3p}\sqrt{\frac{3}{4\pi}}\frac{z+\frac{d}{2}}{r_p}, \tag{A.6}$$

where we have defined

$$r_d = \sqrt{x^2+y^2+\left(z-\frac{d}{2}\right)^2}, \tag{A.7}$$

$$r_p = \sqrt{x^2+y^2+\left(z+\frac{d}{2}\right)^2}. \tag{A.8}$$

Note that the ρ's in the radial parts of the wavefunctions are now a function of r_d and r_p for the d-orbital and the p-orbital, respectively. The overlap between the two orbitals can now be obtained,

$$\langle\psi_{3p_x}|\psi_{3d_{x^2-y^2}}\rangle = \frac{Z_p^{5/2}Z_d^{7/2}}{4374\sqrt{\pi}}\int d\mathbf{r}\left(4-\frac{2Z_pr_p}{3}\right)\left(z+\frac{d}{2}\right)e^{-\frac{Z_pr_p}{3}}\left[\left(z-\frac{d}{2}\right)^2-y^2\right]e^{-\frac{Z_dr_d}{3}} \tag{A.9}$$

These integrals can be evaluated in spherical coordinates, so the transformation

$$z = r\cos\theta, \quad y = r\sin\theta\sin\phi \tag{A.10}$$

$$r_p = \sqrt{r^2+\left(\frac{d}{2}\right)^2+\frac{d}{2}r\cos\theta} \tag{A.11}$$

$$r_d = \sqrt{r^2+\left(\frac{d}{2}\right)^2-\frac{d}{2}r\cos\theta}, \tag{A.12}$$

is performed. Thus, the overlap can be written as

$$\langle\psi_{3p_x}|\psi_{3d_{x^2-y^2}}\rangle = A\int dr d\theta d\phi\, r^2\sin\theta\left(4-\frac{2Z_pr_p}{3}\right)\left(r\cos\theta+\frac{d}{2}\right) \tag{A.13}$$

$$e^{-\frac{Z_pr_p}{3}}\left[\left(r\cos\theta-\frac{d}{2}\right)^2-r^2\sin\theta^2\sin\phi^2\right]e^{-\frac{Z_dr_d}{3}}. \tag{A.14}$$

This integral can not be solved trivially, though this can be split into a sum of eight integrals. These can be solved numerically individually using the substitution $\mu = \cos\theta$ such that

$$\int_0^\pi d\theta\sin\theta = \int_{-1}^1 d\mu. \tag{A.15}$$

A similar approach can be used to obtain the remaining bond integrals.

Appendix B

Expansion Around the K-point

The expansion around the **K**-point is not as trivial as the **Γ**-point, and it has proved to be convenient to change coordinate system to be able to diagonalize the Hamiltonian in this point. Thus, in this section we let $x \to y$ and $y \to -x$ compared to the coordinate-system described in **section 5.3.1**.

In addition to changing coordinate system, it is convenient to use another basis, namely $\{d_{z^2}, d_{x^2-y^2}, d_{xy}, d_{zx}, d_{yz}, p_x^t, p_y^t, p_z^t, p_x^b, p_y^b, p_z^b\}$. The eigenvector can now be written in terms of the amplitudes as

$$\Psi^T = (\alpha_5, \alpha_4, \alpha_1, \alpha_3, \alpha_2, \tau_1, \tau_2, \tau_3, \beta_1, \beta_2, \beta_3). \tag{B.1}$$

In this basis and coordinate system the hopping matrices become

$$\begin{aligned}
t^t &= \begin{bmatrix} 0 & t_{12}^t & t_{13}^t \\ 0 & t_{22}^t & t_{23}^t \\ t_{31}^t & 0 & 0 \\ t_{41}^t & 0 & 0 \\ 0 & t_{52}^t & t_{53}^t \end{bmatrix}, \quad t^b = \begin{bmatrix} 0 & t_{12}^t & -t_{13}^t \\ 0 & t_{22}^t & -t_{23}^t \\ t_{31}^t & 0 & 0 \\ -t_{41}^t & 0 & 0 \\ 0 & -t_{52}^t & t_{53}^t \end{bmatrix}, \\
t^{l,t} &= \begin{bmatrix} t_{11}^{l,t} & t_{12}^{l,t} & t_{13}^{l,t} \\ t_{21}^{l,t} & t_{22}^{l,t} & t_{23}^{l,t} \\ t_{31}^{l,t} & t_{32}^{l,t} & t_{33}^{l,t} \\ t_{41}^{l,t} & t_{42}^{l,t} & t_{43}^{l,t} \\ t_{51}^{l,t} & t_{52}^{l,t} & t_{53}^{l,t} \end{bmatrix}, \quad t^{l,b} = \begin{bmatrix} t_{11}^{l,t} & t_{12}^{l,t} & -t_{13}^{l,t} \\ t_{21}^{l,t} & t_{22}^{l,t} & -t_{23}^{l,t} \\ t_{31}^{l,t} & t_{32}^{l,t} & -t_{33}^{l,t} \\ -t_{41}^{l,t} & -t_{42}^{l,t} & t_{43}^{l,t} \\ -t_{51}^{l,t} & -t_{52}^{l,t} & t_{53}^{l,t} \end{bmatrix}, \\
t^{r,t} &= \begin{bmatrix} -t_{11}^{l,t} & t_{12}^{l,t} & t_{13}^{l,t} \\ -t_{21}^{l,t} & t_{22}^{l,t} & t_{23}^{l,t} \\ t_{31}^{l,t} & -t_{32}^{l,t} & -t_{33}^{l,t} \\ t_{41}^{l,t} & -t_{42}^{l,t} & -t_{43}^{l,t} \\ -t_{51}^{l,t} & t_{52}^{l,t} & t_{53}^{l,t} \end{bmatrix}, \quad t^{r,b} = \begin{bmatrix} -t_{11}^{l,t} & t_{12}^{l,t} & -t_{13}^{l,t} \\ -t_{21}^{l,t} & t_{22}^{l,t} & -t_{23}^{l,t} \\ t_{31}^{l,t} & -t_{32}^{l,t} & t_{33}^{l,t} \\ -t_{41}^{l,t} & t_{42}^{l,t} & -t_{43}^{l,t} \\ t_{51}^{l,t} & -t_{52}^{l,t} & t_{53}^{l,t} \end{bmatrix}.
\end{aligned} \tag{B.2}$$

In this basis the **K**-point has the componenets $k_x = \frac{2\pi}{3a}$ and $k_y = \frac{-2\pi}{\sqrt{3}a}$, which means that $z_1 = -e^{i\pi/3}$ and $c_1 = c_2 = c_{12} = -\frac{1}{2}$. Thus, in this case, the components of the Hamiltonian is

$$T^t = t^t - e^{-i\pi/3}t^{l,t} - e^{i\pi/3}t^{r,t} \quad , \quad T^b = t^b - e^{-i\pi/3}t^{l,b} - e^{i\pi/3}t^{r,b}. \tag{B.3}$$

Following the same procedure as in **section 5.3.1** we can split the Hamiltonian in an even part and a odd part. Making use of the two identities

$$-e^{-i\pi/3} + e^{i\pi/3} = i\sqrt{3} \quad \text{and} \quad -e^{-i\pi/3} + e^{i\pi/3} = 1, \tag{B.4}$$

we get that $T^{E,O}$ and $T^{O,E}$, in the **K**-point, simplifies to

$$T^{E,O}_{\mathbf{K}} = \sqrt{2}\begin{bmatrix} i\sqrt{3}t^{l,t}_{11} & t^{t}_{12} - t^{l,t}_{12} & 0 \\ i\sqrt{3}t^{l,t}_{21} & t^{t}_{22} - t^{l,t}_{22} & t^{t}_{23} - t^{l,t}_{23} \\ t^{t}_{31} - t^{l,t}_{31} & i\sqrt{3}t^{l,t}_{32} & i\sqrt{3}t^{l,t}_{33} \end{bmatrix} \tag{B.5}$$

and

$$T^{O,E}_{\mathbf{K}} = \sqrt{2}\begin{bmatrix} t^{t}_{41} - t^{l,t}_{41} & i\sqrt{3}t^{l,t}_{42} & i\sqrt{3}t^{l,t}_{43} \\ i\sqrt{3}t^{l,t}_{51} & t^{t}_{52} - t^{l,t}_{52} & t^{t}_{53} - t^{l,t}_{53} \end{bmatrix}. \tag{B.6}$$

Now the Hamiltonian can be diagonalized by the chiral transformation

$$\alpha_{M_2} = \frac{\alpha_2 - i\alpha_3}{\sqrt{2}}, \quad \alpha_{P_2} = \frac{\alpha_2 + i\alpha_3}{\sqrt{2}}, \quad \alpha_{M_1} = \frac{\alpha_4 - i\alpha_5}{\sqrt{2}}, \quad \alpha_{P_1} = \frac{\alpha_4 + i\alpha_5}{\sqrt{2}}, \tag{B.7}$$

$$\theta_M = \frac{\theta_1 - i\theta_2}{\sqrt{2}}, \quad \theta_P = \frac{\theta_1 + i\theta_2}{\sqrt{2}}, \quad \phi_M = \frac{\phi_1 - i\phi_2}{\sqrt{2}}, \quad \phi_P = \frac{\phi_1 + i\phi_2}{\sqrt{2}}. \tag{B.8}$$

α_1, θ_3 and ϕ_3 remain unchanged. Thus, we now have the eigenvector

$$\psi^T = (\alpha_1, \alpha_{M_2}, \alpha_{P_2}, \theta_P, \theta_M, \phi_3, \alpha_{M_1}, \alpha_{P_1}, \phi_P, \phi_R, \theta_3). \tag{B.9}$$

Using the Slater Koster decomposition, many elements reduce to zero, and as in the expansion around the **Γ**-point, the problem reduces to five 2x2 matrices and one 1x1 matrix, given by

$$\begin{aligned}
\{\alpha_1, \theta_M\}: &\quad \begin{bmatrix} \xi_d & i(K_{11} - K_{12}) \\ -i(K_{11} - K_{12}) & \xi_p \end{bmatrix}, \\
\{\alpha_{M_2}, \theta_P\}: &\quad \begin{bmatrix} \xi_d & i(K_{21} - K_{31} + K_{22} + K_{32})/\sqrt{2} \\ -i(K_{21} - K_{31} + K_{22} + K_{32})/\sqrt{2} & \xi_p \end{bmatrix}, \\
\{\alpha_{P_2}, \phi_3\}: &\quad \begin{bmatrix} \xi_d & K_{23} - K_{33} \\ K_{23} - K_{33} & \xi_p \end{bmatrix}, \\
\{\alpha_{P_1}, \phi_P\}: &\quad \begin{bmatrix} \xi_d & (K_{41} - K_{51} + K_{42} - K_{52})/\sqrt{2} \\ (K_{41} - K_{51} + K_{42} - K_{52})/\sqrt{2} & \xi_p \end{bmatrix}, \\
\{\alpha_{M_1}, \theta_3\}: &\quad \begin{bmatrix} \xi_d & i(K_{43} - K_{53}) \\ -i(K_{43} - K_{53}) & \xi_p \end{bmatrix}, \\
\{\phi_M\}: &\quad \begin{bmatrix} \xi_p \end{bmatrix}.
\end{aligned}$$

Here, we have defined the following identities

$$K_{11} = \sqrt{3}t^{l,t}_{11}, \quad K_{12} = t^{t}_{12} - t^{l,t}_{12}, \tag{B.10}$$

$$K_{21} = \sqrt{3}t^{l,t}_{21}, \quad K_{22} = t^{t}_{22} - t^{l,t}_{22}, \quad K_{23} = t^{t}_{23} - t^{l,t}_{23}, \tag{B.11}$$

$$K_{31} = t^{t}_{31} - t^{l,t}_{31}, \quad K_{32} = \sqrt{3}t^{l,t}_{32}, \quad K_{33} = \sqrt{3}t^{l,t}_{33}, \tag{B.12}$$

$$K_{41} = t^{t}_{41} - t^{l,t}_{41}, \quad K_{42} = \sqrt{3}t^{l,t}_{42}, \quad K_{43} = \sqrt{3}t^{l,t}_{43}, \tag{B.13}$$

$$K_{51} = \sqrt{3}t^{l,t}_{51}, \quad K_{52} = t^{t}_{52} - t^{l,t}_{52}, \quad K_{53} = t^{t}_{53} - t^{l,t}_{53}. \tag{B.14}$$

These are trivial to diagonalize. The analytical expressions yield identical results to the numerical solutions for the **K**-point obtained previously.

Appendix C

$CrCl_2(pyz)_2$ Described by the Curie-Weiss Law

In this appendix a brief investigation of the magnetic properties of $CrCl_2(pyz)_2$ is performed. The Curie-Weiss law is given by

$$\chi = \frac{C}{T - T_c}, \tag{C.1}$$

with the Curie constant

$$C = \frac{\mu_0 \mu_B^2}{3k_b} n g^2 J(J+1) \tag{C.2}$$

in SI units. μ_B denotes the Bohr magneton, μ_0 is vacuum permeability, n the number of magnetic atoms per unit volume, k_B the Boltzmann constant, and $J = L + S$ is the angular momentum quantum number. In this case $L = 0$. Note, that to get Eq. (C.2) in cgs units, to be able to compare with the results in [4]), this must be multiplied with $\frac{10^6 N_A}{4\pi}$, where N_A is Avogrado's constant. Setting $T_c = 0$, $\chi T(J)$ at $T = 400$ K can be obtained for three distinct J's,

$$\chi T(1) = 1.00\text{cm}^3\text{Kmol}^{-1}, \quad \chi T(3/2) = 1.88\text{cm}^3\text{Kmol}^{-1}, \quad \chi T(2) = 3.01\text{cm}^3\text{Kmol}^{-1}.$$

This is in accordance with numbers presented in [4]. The measured value at 400 K is $2.7\text{cm}^3\text{Kmol}^{-1}$, and for this reason could indicate that $J = S = 2$, though the theoretical prediction is greater than the measured value. As shown in **section 6.2**, an ordering temperature at ~ 55 K is observed. Thus, setting $T_c = 55$ K $\chi T(J)$ at 400 K is found to be

$$\chi T(1) = 1.16\text{cm}^3\text{Kmol}^{-1}, \quad \chi T(3/2) = 2.18\text{cm}^3\text{Kmol}^{-1}, \quad \chi T(2) = 3.49\text{cm}^3\text{Kmol}^{-1}.$$

This could suggest that $S = 3/2$ is also a possible spin configuration for the Cr-ions. Due to the strong magnetic interactions and strong $\pi - d$ conjugation, this method is not suitable to describe the magnetic susceptibility-temperature product.

Fitting the Curie-Weiss law to the χT data, Pedersen et al. have obtained, for datapoints above the ordering temperature confirms that this is not describing the data well. **Fig. C.1** (a) depict the magnetic susceptibility temperature product data along with a fit of the Curie-Weiss law multiplied with the temperature. The data is collected from Pedersen et al. [4] and the fit is performed using the χ^2 method. The fit yields a Curie constant of $C = 10.32 \pm 1.6$ and a Curie temperature of $T_C = 52.1 \pm 0.58$ K. **Fig. C.1** (b) shows a log-log plot of the same data excluding the first five points. Here, it is clearly observed that the Curie-Weiss model does not fit the data well.

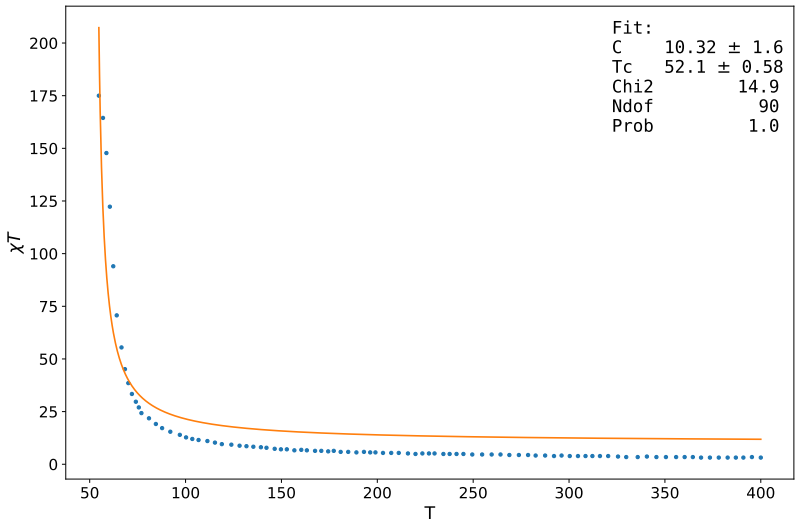

(a)

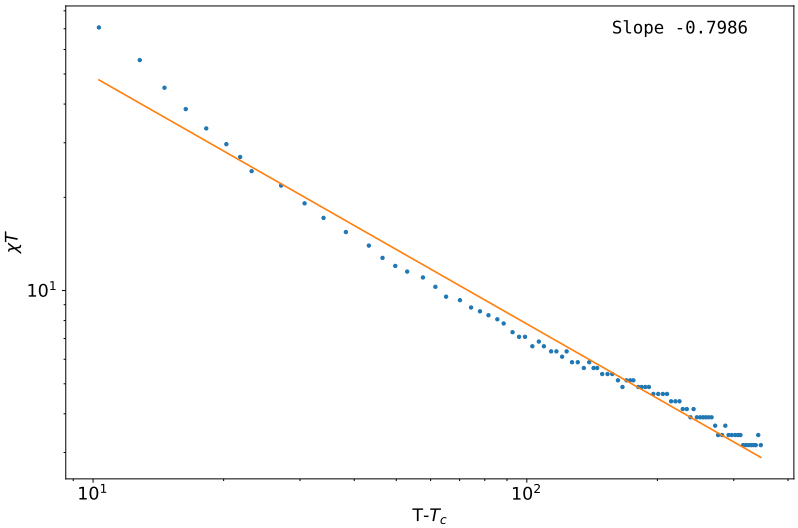

(b)

Fig. C.1: (a) χT data collected from Pedersen et al. [4] together with a fit of the Curie-Weiss law in Eq. (C.1). (b) Log-log plot of χT data together with fit. The ten first datapoints has been excluded.

Appendix D

Supplementary Figures from Pedersen et al. [4]

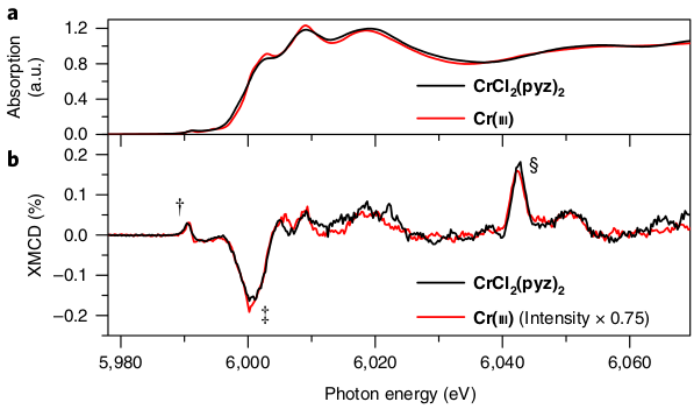

Fig. D.1: **a** Normalized XAS spectra of $CrCl_2(pyz)_2$ and Cr(III). **b** XMCD spectra shown as the percentage of the peak at the edge. The data was obtained at a temperature at 3 K with a magnetic field of 17 T. † illustrates the pre-dge, ‡ the edge and § marks multi-electron excitations.

Appendix E

Spin-Matrices used in Numerical Calculations

The following matrices are given in the basis in Eq. (6.33).

$$\mathbf{S}_1^z + \mathbf{S}_2^z + \mathbf{S}_3^z = \begin{bmatrix}
0 & 0 & 0 & 0 & 0 & 0 & 0 & 0 & 0 & 0 & 0 & 0 & 0 & 0 & 0 & 0 & 0 & 0 & 0 & 0 & 0 & 0 & 0 & 0 & 0 & 0 & 0 & 0 \\
0 & 0 & 0 & 0 & 0 & 0 & 0 & 0 & 0 & 0 & 0 & 0 & 0 & 0 & 0 & 0 & 0 & 0 & 0 & 0 & 0 & 0 & 0 & 0 & 0 & 0 & 0 & 0 \\
0 & 0 & 0 & 0 & 0 & 0 & 0 & 0 & 0 & 0 & 0 & 0 & 0 & 0 & 0 & 0 & 0 & 0 & \frac{1}{2} & 0 & 0 & 0 & 0 & 0 & 0 & 0 & 0 & 0 \\
0 & 0 & 0 & 0 & 0 & 0 & 0 & 0 & 0 & 0 & 0 & 0 & 0 & 0 & 0 & 0 & 0 & 0 & 0 & 0 & 0 & 0 & 0 & 0 & 0 & 0 & 0 & 0 \\
0 & 0 & 0 & 0 & 0 & 0 & 0 & 0 & 0 & 0 & 0 & 0 & 0 & 0 & 0 & 0 & 0 & 0 & 0 & \frac{1}{2} & 0 & 0 & 0 & 0 & 0 & 0 & 0 & 0 \\
0 & 0 & 0 & 0 & 0 & 0 & 0 & 0 & 0 & 0 & 0 & 0 & 0 & 0 & 0 & 0 & 0 & 0 & 0 & 0 & \frac{1}{2} & 0 & 0 & 0 & 0 & 0 & 0 & 0 \\
0 & 0 & 0 & 0 & 0 & 0 & 0 & 0 & 0 & 0 & 0 & 0 & 0 & 0 & 0 & 0 & 0 & 0 & 0 & 0 & 0 & 0 & 0 & 0 & 0 & 0 & 0 & 0 \\
0 & 0 & 0 & 0 & 0 & 0 & 0 & 0 & 0 & 0 & 0 & 0 & 0 & 0 & 0 & 0 & 0 & 0 & 0 & 0 & 0 & 0 & 0 & 0 & 0 & 0 & 0 & 0 \\
0 & 0 & 0 & 0 & 0 & 0 & 0 & 0 & 0 & 0 & 0 & 0 & 0 & 0 & 0 & 0 & 0 & 0 & 0 & 0 & 0 & 0 & 0 & 0 & 0 & 0 & 0 & 0 \\
0 & 0 & 0 & 0 & 0 & 0 & 0 & 0 & 0 & 0 & 0 & 0 & 0 & 0 & 0 & 0 & 0 & 0 & 0 & 0 & 0 & 0 & 0 & 0 & 0 & 0 & 0 & 0 \\
0 & 0 & 0 & 0 & 0 & 0 & 0 & 0 & 0 & 0 & 0 & 0 & 0 & 0 & 0 & 0 & 0 & 0 & 0 & 0 & 0 & 0 & 0 & 0 & 0 & 0 & 0 & 0 \\
0 & 0 & 0 & 0 & 0 & 0 & 0 & 0 & 0 & 0 & -1 & 0 & 0 & 0 & 0 & 0 & 0 & 0 & 0 & 0 & 0 & 0 & 0 & 0 & 0 & 0 & 0 & 0 \\
0 & 0 & 0 & 0 & 0 & 0 & 0 & 0 & 0 & 0 & 0 & -1 & 0 & 0 & 0 & 0 & 0 & 0 & 0 & 0 & 0 & 0 & 0 & 0 & 0 & 0 & 0 & 0 \\
0 & 0 & 0 & 0 & 0 & 0 & 0 & 0 & 0 & 0 & 0 & 0 & \frac{-1}{2} & 0 & 0 & 0 & 0 & 0 & 0 & 0 & 0 & 0 & 0 & 0 & 0 & 0 & 0 & 0 \\
0 & 0 & 0 & 0 & 0 & 0 & 0 & 0 & 0 & 0 & 0 & 0 & 0 & -1 & 0 & 0 & 0 & 0 & 0 & 0 & 0 & 0 & 0 & 0 & 0 & 0 & 0 & 0 \\
0 & 0 & 0 & 0 & 0 & 0 & 0 & 0 & 0 & 0 & 0 & 0 & 0 & 0 & \frac{-1}{2} & 0 & 0 & 0 & 0 & 0 & 0 & 0 & 0 & 0 & 0 & 0 & 0 & 0 \\
0 & 0 & 0 & 0 & 0 & 0 & 0 & 0 & 0 & 0 & 0 & 0 & 0 & 0 & 0 & \frac{-1}{2} & 0 & 0 & 0 & 0 & 0 & 0 & 0 & 0 & 0 & 0 & 0 & 0 \\
0 & 0 & 0 & 0 & 0 & 0 & 0 & 0 & 0 & 0 & 0 & 0 & 0 & 0 & 0 & 0 & 0 & 0 & 0 & 0 & 0 & 0 & 0 & 0 & 0 & 0 & 0 & 0 \\
0 & 0 & 0 & 0 & 0 & 0 & 0 & 0 & 0 & 0 & 0 & 0 & 0 & 0 & 0 & 0 & 0 & 0 & 0 & 0 & 0 & 0 & 0 & 0 & 0 & 0 & 0 & 0 \\
0 & 0 & \frac{1}{2} & 0 & 0 & 0 & 0 & 0 & 0 & 0 & 0 & 0 & 0 & 0 & 0 & 0 & 0 & 0 & 0 & 0 & 0 & 0 & 0 & 0 & 0 & 0 & 0 & 0 \\
0 & 0 & 0 & 0 & 0 & 0 & 0 & 0 & 0 & 0 & 0 & 0 & 0 & 0 & 0 & 0 & 0 & 0 & 0 & 0 & 0 & 0 & 0 & 0 & 0 & 0 & 0 & 0 \\
0 & 0 & 0 & 0 & \frac{1}{2} & 0 & 0 & 0 & 0 & 0 & 0 & 0 & 0 & 0 & 0 & 0 & 0 & 0 & 0 & 0 & 0 & 0 & 0 & 0 & 0 & 0 & 0 & 0 \\
0 & 0 & 0 & 0 & 0 & \frac{1}{2} & 0 & 0 & 0 & 0 & 0 & 0 & 0 & 0 & 0 & 0 & 0 & 0 & 0 & 0 & 0 & 0 & 0 & 0 & 0 & 0 & 0 & 0 \\
0 & 0 & 0 & 0 & 0 & 0 & 0 & 0 & 0 & 0 & 0 & 0 & 0 & 0 & 0 & 0 & 0 & 0 & 0 & 0 & 0 & 1 & 0 & 0 & 0 & 0 & 0 & 0 \\
0 & 0 & 0 & 0 & 0 & 0 & 0 & 0 & 0 & 0 & 0 & 0 & 0 & 0 & 0 & 0 & 0 & 0 & 0 & 0 & 0 & 0 & 1 & 0 & 0 & 0 & 0 & 0 \\
0 & 0 & 0 & 0 & 0 & 0 & 0 & 0 & 0 & 0 & 0 & 0 & 0 & 0 & 0 & 0 & 0 & 0 & 0 & 0 & 0 & 0 & 0 & \frac{1}{2} & 0 & 0 & 0 & 0 \\
0 & 0 & 0 & 0 & 0 & 0 & 0 & 0 & 0 & 0 & 0 & 0 & 0 & 0 & 0 & 0 & 0 & 0 & 0 & 0 & 0 & 0 & 0 & 0 & 1 & 0 & 0 & 0 \\
0 & 0 & 0 & 0 & 0 & 0 & 0 & 0 & 0 & 0 & 0 & 0 & 0 & 0 & 0 & 0 & 0 & 0 & 0 & 0 & 0 & 0 & 0 & 0 & 0 & \frac{1}{2} & 0 & 0 \\
0 & 0 & 0 & 0 & 0 & 0 & 0 & 0 & 0 & 0 & 0 & 0 & 0 & 0 & 0 & 0 & 0 & 0 & 0 & 0 & 0 & 0 & 0 & 0 & 0 & 0 & \frac{1}{2} & 0 \\
0 & 0 & 0 & 0 & 0 & 0 & 0 & 0 & 0 & 0 & 0 & 0 & 0 & 0 & 0 & 0 & 0 & 0 & 0 & 0 & 0 & 0 & 0 & 0 & 0 & 0 & 0 & \frac{1}{2}
\end{bmatrix}$$

$$\mathbf{S}_2^z + \mathbf{S}_3^z + \mathbf{S}_4^z = \begin{bmatrix}
0 & 0 & 0 & 0 & 0 & 0 & 0 & 0 & 0 & 0 & 0 & 0 & 0 & 0 & 0 & 0 & 0 & \frac{1}{2} & 0 & 0 & 0 & 0 & 0 & 0 & 0 & 0 & 0 & 0 \\
0 & 0 & 0 & 0 & 0 & 0 & 0 & 0 & 0 & 0 & 0 & 0 & 0 & 0 & 0 & 0 & 0 & 0 & 0 & 0 & 0 & 0 & 0 & 0 & 0 & 0 & 0 & 0 \\
0 & 0 & 0 & 0 & 0 & 0 & 0 & 0 & 0 & 0 & 0 & 0 & 0 & 0 & 0 & 0 & 0 & 0 & 0 & 0 & 0 & 0 & 0 & 0 & 0 & 0 & 0 & 0 \\
0 & 0 & 0 & 0 & 0 & 0 & 0 & 0 & 0 & 0 & 0 & 0 & 0 & 0 & 0 & 0 & 0 & 0 & \frac{1}{2} & 0 & 0 & 0 & 0 & 0 & 0 & 0 & 0 & 0 \\
0 & 0 & 0 & 0 & 0 & 0 & 0 & 0 & 0 & 0 & 0 & 0 & 0 & 0 & 0 & 0 & 0 & 0 & 0 & 0 & 0 & 0 & 0 & 0 & 0 & 0 & 0 & 0 \\
0 & 0 & 0 & 0 & 0 & 0 & 0 & 0 & 0 & 0 & 0 & 0 & 0 & 0 & 0 & 0 & 0 & 0 & 0 & \frac{1}{2} & 0 & 0 & 0 & 0 & 0 & 0 & 0 & 0 \\
0 & 0 & 0 & 0 & 0 & 0 & 0 & 0 & 0 & 0 & 0 & 0 & 0 & 0 & 0 & 0 & 0 & 0 & 0 & 0 & 0 & 0 & 0 & 0 & 0 & 0 & 0 & 0 \\
0 & 0 & 0 & 0 & 0 & 0 & 0 & 0 & 0 & 0 & 0 & 0 & 0 & 0 & 0 & 0 & 0 & 0 & 0 & 0 & 0 & 0 & 0 & 0 & 0 & 0 & 0 & 0 \\
0 & 0 & 0 & 0 & 0 & 0 & 0 & 0 & 0 & 0 & 0 & 0 & 0 & 0 & 0 & 0 & 0 & 0 & 0 & 0 & 0 & 0 & 0 & 0 & 0 & 0 & 0 & 0 \\
0 & 0 & 0 & 0 & 0 & 0 & 0 & 0 & 0 & 0 & 0 & 0 & 0 & 0 & 0 & 0 & 0 & 0 & 0 & 0 & 0 & 0 & 0 & 0 & 0 & 0 & 0 & 0 \\
0 & 0 & 0 & 0 & 0 & 0 & 0 & 0 & 0 & 0 & 0 & 0 & 0 & 0 & 0 & 0 & 0 & 0 & 0 & 0 & 0 & 0 & 0 & 0 & 0 & 0 & 0 & 0 \\
0 & 0 & 0 & 0 & 0 & 0 & 0 & 0 & 0 & 0 & 0 & 0 & 0 & 0 & 0 & 0 & 0 & 0 & 0 & 0 & 0 & 0 & 0 & 0 & 0 & 0 & 0 & 0 \\
0 & 0 & 0 & 0 & 0 & 0 & 0 & 0 & 0 & 0 & 0 & 0 & 0 & 0 & 0 & 0 & 0 & 0 & 0 & 0 & 0 & 0 & 0 & 0 & 0 & 0 & 0 & 0 \\
0 & 0 & 0 & 0 & 0 & 0 & 0 & 0 & 0 & 0 & 0 & 0 & 0 & 0 & 0 & 0 & 0 & 0 & 0 & 0 & 0 & 0 & 0 & 0 & 0 & 0 & 0 & 0 \\
0 & 0 & 0 & 0 & 0 & 0 & 0 & 0 & 0 & 0 & 0 & 0 & 0 & 0 & 0 & 0 & 0 & 0 & 0 & 0 & 0 & 0 & 0 & 0 & 0 & 0 & 0 & 0 \\
0 & 0 & 0 & 0 & 0 & 0 & 0 & 0 & 0 & 0 & 0 & 0 & 0 & 0 & 0 & 0 & 0 & 0 & 0 & 0 & 0 & 0 & 0 & 0 & 0 & 0 & 0 & 0 \\
0 & 0 & 0 & 0 & 0 & 0 & 0 & 0 & 0 & 0 & 0 & 0 & 0 & 0 & 0 & 0 & 0 & 0 & 0 & 0 & 0 & 0 & 0 & 0 & 0 & 0 & 0 & 0 \\
0 & 0 & 0 & 0 & 0 & 0 & 0 & 0 & 0 & 0 & 0 & 0 & 0 & 0 & 0 & 0 & 0 & 0 & 0 & 0 & 0 & 0 & 0 & 0 & 0 & 0 & 0 & 0 \\
0 & 0 & 0 & 0 & 0 & 0 & 0 & 0 & 0 & 0 & 0 & 0 & 0 & 0 & 0 & 0 & 0 & 0 & 0 & 0 & 0 & 0 & 0 & 0 & 0 & 0 & 0 & 0 \\
0 & 0 & 0 & 0 & 0 & 0 & 0 & 0 & 0 & 0 & 0 & 0 & 0 & 0 & 0 & 0 & 0 & 0 & 0 & 0 & 0 & 0 & 0 & 0 & 0 & 0 & 0 & 0 \\
0 & 0 & 0 & 0 & 0 & 0 & 0 & 0 & 0 & 0 & 0 & 0 & 0 & 0 & 0 & 0 & 0 & 0 & 0 & 0 & 0 & 0 & 0 & 0 & 0 & 0 & 0 & 0 \\
0 & 0 & 0 & 0 & 0 & 0 & 0 & 0 & 0 & 0 & 0 & 0 & 0 & 0 & 0 & 0 & 0 & 0 & 0 & 0 & 0 & 0 & 0 & 0 & 0 & 0 & 0 & 0 \\
0 & 0 & 0 & 0 & 0 & 0 & 0 & 0 & 0 & 0 & 0 & 0 & 0 & 0 & 0 & 0 & 0 & 0 & 0 & 0 & 0 & 0 & 0 & 0 & 0 & 0 & 0 & 0 \\
0 & 0 & 0 & 0 & 0 & 0 & 0 & 0 & 0 & 0 & 0 & 0 & 0 & 0 & 0 & 0 & 0 & 0 & 0 & 0 & 0 & 0 & 0 & 0 & 0 & 0 & 0 & 0 \\
0 & 0 & 0 & 0 & 0 & 0 & 0 & 0 & 0 & 0 & 0 & 0 & 0 & 0 & 0 & 0 & 0 & 0 & 0 & 0 & 0 & 0 & 0 & 0 & 0 & 0 & 0 & 0 \\
0 & 0 & 0 & 0 & 0 & 0 & 0 & 0 & 0 & 0 & 0 & 0 & 0 & 0 & 0 & 0 & 0 & 0 & 0 & 0 & 0 & 0 & 0 & 0 & 0 & 0 & 0 & 0 \\
0 & 0 & 0 & 0 & 0 & 0 & 0 & 0 & 0 & 0 & 0 & 0 & 0 & 0 & 0 & 0 & 0 & 0 & 0 & 0 & 0 & 0 & 0 & 0 & 0 & 0 & 0 & 0 \\
0 & 0 & 0 & 0 & 0 & 0 & 0 & 0 & 0 & 0 & 0 & 0 & 0 & 0 & 0 & 0 & 0 & 0 & 0 & 0 & 0 & 0 & 0 & 0 & 0 & 0 & 0 & 0 \\
0 & 0 & 0 & 0 & 0 & 0 & 0 & 0 & 0 & 0 & 0 & 0 & 0 & 0 & 0 & 0 & 0 & 0 & 0 & 0 & 0 & 0 & 0 & 0 & 0 & 0 & 0 & 0 \\
0 & 0 & 0 & 0 & 0 & 0 & 0 & 0 & 0 & 0 & 0 & 0 & 0 & 0 & 0 & 0 & 0 & 0 & 0 & 0 & 0 & 0 & 0 & 0 & 0 & 0 & 0 & 0 \\
0 & 0 & 0 & 0 & 0 & 0 & 0 & 0 & 0 & 0 & 0 & 0 & 0 & 0 & 0 & 0 & 0 & 0 & 0 & 0 & 0 & 0 & 0 & 0 & 0 & 0 & 0 & 0 \\
0 & 0 & 0 & 0 & 0 & 0 & 0 & 0 & 0 & 0 & 0 & 0 & 0 & 0 & 0 & 0 & 0 & 0 & 0 & 0 & 0 & 0 & 0 & 0 & 0 & 0 & 0 & 0 \\
0 & 0 & 0 & 0 & 0 & 0 & 0 & 0 & 0 & 0 & 0 & 0 & 0 & 0 & 0 & 0 & 0 & 0 & 0 & 0 & 0 & 0 & 0 & 0 & 0 & 0 & 0 & 0 \\
0 & 0 & 0 & 0 & 0 & 0 & 0 & 0 & 0 & 0 & 0 & 0 & 0 & 0 & 0 & 0 & 0 & 0 & 0 & 0 & 0 & 0 & 0 & 0 & 0 & 0 & 0 & 0 \\
0 & 0 & 0 & 0 & 0 & 0 & 0 & 0 & 0 & 0 & 0 & 0 & 0 & 0 & 0 & 0 & 0 & 0 & 0 & 0 & 0 & 0 & 0 & 0 & 0 & 0 & 0 & 0 \\
0 & 0 & 0 & 0 & 0 & 0 & 0 & 0 & 0 & 0 & 0 & 0 & 0 & 0 & 0 & 0 & 0 & 0 & 0 & 0 & 0 & 0 & 0 & 0 & 0 & 0 & 0 & 0 \\
0 & 0 & 0 & 0 & 0 & 0 & 0 & 0 & 0 & 0 & 0 & 0 & 0 & 0 & 0 & 0 & 0 & 0 & 0 & 0 & 0 & 0 & 0 & 0 & 0 & 0 & 0 & 0 \\
0 & 0 & 0 & 0 & 0 & 0 & 0 & 0 & 0 & 0 & 0 & 0 & 0 & 0 & 0 & 0 & 0 & 0 & 0 & 0 & 0 & 0 & 0 & 0 & 0 & 0 & 0 & 0 \\
0 & 0 & 0 & 0 & 0 & 0 & 0 & 0 & 0 & 0 & 0 & 0 & 0 & 0 & 0 & 0 & 0 & 0 & 0 & 0 & 0 & 0 & 0 & 0 & 0 & 0 & 0 & 0 \\
0 & 0 & 0 & 0 & 0 & 0 & 0 & 0 & 0 & 0 & 0 & 0 & 0 & 0 & 0 & 0 & 0 & 0 & 0 & 0 & 0 & 0 & 0 & 0 & 0 & 0 & 0 & 0 \\
0 & 0 & 0 & 0 & 0 & 0 & 0 & 0 & 0 & 0 & 0 & 0 & 0 & 0 & 0 & 0 & 0 & 0 & 0 & 0 & 0 & 0 & 0 & 0 & 0 & 0 & 0 & 0 \\
0 & 0 & 0 & 0 & 0 & 0 & 0 & 0 & 0 & 0 & 0 & 0 & 0 & 0 & 0 & 0 & 0 & 0 & 0 & 0 & 0 & 0 & 0 & 0 & 0 & 0 & 0 & 0 \\
0 & 0 & 0 & 0 & 0 & 0 & 0 & 0 & 0 & 0 & 0 & 0 & 0 & 0 & 0 & 0 & 0 & 0 & 0 & 0 & 0 & 0 & 0 & 0 & 0 & 0 & 0 & 0 \\
0 & 0 & 0 & 0 & 0 & 0 & 0 & 0 & 0 & 0 & 0 & 0 & 0 & 0 & 0 & 0 & 0 & 0 & 0 & 0 & 0 & 0 & 0 & 0 & 0 & 0 & 0 & 0 \\
0 & 0 & 0 & 0 & 0 & 0 & 0 & 0 & 0 & 0 & 0 & 0 & 0 & 0 & 0 & 0 & 0 & 0 & 0 & 0 & 0 & 0 & 0 & 0 & 0 & 0 & 0 & 0 \\
0 & 0 & 0 & 0 & 0 & 0 & 0 & 0 & 0 & 0 & 0 & 0 & 0 & 0 & 0 & 0 & 0 & 0 & 0 & 0 & 0 & 0 & 0 & 0 & 0 & 0 & 0 & 0 \\
0 & 0 & 0 & 0 & 0 & 0 & 0 & 0 & 0 & 0 & 0 & 0 & 0 & 0 & 0 & 0 & 0 & 0 & 0 & 0 & 0 & 0 & 0 & 0 & 0 & 0 & 0 & 0 \\
0 & 0 & 0 & 0 & 0 & 0 & 0 & 0 & 0 & 0 & 0 & 0 & 0 & 0 & 0 & 0 & 0 & 0 & 0 & 0 & 0 & 0 & 0 & 0 & 0 & 0 & 0 & 0 \\
0 & 0 & 0 & 0 & 0 & 0 & 0 & 0 & 0 & 0 & 0 & 0 & 0 & 0 & 0 & 0 & 0 & 0 & 0 & 0 & 0 & 0 & 0 & 0 & 0 & 0 & 0 & 0 \\
0 & 0 & 0 & 0 & 0 & 0 & 0 & 0 & 0 & 0 & 0 & 0 & 0 & 0 & 0 & 0 & 0 & 0 & 0 & 0 & 0 & 0 & 0 & 0 & 0 & 0 & 0 & 0 \\
0 & 0 & 0 & 0 & 0 & 0 & 0 & 0 & 0 & 0 & 0 & 0 & 0 & 0 & 0 & 0 & 0 & 0 & 0 & 0 & 0 & 0 & 0 & 0 & 0 & 0 & 0 & 0 \\
0 & 0 & 0 & 0 & 0 & 0 & 0 & 0 & 0 & 0 & 0 & 0 & 0 & 0 & 0 & 0 & 0 & 0 & 0 & 0 & 0 & 0 & 0 & 0 & 0 & 0 & 0 & 0 \\
0 & 0 & 0 & 0 & 0 & 0 & 0 & 0 & 0 & 0 & 0 & 0 & 0 & 0 & 0 & 0 & 0 & 0 & 0 & 0 & 0 & 0 & 0 & 0 & 0 & 0 & 0 & 0 \\
0 & 0 & 0 & 0 & 0 & 0 & 0 & 0 & 0 & 0 & 0 & 0 & 0 & 0 & 0 & 0 & 0 & 0 & 0 & 0 & 0 & 0 & 0 & 0 & 0 & 0 & 0 & 0
\end{bmatrix}$$

$$\mathbf{S}_1^+ + \mathbf{S}_2^+ + \mathbf{S}_3^+ = \begin{bmatrix}
0 & 0 & 0 & 0 & 0 & 0 & 0 & 0 & 0 & 0 & 0 & 0 & 0 & 0 & 0 & 0 & 0 & 0 & 0 & 0 & 0 & 0 & 0 & 0 & 0 & 0 & 0 & 0 \\
0 & 0 & 0 & 0 & 0 & 0 & 0 & 0 & 0 & 0 & 0 & 0 & 0 & 0 & 0 & 0 & 0 & 0 & 0 & 0 & 0 & 0 & 0 & 0 & 0 & 0 & 0 & 0 \\
0 & 0 & 0 & 0 & 0 & 0 & 0 & 0 & 0 & 0 & 0 & 0 & 0 & 0 & 0 & 0 & 0 & 0 & 0 & 0 & 0 & 0 & 0 & 0 & $-\frac{1}{\sqrt{2}}$ & 0 & 0 & 0 \\
0 & 0 & 0 & 0 & 0 & 0 & 0 & 0 & 0 & 0 & 0 & 0 & 0 & 0 & 0 & 0 & 0 & 0 & 0 & 0 & 0 & 0 & 0 & 0 & 0 & 0 & 0 & 0 \\
0 & 0 & 0 & 0 & 0 & 0 & 0 & 0 & 0 & 0 & 0 & 0 & 0 & 0 & 0 & 0 & 0 & 0 & 0 & 0 & 0 & 0 & 0 & 0 & 0 & 0 & $-\frac{1}{\sqrt{2}}$ & 0 \\
0 & 0 & 0 & 0 & 0 & 0 & 0 & 0 & 0 & 0 & 0 & 0 & 0 & 0 & 0 & 0 & 0 & 0 & 0 & 0 & 0 & 0 & 0 & 0 & 0 & 0 & 0 & $-\frac{1}{\sqrt{2}}$ \\
0 & 0 & 0 & 0 & 0 & 0 & 0 & 0 & 0 & 0 & 0 & 0 & 0 & 0 & 0 & 0 & 0 & 0 & 0 & 0 & 0 & 0 & 0 & 0 & 0 & 0 & 0 & 0 \\
0 & 0 & 0 & 0 & 0 & 0 & 0 & 0 & 0 & 0 & 0 & 0 & 0 & 0 & 0 & 0 & 0 & 0 & 0 & 0 & 0 & 0 & 0 & 0 & 0 & 0 & 0 & 0 \\
0 & 0 & 0 & 0 & 0 & 0 & 0 & 0 & 0 & 0 & 0 & 0 & 0 & 0 & 0 & 0 & 0 & 0 & 0 & 0 & 0 & 0 & 0 & 0 & 0 & 0 & 0 & 0 \\
0 & 0 & 0 & 0 & 0 & 0 & 0 & 0 & 0 & 0 & 0 & 0 & 0 & 0 & 0 & 0 & 0 & 0 & 0 & 0 & 0 & 0 & 0 & 0 & 0 & 0 & 0 & 0 \\
0 & 0 & 0 & 0 & 0 & 0 & 0 & 0 & 0 & 0 & 0 & 0 & 0 & 0 & 0 & 0 & 0 & $\sqrt{2}$ & 0 & 0 & 0 & 0 & 0 & 0 & 0 & 0 & 0 & 0 \\
0 & 0 & 0 & 0 & 0 & 0 & 0 & 0 & 0 & 0 & 0 & 0 & 0 & 0 & 0 & 0 & 0 & 0 & $\sqrt{2}$ & 0 & 0 & 0 & 0 & 0 & 0 & 0 & 0 & 0 \\
0 & 0 & $\frac{1}{\sqrt{2}}$ & 0 & 0 & 0 & 0 & 0 & 0 & 0 & 0 & 0 & 0 & 0 & 0 & 0 & 0 & 0 & 0 & $\frac{1}{\sqrt{2}}$ & 0 & 0 & 0 & 0 & 0 & 0 & 0 & 0 \\
0 & 0 & 0 & 0 & 0 & 0 & 0 & 0 & 0 & 0 & 0 & 0 & 0 & 0 & 0 & 0 & 0 & 0 & 0 & 0 & $\sqrt{2}$ & 0 & 0 & 0 & 0 & 0 & 0 & 0 \\
0 & 0 & 0 & 0 & $\frac{1}{\sqrt{2}}$ & 0 & 0 & 0 & 0 & 0 & 0 & 0 & 0 & 0 & 0 & 0 & 0 & 0 & 0 & 0 & 0 & $\frac{1}{\sqrt{2}}$ & 0 & 0 & 0 & 0 & 0 & 0 \\
0 & 0 & 0 & 0 & 0 & $\frac{1}{\sqrt{2}}$ & 0 & 0 & 0 & 0 & 0 & 0 & 0 & 0 & 0 & 0 & 0 & 0 & 0 & 0 & 0 & $\frac{1}{\sqrt{2}}$ & 0 & 0 & 0 & 0 & 0 & 0 \\
0 & 0 & 0 & 0 & 0 & 0 & 0 & 0 & 0 & 0 & 0 & 0 & 0 & 0 & 0 & 0 & 0 & 0 & 0 & 0 & 0 & 0 & $\sqrt{2}$ & 0 & 0 & 0 & 0 & 0 \\
0 & 0 & 0 & 0 & 0 & 0 & 0 & 0 & 0 & 0 & 0 & 0 & 0 & 0 & 0 & 0 & 0 & 0 & 0 & 0 & 0 & 0 & 0 & $\sqrt{2}$ & 0 & 0 & 0 & 0 \\
0 & 0 & 0 & 0 & 0 & 0 & 0 & 0 & 0 & 0 & 0 & 0 & 0 & 0 & 0 & 0 & 0 & 0 & 0 & 0 & 0 & 0 & 0 & 0 & $\frac{1}{\sqrt{2}}$ & 0 & 0 & 0 \\
0 & 0 & 0 & 0 & 0 & 0 & 0 & 0 & 0 & 0 & 0 & 0 & 0 & 0 & 0 & 0 & 0 & 0 & 0 & 0 & 0 & 0 & 0 & 0 & 0 & $\sqrt{2}$ & 0 & 0 \\
0 & 0 & 0 & 0 & 0 & 0 & 0 & 0 & 0 & 0 & 0 & 0 & 0 & 0 & 0 & 0 & 0 & 0 & 0 & 0 & 0 & 0 & 0 & 0 & 0 & 0 & $\frac{1}{\sqrt{2}}$ & 0 \\
0 & 0 & 0 & 0 & 0 & 0 & 0 & 0 & 0 & 0 & 0 & 0 & 0 & 0 & 0 & 0 & 0 & 0 & 0 & 0 & 0 & 0 & 0 & 0 & 0 & 0 & 0 & $\frac{1}{\sqrt{2}}$ \\
0 & 0 & 0 & 0 & 0 & 0 & 0 & 0 & 0 & 0 & 0 & 0 & 0 & 0 & 0 & 0 & 0 & 0 & 0 & 0 & 0 & 0 & 0 & 0 & 0 & 0 & 0 & 0 \\
0 & 0 & 0 & 0 & 0 & 0 & 0 & 0 & 0 & 0 & 0 & 0 & 0 & 0 & 0 & 0 & 0 & 0 & 0 & 0 & 0 & 0 & 0 & 0 & 0 & 0 & 0 & 0 \\
0 & 0 & 0 & 0 & 0 & 0 & 0 & 0 & 0 & 0 & 0 & 0 & 0 & 0 & 0 & 0 & 0 & 0 & 0 & 0 & 0 & 0 & 0 & 0 & 0 & 0 & 0 & 0 \\
0 & 0 & 0 & 0 & 0 & 0 & 0 & 0 & 0 & 0 & 0 & 0 & 0 & 0 & 0 & 0 & 0 & 0 & 0 & 0 & 0 & 0 & 0 & 0 & 0 & 0 & 0 & 0 \\
0 & 0 & 0 & 0 & 0 & 0 & 0 & 0 & 0 & 0 & 0 & 0 & 0 & 0 & 0 & 0 & 0 & 0 & 0 & 0 & 0 & 0 & 0 & 0 & 0 & 0 & 0 & 0
\end{bmatrix}$$

$$\mathbf{S}_2^+ + \mathbf{S}_3^+ + \mathbf{S}_4^+ = \begin{bmatrix}
0 & 0 & 0 & 0 & 0 & 0 & 0 & 0 & 0 & 0 & 0 & 0 & 0 & 0 & 0 & 0 & 0 & 0 & 0 & 0 & \frac{1}{\sqrt{2}} & 0 & 0 & 0 & 0 & 0 \\
0 & 0 & 0 & 0 & 0 & 0 & 0 & 0 & 0 & 0 & 0 & 0 & 0 & 0 & 0 & 0 & 0 & 0 & 0 & 0 & 0 & 0 & 0 & 0 & 0 & 0 \\
0 & 0 & 0 & 0 & 0 & 0 & 0 & 0 & 0 & 0 & 0 & 0 & 0 & 0 & 0 & 0 & 0 & 0 & 0 & 0 & 0 & 0 & 0 & 0 & 0 & 0 \\
0 & 0 & 0 & 0 & 0 & 0 & 0 & 0 & 0 & 0 & 0 & 0 & 0 & 0 & 0 & 0 & 0 & 0 & 0 & 0 & 0 & 0 & 0 & \frac{1}{\sqrt{2}} & 0 & 0 \\
0 & 0 & 0 & 0 & 0 & 0 & 0 & 0 & 0 & 0 & 0 & 0 & 0 & 0 & 0 & 0 & 0 & 0 & 0 & 0 & 0 & 0 & 0 & 0 & 0 & 0 \\
0 & 0 & 0 & 0 & 0 & 0 & 0 & 0 & 0 & 0 & 0 & 0 & 0 & 0 & 0 & 0 & 0 & 0 & 0 & 0 & 0 & 0 & 0 & 0 & 0 & \frac{1}{\sqrt{2}} \\
0 & 0 & 0 & 0 & 0 & 0 & 0 & 0 & 0 & 0 & 0 & 0 & 0 & 0 & 0 & 0 & 0 & 0 & 0 & 0 & 0 & 0 & 0 & 0 & 0 & 0 \\
0 & 0 & 0 & 0 & 0 & 0 & 0 & 0 & 0 & 0 & 0 & 0 & 0 & 0 & 0 & 0 & 0 & 0 & 0 & 0 & 0 & 0 & 0 & 0 & 0 & 0 \\
0 & 0 & 0 & 0 & 0 & 0 & 0 & 0 & 0 & 0 & 0 & 0 & 0 & 0 & 0 & 0 & 0 & 0 & 0 & 0 & 0 & 0 & 0 & 0 & 0 & 0 \\
0 & 0 & 0 & 0 & 0 & 0 & 0 & 0 & 0 & 0 & 0 & 0 & 0 & 0 & 0 & 0 & 0 & 0 & 0 & 0 & 0 & 0 & 0 & 0 & 0 & 0 \\
-\frac{1}{\sqrt{2}} & 0 & 0 & 0 & 0 & 0 & 0 & 0 & 0 & 0 & 0 & 0 & 0 & 0 & 0 & \frac{1}{\sqrt{2}} & 0 & 0 & 0 & 0 & 0 & 0 & 0 & 0 & 0 & 0 \\
0 & 0 & 0 & 0 & 0 & 0 & 0 & 0 & 0 & 0 & 0 & 0 & 0 & 0 & 0 & 0 & \sqrt{2} & 0 & 0 & 0 & 0 & 0 & 0 & 0 & 0 & 0 \\
0 & 0 & 0 & 0 & 0 & 0 & 0 & 0 & 0 & 0 & 0 & 0 & 0 & 0 & 0 & 0 & 0 & \sqrt{2} & 0 & 0 & 0 & 0 & 0 & 0 & 0 & 0 \\
0 & 0 & 0 & -\frac{1}{\sqrt{2}} & 0 & 0 & 0 & 0 & 0 & 0 & 0 & 0 & 0 & 0 & 0 & 0 & 0 & 0 & \frac{1}{\sqrt{2}} & 0 & 0 & 0 & 0 & 0 & 0 & 0 \\
0 & 0 & 0 & 0 & 0 & 0 & 0 & 0 & 0 & 0 & 0 & 0 & 0 & 0 & 0 & 0 & 0 & 0 & 0 & \sqrt{2} & 0 & 0 & 0 & 0 & 0 & 0 \\
0 & 0 & 0 & 0 & 0 & -\frac{1}{\sqrt{2}} & 0 & 0 & 0 & 0 & 0 & 0 & 0 & 0 & 0 & 0 & 0 & 0 & 0 & 0 & \frac{1}{\sqrt{2}} & 0 & 0 & 0 & 0 & 0 \\
0 & 0 & 0 & 0 & 0 & 0 & 0 & 0 & 0 & 0 & 0 & 0 & 0 & 0 & 0 & 0 & 0 & 0 & 0 & 0 & 0 & \frac{1}{\sqrt{2}} & 0 & 0 & 0 & 0 \\
0 & 0 & 0 & 0 & 0 & 0 & 0 & 0 & 0 & 0 & 0 & 0 & 0 & 0 & 0 & 0 & 0 & 0 & 0 & 0 & 0 & 0 & \sqrt{2} & 0 & 0 & 0 \\
0 & 0 & 0 & 0 & 0 & 0 & 0 & 0 & 0 & 0 & 0 & 0 & 0 & 0 & 0 & 0 & 0 & 0 & 0 & 0 & 0 & 0 & 0 & \sqrt{2} & 0 & 0 \\
0 & 0 & 0 & 0 & 0 & 0 & 0 & 0 & 0 & 0 & 0 & 0 & 0 & 0 & 0 & 0 & 0 & 0 & 0 & 0 & 0 & 0 & 0 & 0 & \frac{1}{\sqrt{2}} & 0 \\
0 & 0 & 0 & 0 & 0 & 0 & 0 & 0 & 0 & 0 & 0 & 0 & 0 & 0 & 0 & 0 & 0 & 0 & 0 & 0 & 0 & 0 & 0 & 0 & 0 & \frac{1}{\sqrt{2}} \\
0 & 0 & 0 & 0 & 0 & 0 & 0 & 0 & 0 & 0 & 0 & 0 & 0 & 0 & 0 & 0 & 0 & 0 & 0 & 0 & 0 & 0 & 0 & 0 & 0 & 0 \\
0 & 0 & 0 & 0 & 0 & 0 & 0 & 0 & 0 & 0 & 0 & 0 & 0 & 0 & 0 & 0 & 0 & 0 & 0 & 0 & 0 & 0 & 0 & 0 & 0 & 0 \\
0 & 0 & 0 & 0 & 0 & 0 & 0 & 0 & 0 & 0 & 0 & 0 & 0 & 0 & 0 & 0 & 0 & 0 & 0 & 0 & 0 & 0 & 0 & 0 & 0 & 0 \\
0 & 0 & 0 & 0 & 0 & 0 & 0 & 0 & 0 & 0 & 0 & 0 & 0 & 0 & 0 & 0 & 0 & 0 & 0 & 0 & 0 & 0 & 0 & 0 & 0 & 0 \\
0 & 0 & 0 & 0 & 0 & 0 & 0 & 0 & 0 & 0 & 0 & 0 & 0 & 0 & 0 & 0 & 0 & 0 & 0 & 0 & 0 & 0 & 0 & 0 & 0 & 0 \\
0 & 0 & 0 & 0 & 0 & 0 & 0 & 0 & 0 & 0 & 0 & 0 & 0 & 0 & 0 & 0 & 0 & 0 & 0 & 0 & 0 & 0 & 0 & 0 & 0 & 0
\end{bmatrix}$$

$$\mathbf{S}_1^- + \mathbf{S}_2^- + \mathbf{S}_3^- = \begin{bmatrix}
0 & 0 & 0 & 0 & 0 & 0 & 0 & 0 & 0 & 0 & 0 & 0 & 0 & 0 & 0 & 0 & 0 & 0 & 0 & 0 & 0 & 0 & 0 & 0 & 0 & 0 & 0 & 0 \\
0 & 0 & 0 & 0 & 0 & 0 & 0 & 0 & 0 & 0 & 0 & 0 & 0 & 0 & 0 & 0 & 0 & 0 & 0 & 0 & 0 & 0 & 0 & 0 & 0 & 0 & 0 & 0 \\
0 & 0 & 0 & 0 & 0 & 0 & 0 & 0 & 0 & 0 & 0 & 0 & \frac{1}{\sqrt{2}} & 0 & 0 & 0 & 0 & 0 & 0 & 0 & 0 & 0 & 0 & 0 & 0 & 0 & 0 & 0 \\
0 & 0 & 0 & 0 & 0 & 0 & 0 & 0 & 0 & 0 & 0 & 0 & 0 & 0 & 0 & 0 & 0 & 0 & 0 & 0 & 0 & 0 & 0 & 0 & 0 & 0 & 0 & 0 \\
0 & 0 & 0 & 0 & 0 & 0 & 0 & 0 & 0 & 0 & 0 & 0 & 0 & 0 & \frac{1}{\sqrt{2}} & 0 & 0 & 0 & 0 & 0 & 0 & 0 & 0 & 0 & 0 & 0 & 0 & 0 \\
0 & 0 & 0 & 0 & 0 & 0 & 0 & 0 & 0 & 0 & 0 & 0 & 0 & 0 & 0 & \frac{1}{\sqrt{2}} & 0 & 0 & 0 & 0 & 0 & 0 & 0 & 0 & 0 & 0 & 0 & 0 \\
0 & 0 & 0 & 0 & 0 & 0 & 0 & 0 & 0 & 0 & 0 & 0 & 0 & 0 & 0 & 0 & 0 & 0 & 0 & 0 & 0 & 0 & 0 & 0 & 0 & 0 & 0 & 0 \\
0 & 0 & 0 & 0 & 0 & 0 & 0 & 0 & 0 & 0 & 0 & 0 & 0 & 0 & 0 & 0 & 0 & 0 & 0 & 0 & 0 & 0 & 0 & 0 & 0 & 0 & 0 & 0 \\
0 & 0 & 0 & 0 & 0 & 0 & 0 & 0 & 0 & 0 & 0 & 0 & 0 & 0 & 0 & 0 & 0 & 0 & 0 & 0 & 0 & 0 & 0 & 0 & 0 & 0 & 0 & 0 \\
0 & 0 & 0 & 0 & 0 & 0 & 0 & 0 & 0 & 0 & 0 & 0 & 0 & 0 & 0 & 0 & 0 & 0 & 0 & 0 & 0 & 0 & 0 & 0 & 0 & 0 & 0 & 0 \\
0 & 0 & 0 & 0 & 0 & 0 & 0 & 0 & 0 & 0 & 0 & 0 & 0 & 0 & 0 & 0 & 0 & 0 & 0 & 0 & 0 & 0 & 0 & 0 & 0 & 0 & 0 & 0 \\
0 & 0 & 0 & 0 & 0 & 0 & 0 & 0 & 0 & 0 & 0 & 0 & 0 & 0 & 0 & 0 & 0 & 0 & 0 & 0 & 0 & 0 & 0 & 0 & 0 & 0 & 0 & 0 \\
0 & 0 & 0 & 0 & 0 & 0 & 0 & 0 & 0 & 0 & 0 & 0 & 0 & 0 & 0 & 0 & 0 & 0 & 0 & 0 & 0 & 0 & 0 & 0 & 0 & 0 & 0 & 0 \\
0 & 0 & 0 & 0 & 0 & 0 & 0 & 0 & 0 & 0 & 0 & 0 & 0 & 0 & 0 & 0 & 0 & 0 & 0 & 0 & 0 & 0 & 0 & 0 & 0 & 0 & 0 & 0 \\
0 & 0 & 0 & 0 & 0 & 0 & 0 & 0 & 0 & 0 & 0 & 0 & 0 & 0 & 0 & 0 & 0 & 0 & 0 & 0 & 0 & 0 & 0 & 0 & 0 & 0 & 0 & 0 \\
0 & 0 & 0 & 0 & 0 & 0 & 0 & 0 & 0 & 0 & 0 & 0 & 0 & 0 & 0 & 0 & 0 & 0 & 0 & 0 & 0 & 0 & 0 & 0 & 0 & 0 & 0 & 0 \\
0 & 0 & 0 & 0 & 0 & 0 & 0 & 0 & 0 & 0 & 0 & 0 & 0 & 0 & 0 & 0 & 0 & 0 & 0 & 0 & 0 & 0 & 0 & 0 & 0 & 0 & 0 & 0 \\
0 & 0 & 0 & 0 & 0 & 0 & 0 & 0 & 0 & 0 & 0 & 0 & 0 & 0 & 0 & 0 & 0 & 0 & 0 & 0 & 0 & 0 & 0 & 0 & 0 & 0 & 0 & 0 \\
0 & 0 & 0 & 0 & 0 & 0 & 0 & 0 & 0 & 0 & \sqrt{2} & 0 & 0 & 0 & 0 & 0 & 0 & 0 & 0 & 0 & 0 & 0 & 0 & 0 & 0 & 0 & 0 & 0 \\
0 & 0 & 0 & 0 & 0 & 0 & 0 & 0 & 0 & 0 & 0 & \sqrt{2} & 0 & 0 & 0 & 0 & 0 & 0 & 0 & 0 & 0 & 0 & 0 & 0 & 0 & 0 & 0 & 0 \\
0 & 0 & 0 & 0 & 0 & 0 & 0 & 0 & 0 & 0 & 0 & 0 & \frac{1}{\sqrt{2}} & 0 & 0 & 0 & 0 & 0 & 0 & 0 & 0 & 0 & 0 & 0 & 0 & 0 & 0 & 0 \\
0 & 0 & 0 & 0 & 0 & 0 & 0 & 0 & 0 & 0 & 0 & 0 & 0 & \sqrt{2} & 0 & 0 & 0 & 0 & 0 & 0 & 0 & 0 & 0 & 0 & 0 & 0 & 0 & 0 \\
0 & 0 & 0 & 0 & 0 & 0 & 0 & 0 & 0 & 0 & 0 & 0 & 0 & 0 & \frac{1}{\sqrt{2}} & 0 & 0 & 0 & 0 & 0 & 0 & 0 & 0 & 0 & 0 & 0 & 0 & 0 \\
0 & 0 & 0 & 0 & 0 & 0 & 0 & 0 & 0 & 0 & 0 & 0 & 0 & 0 & 0 & \frac{1}{\sqrt{2}} & 0 & 0 & 0 & 0 & 0 & 0 & 0 & 0 & 0 & 0 & 0 & 0 \\
0 & 0 & 0 & 0 & 0 & 0 & 0 & 0 & 0 & 0 & 0 & 0 & 0 & 0 & 0 & 0 & \sqrt{2} & 0 & 0 & 0 & 0 & 0 & 0 & 0 & 0 & 0 & 0 & 0 \\
0 & 0 & 0 & 0 & 0 & 0 & 0 & 0 & 0 & 0 & 0 & 0 & 0 & 0 & 0 & 0 & 0 & \sqrt{2} & 0 & 0 & 0 & 0 & 0 & 0 & 0 & 0 & 0 & 0 \\
0 & 0 & -\frac{1}{\sqrt{2}} & 0 & 0 & 0 & 0 & 0 & 0 & 0 & 0 & 0 & 0 & 0 & 0 & 0 & 0 & 0 & \frac{1}{\sqrt{2}} & 0 & 0 & 0 & 0 & 0 & 0 & 0 & 0 & 0 & 0 \\
0 & 0 & 0 & 0 & 0 & 0 & 0 & 0 & 0 & 0 & 0 & 0 & 0 & 0 & 0 & 0 & 0 & 0 & 0 & \sqrt{2} & 0 & 0 & 0 & 0 & 0 & 0 & 0 & 0 \\
0 & 0 & 0 & 0 & -\frac{1}{\sqrt{2}} & 0 & 0 & 0 & 0 & 0 & 0 & 0 & 0 & 0 & 0 & 0 & 0 & 0 & 0 & 0 & \frac{1}{\sqrt{2}} & 0 & 0 & 0 & 0 & 0 & 0 & 0 \\
0 & 0 & 0 & 0 & 0 & -\frac{1}{\sqrt{2}} & 0 & 0 & 0 & 0 & 0 & 0 & 0 & 0 & 0 & 0 & 0 & 0 & 0 & 0 & 0 & \frac{1}{\sqrt{2}} & 0 & 0 & 0 & 0 & 0 & 0
\end{bmatrix}$$

$$\mathbf{S}_2^- + \mathbf{S}_3^- + \mathbf{S}_4^- = \begin{bmatrix}
0 & 0 & 0 & 0 & 0 & 0 & 0 & 0 & 0 & 0 & -\frac{1}{\sqrt{2}} & 0 & 0 & 0 & 0 & 0 & 0 & 0 & 0 & 0 & 0 & 0 & 0 & 0 & 0 & 0 & 0 \\
0 & 0 & 0 & 0 & 0 & 0 & 0 & 0 & 0 & 0 & 0 & 0 & 0 & 0 & 0 & 0 & 0 & 0 & 0 & 0 & 0 & 0 & 0 & 0 & 0 & 0 & 0 \\
0 & 0 & 0 & 0 & 0 & 0 & 0 & 0 & 0 & 0 & 0 & 0 & 0 & 0 & 0 & 0 & 0 & 0 & 0 & 0 & 0 & 0 & 0 & 0 & 0 & 0 & 0 \\
0 & 0 & 0 & 0 & 0 & 0 & 0 & 0 & 0 & 0 & 0 & 0 & 0 & -\frac{1}{\sqrt{2}} & 0 & 0 & 0 & 0 & 0 & 0 & 0 & 0 & 0 & 0 & 0 & 0 & 0 \\
0 & 0 & 0 & 0 & 0 & 0 & 0 & 0 & 0 & 0 & 0 & 0 & 0 & 0 & 0 & 0 & 0 & 0 & 0 & 0 & 0 & 0 & 0 & 0 & 0 & 0 & 0 \\
0 & 0 & 0 & 0 & 0 & 0 & 0 & 0 & 0 & 0 & 0 & 0 & 0 & 0 & 0 & -\frac{1}{\sqrt{2}} & 0 & 0 & 0 & 0 & 0 & 0 & 0 & 0 & 0 & 0 & 0 \\
0 & 0 & 0 & 0 & 0 & 0 & 0 & 0 & 0 & 0 & 0 & 0 & 0 & 0 & 0 & 0 & 0 & 0 & 0 & 0 & 0 & 0 & 0 & 0 & 0 & 0 & 0 \\
0 & 0 & 0 & 0 & 0 & 0 & 0 & 0 & 0 & 0 & 0 & 0 & 0 & 0 & 0 & 0 & 0 & 0 & 0 & 0 & 0 & 0 & 0 & 0 & 0 & 0 & 0 \\
0 & 0 & 0 & 0 & 0 & 0 & 0 & 0 & 0 & 0 & 0 & 0 & 0 & 0 & 0 & 0 & 0 & 0 & 0 & 0 & 0 & 0 & 0 & 0 & 0 & 0 & 0 \\
0 & 0 & 0 & 0 & 0 & 0 & 0 & 0 & 0 & 0 & 0 & 0 & 0 & 0 & 0 & 0 & 0 & 0 & 0 & 0 & 0 & 0 & 0 & 0 & 0 & 0 & 0 \\
0 & 0 & 0 & 0 & 0 & 0 & 0 & 0 & 0 & 0 & 0 & 0 & 0 & 0 & 0 & 0 & 0 & 0 & 0 & 0 & 0 & 0 & 0 & 0 & 0 & 0 & 0 \\
0 & 0 & 0 & 0 & 0 & 0 & 0 & 0 & 0 & 0 & 0 & 0 & 0 & 0 & 0 & 0 & 0 & 0 & 0 & 0 & 0 & 0 & 0 & 0 & 0 & 0 & 0 \\
0 & 0 & 0 & 0 & 0 & 0 & 0 & 0 & 0 & 0 & 0 & 0 & 0 & 0 & 0 & 0 & 0 & 0 & 0 & 0 & 0 & 0 & 0 & 0 & 0 & 0 & 0 \\
0 & 0 & 0 & 0 & 0 & 0 & 0 & 0 & 0 & 0 & 0 & 0 & 0 & 0 & 0 & 0 & 0 & 0 & 0 & 0 & 0 & 0 & 0 & 0 & 0 & 0 & 0 \\
0 & 0 & 0 & 0 & 0 & 0 & 0 & 0 & 0 & 0 & 0 & 0 & 0 & 0 & 0 & 0 & 0 & 0 & 0 & 0 & 0 & 0 & 0 & 0 & 0 & 0 & 0 \\
0 & 0 & 0 & 0 & 0 & 0 & 0 & 0 & 0 & 0 & 0 & 0 & 0 & 0 & 0 & 0 & 0 & 0 & 0 & 0 & 0 & 0 & 0 & 0 & 0 & 0 & 0 \\
0 & 0 & 0 & 0 & 0 & 0 & 0 & 0 & 0 & 0 & 0 & 0 & 0 & 0 & 0 & 0 & 0 & 0 & 0 & 0 & 0 & 0 & 0 & 0 & 0 & 0 & 0 \\
0 & 0 & 0 & 0 & 0 & 0 & 0 & 0 & 0 & 0 & 0 & 0 & 0 & 0 & 0 & 0 & 0 & 0 & 0 & 0 & 0 & 0 & 0 & 0 & 0 & 0 & 0 \\
0 & 0 & 0 & 0 & 0 & 0 & 0 & 0 & 0 & 0 & \frac{1}{\sqrt{2}} & 0 & 0 & 0 & 0 & 0 & 0 & 0 & 0 & 0 & 0 & 0 & 0 & 0 & 0 & 0 & 0 \\
0 & 0 & 0 & 0 & 0 & 0 & 0 & 0 & 0 & 0 & 0 & \sqrt{2} & 0 & 0 & 0 & 0 & 0 & 0 & 0 & 0 & 0 & 0 & 0 & 0 & 0 & 0 & 0 \\
0 & 0 & 0 & 0 & 0 & 0 & 0 & 0 & 0 & 0 & 0 & 0 & \sqrt{2} & 0 & 0 & 0 & 0 & 0 & 0 & 0 & 0 & 0 & 0 & 0 & 0 & 0 & 0 \\
0 & 0 & 0 & 0 & 0 & 0 & 0 & 0 & 0 & 0 & 0 & 0 & 0 & \frac{1}{\sqrt{2}} & 0 & 0 & 0 & 0 & 0 & 0 & 0 & 0 & 0 & 0 & 0 & 0 & 0 \\
0 & 0 & 0 & 0 & 0 & 0 & 0 & 0 & 0 & 0 & 0 & 0 & 0 & 0 & \sqrt{2} & 0 & 0 & 0 & 0 & 0 & 0 & 0 & 0 & 0 & 0 & 0 & 0 \\
0 & 0 & 0 & 0 & 0 & 0 & 0 & 0 & 0 & 0 & 0 & 0 & 0 & 0 & 0 & \frac{1}{\sqrt{2}} & 0 & 0 & 0 & 0 & 0 & 0 & 0 & 0 & 0 & 0 & 0 \\
\frac{1}{\sqrt{2}} & 0 & 0 & 0 & 0 & 0 & 0 & 0 & 0 & 0 & 0 & 0 & 0 & 0 & 0 & 0 & \frac{1}{\sqrt{2}} & 0 & 0 & 0 & 0 & 0 & 0 & 0 & 0 & 0 & 0 \\
0 & 0 & 0 & 0 & 0 & 0 & 0 & 0 & 0 & 0 & 0 & 0 & 0 & 0 & 0 & 0 & 0 & \sqrt{2} & 0 & 0 & 0 & 0 & 0 & 0 & 0 & 0 & 0 \\
0 & 0 & 0 & 0 & 0 & 0 & 0 & 0 & 0 & 0 & 0 & 0 & 0 & 0 & 0 & 0 & 0 & 0 & \sqrt{2} & 0 & 0 & 0 & 0 & 0 & 0 & 0 & 0 \\
0 & 0 & 0 & \frac{1}{\sqrt{2}} & 0 & 0 & 0 & 0 & 0 & 0 & 0 & 0 & 0 & 0 & 0 & 0 & 0 & 0 & 0 & \frac{1}{\sqrt{2}} & 0 & 0 & 0 & 0 & 0 & 0 & 0 \\
0 & 0 & 0 & 0 & 0 & 0 & 0 & 0 & 0 & 0 & 0 & 0 & 0 & 0 & 0 & 0 & 0 & 0 & 0 & \sqrt{2} & 0 & 0 & 0 & 0 & 0 & 0 & 0 \\
0 & 0 & 0 & 0 & 0 & \frac{1}{\sqrt{2}} & 0 & 0 & 0 & 0 & 0 & 0 & 0 & 0 & 0 & 0 & 0 & 0 & 0 & 0 & \frac{1}{\sqrt{2}} & 0 & 0 & 0 & 0 & 0 & 0
\end{bmatrix}$$